Commissioning and Characterization of a TPC with an InGrid based Readout

Felix Müller

Masterarbeit in Physik
angefertigt im Physikalischen Institut

vorgelegt der
Mathematisch-Naturwissenschaftlichen Fakultät
der
Rheinischen Friedrich-Wilhelms-Universität
Bonn

November 2011

1. Gutachter: Prof. Dr. Klaus Desch
2. Gutachter: Prof. Dr. Reinhard Beck

Acknowledgments

First of all, I would like to thank Prof. Klaus Desch for giving me the opportunity to write my thesis in his working group and giving me such an interesting and challenging topic. I am also grateful to Prof. Reinhard Beck for taking the role of the second reviewer.
I would like to show my gratitude to the members of the working group. I have to mention Christoph Brezina, Dr. Jochen Kaminski, Thorsten Krautscheid and Christoph Krieger as they all gave me a great time during the thesis and helped me with interesting discussions to gather a deeper understanding of my topic.
Of course, spatial thanks go to my parents Dieter Müller and Claudia Stadler-Müller and my sister Jana for the support in all kind of ways during my whole life.

Contents

1 Introduction **1**

2 Gaseous Detectors **5**
2.1 Energy Loss of Charged Particles in Matter 5
2.2 Ionization and Electron Attachment 8
2.3 Electron and Ion Drift and Diffusion 10
2.4 Gas Amplification 13
2.5 Signal Development 15
2.6 Time Projection Chamber 16
2.6.1 Gas Electron Multipliers 18
2.6.2 Micromegas 19
2.7 Gas Configurations 20
2.8 Cosmic Rays 21

3 Experimental Setup **23**
3.1 Timepix Pixel Chip 23
3.2 InGrid 25
3.3 Bonner TPC- Prototype 27
3.4 Setup 27

4 Analysis Framework **31**
4.1 Linear Collider Input Output (LCIO) 31
4.2 Marlin and MarlinTPC 31

5 Data Analysis and Results **33**
5.1 First Measurements 33
5.2 Charge Spread of an Avalanche 33
5.3 Drift Velocity 36
5.4 Reconstruction Chain 38
5.5 Charge Calibration of the Timepix 40
5.6 Gas Amplification 41
5.7 Track Parameters and Cuts Applied 43
5.8 Noise Reduction 45
5.9 Field Distortions 47
5.10 Number of Electrons per Track Length and Efficiency 49
5.11 Spatial Resolution 52
5.11.1 Transverse Spatial Resolution 53
5.11.2 Correction of Field Inhomogeneities 54
5.11.3 Longitudinal Spatial Resolution 56

6 Conclusion **61**

A Backup Figures **63**

Bibliography **67**

List of Figures **69**

List of Tables **73**

Chapter 1

Introduction

Since the Greek philosophers and their theories of the atom as the smallest element of matter, mankind has tried to understand the constituents of matter. Nowadays, scientists and in particular, particle physicists have taken over the role of philosophers and research subatomic particles and their fundamental interactions with scientific experiments.
The advancement of technology during the last two centuries has given rise to the discovery of many elementary particles, e.g. the quarks, the leptons and the gauge bosons. These particles were studied well during the last decades and many characteristics were measured with great accuracy. Theorists developed the Standard Model (SM), which has become the most successful theory in particle physics as it describes the most of the observed phenomena. The origin of mass is still unknown but is an essential part of understanding the universe. Furthermore, a breaking of the electroweak force into electromagnetic and weak force was discovered experimentally. The Higgs field is introduced for the elektroweak symmetry breaking in the SM and is also responsible for the mass of the W- and Z-Boson. It is omnipresent in the universe and could also give mass to the other elementary massive particles trough a Yukawa-interaction. The Higgs-mechanism also predicts the existence of the Higgs Boson. The Higgs Boson is still not observed by any experiment and became the last step to validating the SM.
Two important tools of particle physicists are particle accelerators and particle detectors. The accelerators boost the kinetic energy of charged particles and collide them. These particles interact at high center of mass energies and different particles can be created. In the past the energy of the collisions was increased further and further to generate unknown particles with higher masses. The particle detectors survey the reaction products of the collisions and measure the properties of the resulting particles. With the measured parameters one can deduce a large amount of information about the observed particles, e.g. the masses, cross sections of reactions, lifetimes and decay products.
In 2009 a new proton-proton collider, the Large Hadron Collider (LHC), started operating. With a design center of mass energy of 14 TeV, the LHC has the highest center of mass energy seen up until now. This high collision energy paired with high resolution particle detectors give the LHC the potential to find new phenomena of particle physics. Two of the main tasks of the LHC are the search of the Higgs Boson and the probing of physics beyond the Standard Model. Whereas many other experiments and theories have already given limits on the mass of the Higgs Boson but could not discover it, the LHC investigates the remaining mass ranges of a Standard Model Higgs Boson. Other questions remain unanswered by the SM, e.g. the nature of dark matter. Further theories, like Supersymmetry (SUSY) or M-theory, introduce new particles which are candidates for dark matter and generate new forces or symmetries at the terascale energies [1]. The LHC has taken data with a total collision energy of 7 TeV until now and has opened the terascale region for new discoveries.
The major disadvantage of the LHC is the unknown initial state of the colliding particles, as they are composite and not elementary particles. The LHC also suffers from a high background due to many strong interactions, which restrict the measurement precision of the detectors. These are the reasons for the necessity of the International Linear Collider (ILC). The ILC is a future linear electron-positron

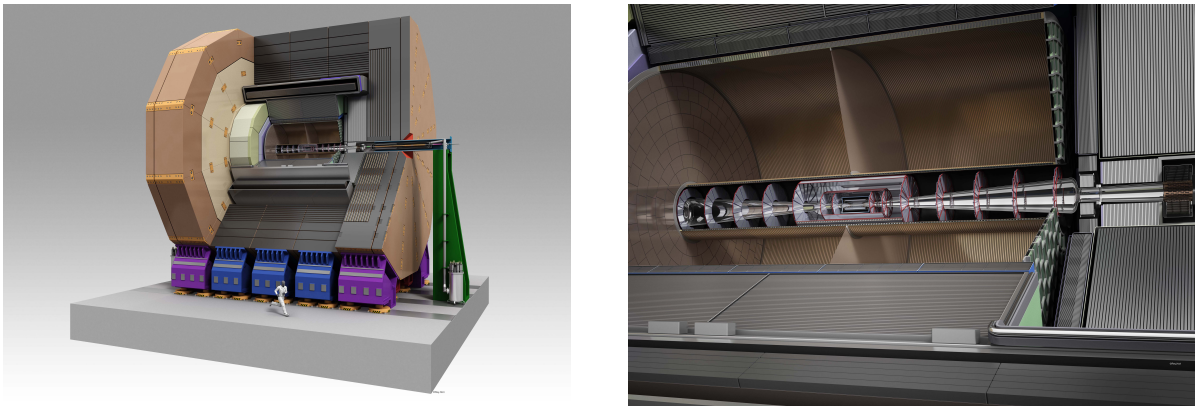

Figure 1.1: Left: Illustration of the whole ILD. Right: Zoom inside the TPC of the ILD [4]

collider, which is still in the design and research phase. Its energy should be tunable from 200 GeV to 500 GeV with the option to run on the mass of the Z-Boson and an upgrade to 1 TeV. It will be able to verify the results of the LHC and to do precision measurements of newly found physics. To clarify the detector and collider performances one has to simulate theoretical interactions. Theory predicts one major Higgs Boson production channel to be $e^+e^- \rightarrow ZH \rightarrow l^+l^-X$ for the ILC. The mass of the Higgs Boson can be calculated from the recoil of the Z-Boson, if the parameters of the decay products are reconstructed well enough. To achieve a high signal to noise ratio the measurement resolution of the momentum has to be in the order of $\delta(1/p_t) \sim 2 \times 10^{-5}\,\mathrm{GeV}^{-1}$ for the tracking detectors [2].
Two different detectors are planned for the ILC which will be exchangeable in the single interaction area with a push-pull configuration. One of the detector concepts of the ILC is the International Large Detector (ILD). To reach the physics goals of the ILC strong requirements regarding detector performance need to be met. The information of highly granular tracking and calorimetry systems are combined to achieve the highest possible energy resolution. This so-called particle flow concept requires a high tracking efficiency, spatial resolution, efficient reconstruction of secondary vertices and momentum resolution. The choice for the ILD's central tracking detector is a large Time Projection Chamber (TPC) (see figure 1.1). Charged particles ionize a gaseous volume along its track inside a TPC. The electrons from the ionization drift towards the end caps as a result of an applied electric field. The drift time and the two dimensional detection of the electrons at the end caps allow a full three dimensional reconstruction of the tracks. The momentum resolution of $\delta(1/p_t) \sim 2 \times 10^{-5}\,\mathrm{GeV}^{-1}$ for the complete tracking system is reduced to $\delta(1/p_t) \sim 7 \times 10^{-5}\,\mathrm{GeV}^{-1}$ for the TPC alone (silicon based tracking detectors are also part of the tracking system). Many track points and a low material budget complement the good point resolution and double-hit resolution of a TPC [3]. For the ILD the amount of material in the barrel area should not exceed 5 % of a radiation length and in the end caps area 25 % of a radiation length.
Traditional wire readout systems of the TPC are not sufficient for the ILD and Micro-Pattern Gaseous Detectors (MPGD) will replace them. Different approaches are being studied at the moment. On the one hand, a pad readout with pad sizes of the order of $\sim 2\,\mathrm{mm} \times 2\,\mathrm{mm}$ and the on the other hand, a pixel chip with a pixel pitch of $\sim 55\,\mu\mathrm{m}$. Furthermore, the gas amplification stage of the MPGD is still under development with a focus on Micromegas and GEMs. GEMs are stand-alone amplification structures consisting of a Kapton foil with copper layers. Holes are etched in the structure and a voltage between the copper layers is applied. Micromegas are metal grids, which are placed around $100\,\mu\mathrm{m}$ above the readout plane. A voltage between the metal grid and the readout plane must also be applied.
In this study the performance of a Micromegas, mounted on a pixel chip, is studied. Measurements

inside a prototype TPC with a maximal drift distance of 26 cm are presented with tracks originating from cosmic muons. Point resolution and general parameters of the setup are presented and the assets and drawbacks of the technology are examined.

Chapter 2

Gaseous Detectors

The track of a particle can only be measured through an interaction with a detector material. One type of tracking devices are gaseous detectors. They are based on the principle that a charged particle ionizes atoms of the gas along its track. By detecting the free electrons one can reconstruct the track of a charged particle.
This chapter introduces the physics needed for a gaseous detector. To understand the functionality of a TPC in detail, the ionization of the gas, the drift of electrons/ions in the gas and the gas amplification is examined. At the end new types of Micro-Pattern Gaseous Detectors will be presented.

2.1 Energy Loss of Charged Particles in Matter

A charged particle loses kinetic energy while traveling through matter because of interactions with the material. The largest contribution to the energy loss is due to ionization and excitation processes through electromagnetic interactions. Other processes, e.g Čherenkov radiation, transition radiation and bremsstrahlung are negligible except at very high energies of the charged particle. As most of the time electrons of the detection volume are the collision partners of the charged particle, one has to distinguish between the case of an electron and of a more heavily charged particle. The spectrum of transferred energy looks quite different for both cases because an electron can transfer its complete kinetic energy to the detector material during a single interaction. This is also the classical expectation for a central collision of identical particles. The maximum kinetic energy transfer $E_{\text{trans}}^{\text{max}}$ for heavier particles can be expressed in the following way:

$$E_{\text{trans}}^{\text{max}} = \frac{E^2}{E + \frac{m_0^2 c^2}{2m_e}} \tag{2.1}$$

where m_0 is the mass of the charged particle and m_e is the mass of the electron. In this formula one uses the relativistic case where the energy E of the particle fulfills the relations $E \approx E_{\text{kin}}$ and $E \approx pc$.
The Bethe-Bloch equation describes the mean energy loss $\mathrm{d}E$ per track length $\mathrm{d}x$ in matter for heavy particles [5]

$$\frac{\mathrm{d}E}{\mathrm{d}x} = \frac{4\pi N e^4 z^2}{m_e c^2 \beta^2} \left\{ \ln\left(\frac{2m_e c^2 \beta^2 \gamma^2}{I} \right) - \beta^2 - \frac{\delta(\beta)}{2} \right\} \tag{2.2}$$

where

N	the number density of electrons in the traversed matter
z	the charge of the traveling particle
e	the elementary charge
$m_e c^2$	the rest energy of the electron

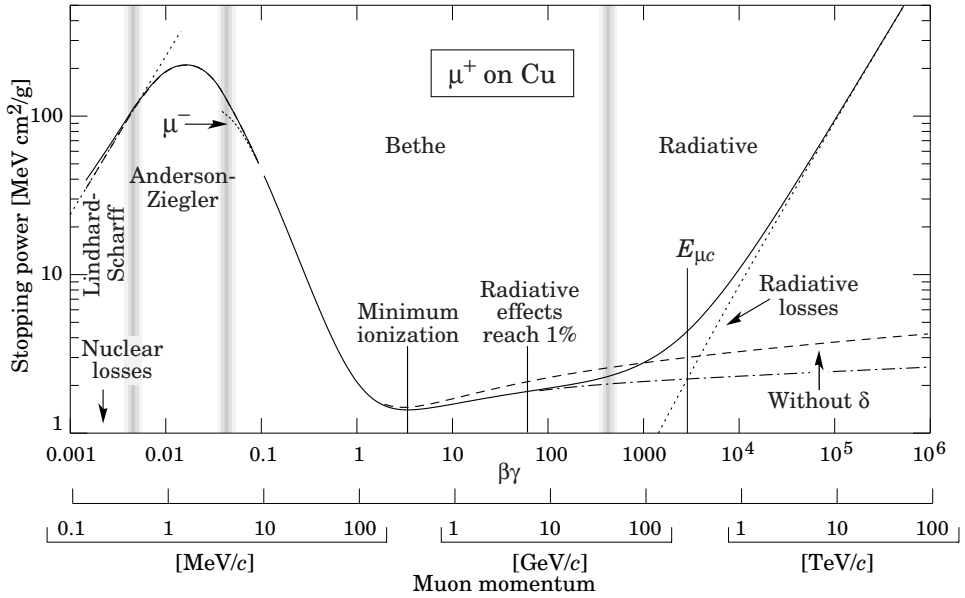

Figure 2.1: Illustration of the energy deposition of a muon. The Bethe-Bloch equation is only valid in the Bethe range and becomes invalid under very high energies due to radiative losses and under very low energies due to the internal structure of atoms [7].

β the velocity of the traveling particle in terms of the velocity c of light
$\gamma = \frac{1}{\sqrt{1-\beta^2}}$
I the mean excitation energy of the atom
$\delta(\beta)$ correction term for the density effect

The mean energy loss per length falls steeply with $1/\beta^2$ for low energies of the incident particle (see figure 2.1). This is due to the fact that slower particles feel the field of the atom longer and thus have a higher cross section. The function then has a minimum at around $\beta\gamma \approx 4$ and thereafter rises logarithmically. The origin of the rise is twofold. The first one is a kinematic effect. In equation (2.1) one can see that the maximum transferred energy increases with the velocity of the particle. In the case of an ultra-relativistic particle the complete kinetic energy can be transferred to the detection material which results in a higher probability for large energy transfers. The second effect is an expansion of the transverse electric field of the traveling particle due to the relativistic velocity. As a result the cross section for interactions with the detector material increases and energy transfer is more probable.
For high energies of the charged particle the relativistic rise is limited by the density effect. This was first calculated by Fermi in 1939. The atoms around the charged particles are polarized and screen the charge of the particle. This effect depends greatly on the detection material and its density, hence the name of the effect [6].
For very low and very high energies of the particle the Bethe-Bloch equation is not valid anymore. The radiative losses are not negligible for ultra-relativistic particles and shell effects of the atoms play an important role for low velocities.
Particles, whose energy is in the minimum region of the Bethe-Bloch formula, are called minimal ionizing particles (MIPs). As the relativistic rise is rather low, one also calls particles in this region MIPs, too. In this area one surveys comic muons which can be considered as MIPs according to this definition (see chapter 2.8 for information about cosmic rays).
One can also identify particles with the help of the energy loss per track length. A specific amount of

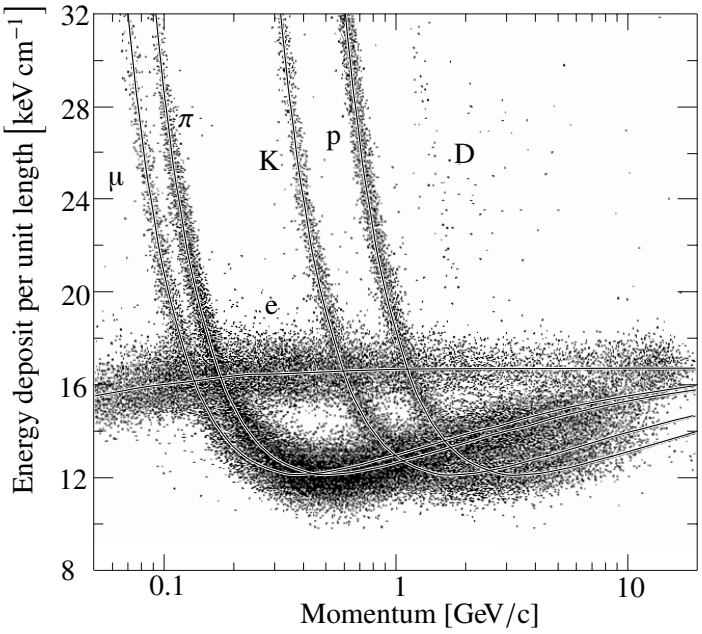

Figure 2.2: Energy deposition per unit length for single events in the PEP-4-Experiment. The data is well described by the Bethe-Bloch function for several particle types [7].

energy is transferred to the detector dependent on the momentum and the mass of the particle. If one measures the momentum and the energy loss, one can identify the particle types. The better the resolution of the detector, the larger the range of momentum where one is able to distinguish between the particles. Figure 2.2 shows a measurement from a TPC of the PEP-4-Experiment at the Stanford Linear Collider. One can see the characteristic energy losses for the particles. In the area of the relativistic rise, the detector resolution is not sufficient to identify the particles any more.
For gaseous detectors the statistical process of the energy transfer produces a large fluctuation around the mean energy loss due to the low number of interactions. In case of a thick absorber one measures a Gaussian distribution of the energy loss in the detector. A large tail is observed for thin absorbers because of the possibility of very large energy transfers. The distribution of energy loss in a thin absorber can be described by a Landau-distribution [6]. An approximation for the Landau-distribution is the following formula from Moyal [8]:

$$L(\lambda) = \frac{1}{\sqrt{2\pi}} \cdot \exp\left(-\frac{1}{2}\left(\lambda + \exp -\lambda\right)\right) \tag{2.3}$$

$$\lambda = \frac{\Delta E - \Delta E^{\mathrm{W}}}{\xi} \tag{2.4}$$

$$\xi = \frac{4\pi N e^4 z^2}{m_{\mathrm{e}} c^2 \beta^2} \rho x \tag{2.5}$$

where

ΔE	the mean energy loss in a layer of thickness x
ΔE^{W}	most probable energy loss in a layer of thickness x
ρ	density of the material
x	thickness of the detection layer

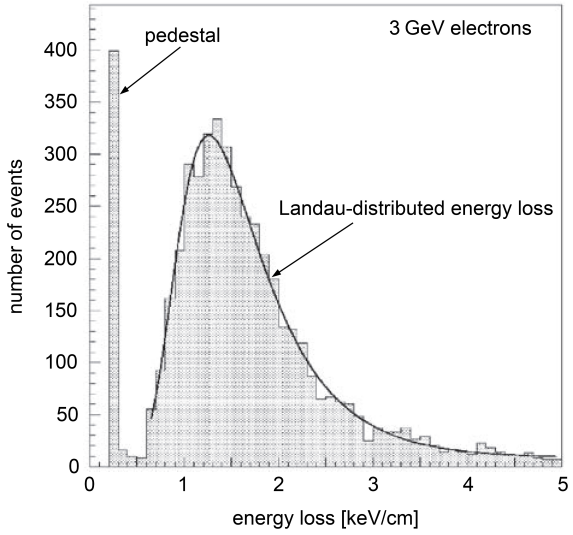

Figure 2.3: Energy loss of 3 GeV electrons in a small drift chamber of the SAMBA experiment [9]. A Landau-distribution characterizes the measured data.

Figure 2.3 shows a Landau-distribution qualitatively, which was measured in a small drift chamber of the SAMBA experiment at CERN.
In the case of gaseous detectors, one can identify new tracks if the energy transfer is too high. The electron is then able to ionize further atoms and causes a new track to arise from the first one. These so-called delta electrons restrict the tail of the Landau-distribution as the tail is derived from large energy transfers, which are now identified as new tracks. This also has an impact on the mean energy loss measured by the detector. Depending on the detector parameters, one inserts a cut off Energy $E_{\max}$ in the Bethe-Bloch equation (2.2). The newly restricted form of the equation can be expressed in the following way [5]:

$$\left(\frac{\mathrm{d}E}{\mathrm{d}x}\right)_{\text{restricted}} = \frac{4\pi N e^4 z^2}{m_\mathrm{e} c^2 \beta^2}\left\{\ln\left(\frac{\sqrt{2m_\mathrm{e}c^2 E_{\max}}\beta\gamma}{I}\right) - \frac{\beta^2}{2} - \frac{\delta(\beta)}{2}\right\} \tag{2.6}$$

2.2 Ionization and Electron Attachment

The atoms of the gas volume can be ionized by the energy transfer from the charged particle. Different processes exist which are defined as primary and secondary ionization. A primary ionization occurs if the charged particle μ directly kicks out one or more electrons of the interacting atom A. One can see the possible primary ionization in the following formulas, while two or three fold ionization occurs less often [5].

$$\mu\mathrm{A} \rightarrow \mu\mathrm{A}^{+}\mathrm{e}^{-} \tag{2.7}$$
$$\mu\mathrm{A} \rightarrow \mu\mathrm{A}^{++}\mathrm{e}^{-}\mathrm{e}^{-} \tag{2.8}$$
$$\mu\mathrm{A} \rightarrow \mu\mathrm{A}^{+++}\mathrm{e}^{-}\mathrm{e}^{-}\mathrm{e}^{-} \tag{2.9}$$

Secondary ionization on the other hand describes several different processes. Two of theses processes, which we can observe, are presented. On the one hand primary electrons exist that received enough

kinetic energy to ionize other atoms through collisions.

$$e^- A \rightarrow e^- A^+ e^- \tag{2.10}$$

$$e^- A \rightarrow e^- A^{++} e^- e^- \tag{2.11}$$

The previously mentioned delta electrons are an example of this process if the secondary electron has a large kinetic energy. On the other hand secondary electrons can be produced through the Penning effect. The Penning effect can only occur if a gas mixture is used in the detector. Furthermore, one of the components A has to possess a metastable excited state (A^*) whose energy is higher than the ionization potential of another gas component B. The effect is most commonly observed when using a noble and an organic gas, as noble gases have high excitation states and organic gases low ionization potentials [6]. Collisions of the excited noble atoms and the organic molecules cause the ionization of the organic molecule and the de-excitation of the noble atoms.

$$\mu A \rightarrow \mu A^* \tag{2.12}$$

$$e^- A \rightarrow e^- A^* \tag{2.13}$$

$$A^* B \rightarrow A B^+ e^- \tag{2.14}$$

The ionization electrons can also interact with the gas and are attached to molecules. As only the free electrons produce the signal in the detector, the electron attachment reduces the signal to noise ratio. The noble gases do not form stable negative ions and the drifting electrons do only reach enough kinetic energy to ionize the other components inside the amplification area of the detector. Most of the time halogen compounds and oxygen with large negative electron affinities are ionized. These gas components are only rarely used in gaseous detectors but can be found as gas impurities due to imperfect gas systems.
The simplest processes of electron attachment are two-body collisions. The electron is absorbed by a molecule M and is sometimes able to dissociate the molecule into smaller parts A, B ... and one of the constituents becomes a negative ion:

$$e^- + M \rightarrow M^- \tag{2.15}$$

$$e^- + M \rightarrow A^- + B \tag{2.16}$$

The first process is very unlikely as an electron has a kinetic energy and would also excite the molecule. In typical cases, the molecule has to interact again to reach the stable state. The energy of the electron for a dissociative attachment has to be quite high ($\sim$ 5 eV [10]) and is not reached in the drift region of a standard TPC configuration, whereas in the amplification process the electron energy rises high enough to dissociate the molecule. As the amplification region is a lot smaller than the drift region, the dissociative process reduces the amplification but not the number of primary electrons. To describe measurements a three body process model was developed by Bloch and Bradbury in 1935 [11]. Due to the later experiment, oxygen molecules O_2 will be used in the following description. First of all the electron is attached to the oxygen.

$$e^- + O_2 \rightarrow O_2^{-*} \tag{2.17}$$

with O_2^{-*} being one of the low vibrational states of the oxygen molecule. The lifetime of the excited oxygen is in the order $\tau = 10^{-10}$ s. Without further interactions the excited oxygen will then either emit

the electron or a photon to reach a stable state.

$$O_2^{-*} \rightarrow e^- + O_2 \tag{2.18}$$
$$O_2^{-*} \rightarrow \gamma + O_2^- \tag{2.19}$$

The higher the density of the gas, the higher the possibility of a collision of the excited molecule with a component X of the gas. This collision can either release the electron from the ion or it stabilizes the oxygen ion.

$$O_2^{-*} + X \rightarrow e^- + O_2 + X \tag{2.20}$$
$$O_2^{-*} + X \rightarrow O_2^- + X^* \tag{2.21}$$

The second reaction only happens if a resonant collision is possible. Therefore, the type of molecule X is rather important for the cross section of the process. Large molecules have a lot of vibrational states and tend to increase the cross section considerably. Huk showed that 1000 ppm of water can double the electron capture rate of oxygen impurities as resonant collisions happen more frequently [10]. If the rate of spontaneous decay $1/\tau$ is low compared to the rate of third body collision, the electron capture rate R can be written as [5]:

$$R = \tau c_1 c_2 \sigma_1 \sigma_2 N(O_2) N(C) \tag{2.22}$$

with c_1 as the electron velocity, c_2 the velocity of thermal motion, σ_1 the cross section of O_2^{-*} generation, σ_2 the cross section of stabilizing third body collisions and $N(O_2)$ and $N(C)$ the density of oxygen and third body molecules. As all the parts of the equation show strong dependence on operating conditions, e.g. pressure, temperature and electron energy, the rate is often measured experimentally.
Observations showed that this model of third body collisions is not sufficient. That is the reason for an expansion of this model with the creation of unstable van der Waals molecules. The reaction chains for attachment due to van der Waals molecules are:

$$O_2 + X \rightarrow (XO_2) \tag{2.23}$$
$$(XO_2) + e^- \rightarrow O_2^- + X \tag{2.24}$$
$$(XO_2) + e^- \rightarrow (XO_2)^{-*} \tag{2.25}$$
$$(XO_2)^{-*} + X \rightarrow O_2^- + 2X \tag{2.26}$$

with molecules in brackets being van der Waals molecules. The conditions of the detector have a strong influence on the importance of the van der Waals molecules but a higher pressure increases the cross section.

2.3 Electron and Ion Drift and Diffusion

Inside a TPC an electric field $\vec{E}$ is applied to move the electrons to the detection plane. A magnetic field $\vec{B}$ is also used to bend the tracks of particles on a helix trajectory, from which one is able to calculate the momentum of the particle. The equation of motion for the electrons and ions inside the volume is expressed by the Langevin equation:

$$m\frac{d\vec{v}}{dt} = e\vec{E} + e[\vec{v} \times \vec{B}] - K\vec{v} \tag{2.27}$$

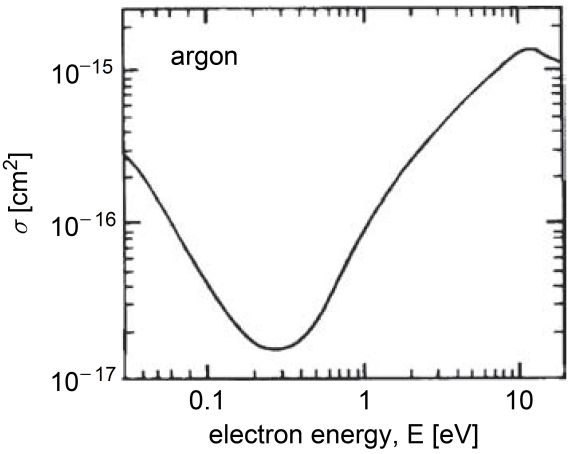

Figure 2.4: Cross sections of electron-Argon scattering with respect to the electron energy. The minimum relates from quantum mechanical description and was first discovered by Ramsauer [12].

with m being the mass of the charged particle, e the charge of the particle, $\vec{v}$ the velocity vector and K is the friction force created by the interactions of the charged particles with the atoms of the gas. The coefficient K can be expressed with the mass m and the mean time between two collisions τ in the following way:

$$K = \frac{m}{\tau} \tag{2.28}$$

If one assumes a large time $t >> \tau$ and that a constant electric field generates a constant drift velocity, a solution of the equation of motion is [5]:

$$\vec{v} = \frac{e}{m}\left|\vec{E}\right| \frac{1}{1+\omega^2\tau^2}\left(\frac{\vec{E}}{\left|\vec{E}\right|} + \omega\tau\left[\frac{\vec{E}}{\left|\vec{E}\right|} \times \frac{\vec{B}}{\left|\vec{B}\right|}\right] + \omega^2\tau^2\left(\frac{\vec{E}}{\left|\vec{E}\right|} \cdot \frac{\vec{B}}{\left|\vec{B}\right|}\right)\frac{\vec{B}}{\left|\vec{B}\right|}\right) \tag{2.29}$$

where $\omega = (e/m)B$ is the cyclotron frequency. In the case of the experiment which will be discussed later, and where no magnetic field is applied, the solution is simplified to:

$$\vec{v} = \frac{e}{m}\tau\vec{E} = \mu\vec{E} \tag{2.30}$$

$$\mu = \frac{e}{m}\tau \tag{2.31}$$

This defines the mobility μ of the ions and electrons inside the electric field. As charge and mass of the charged particles are universal constants the mobility of one type of particles only depends on the mean time between collisions. Figure 2.4 shows the dependence of the cross section of interactions on the kinetic energy of the particles. One can clearly identify a distinct minimum which is called Ramsauer minimum, named after its discoverer Carl Ramsauer. This minimum is generated by a quantum mechanical scattering when the de Broglie wavelength of the electron is in the same order as the wavelength of the atoms of the gas. Historically, this was one of the first experiments which proved that classical mechanics cannot explain the behavior of electrons.
Equation (2.31) also indicates that the mobility, and thus the velocity of ions is three orders lower than the mobility of electrons due to the mass difference.

The ionization electrons and ions do not only move due to the electric field but also due to thermal energy. The initial energy of the particles can be neglected as the particles lose their kinetic energy fast by scattering processes with the gaseous volume. Without the electric field, the ions and electrons posses the thermal velocity distribution explained by the Maxwell-Boltzmann distribution. In the case of a room temperature experiment the mean energy $\overline{E}$ is:

$$\overline{E} = \frac{3}{2} k_{\mathrm{B}} T \approx 40\,\mathrm{meV} \tag{2.32}$$

with k_{B} the Boltzmann constant and T the temperature. During the drift process the ions and electrons behave rather differently because of their masses. The electron motion will be discussed first.
Due to the light mass of the electrons in comparison with the atoms of the gas, the electrons scatter elastically and isotropically. In the case of a bunch of electrons, the electrons will diffuse inside the gas by collisions. After a time t the density distribution n of the electrons reaches a Gaussian distribution in the following form:

$$n = \left(\frac{1}{\sqrt{4\pi D t}}\right)^3 \exp\left(\frac{-r^2}{4Dt}\right) \tag{2.33}$$

$$r^2 = x^2 + y^2 + (z - vt)^2 \tag{2.34}$$

with z the drift direction, v the drift velocity and D the diffusion coefficient. The diffusion coefficient was chosen so that n satisfies the continuity equation.
Experiments have shown that the diffusion coefficient in the drift direction can differ quite a lot from the diffusion in the transverse direction. Partker and Lowke [13] found a model which can explain the discrepancy. They assume that the cross section of the electrons depend on the kinetic energy of the electrons in the observed energy range. This would create a different scattering probability for electrons at the front and at the back of the drifting electron cloud. A change of the longitudinal diffusion would be the consequence. With these assumptions the equation (2.33) changes to:

$$n = \frac{1}{\sqrt{4\pi D_L t}} \left(\frac{1}{\sqrt{4\pi D_T t}}\right)^2 \exp\left(-\frac{x^2 + y^2}{4D_T t} - \frac{(z - vt)^2}{4D_L t}\right) \tag{2.35}$$

with D_T being the transverse diffusion coefficient and D_L the longitudinal diffusion coefficient. The variance σ of the diffusion is:

$$\sigma_{\mathrm{xy}} = \sqrt{2D_T t} = \sqrt{\frac{2D_T z}{\mu E}} = D_T^{'} \sqrt{z} \tag{2.36}$$

$$\sigma_{\mathrm{z}} = \sqrt{2D_L t} = \sqrt{\frac{2D_L z}{\mu E}} = D_L^{'} \sqrt{z} \tag{2.37}$$

with t the drift time, z the drift distance, μ the mobility and E the electric field. The constants $D_T^{'}$ and $D_L^{'}$ are commonly used in detector physics as a simplification of data. In the following thesis they will be called diffusion constants and will be addressed as D_T and D_L.
The ions have a similar mass compared to the atoms of the gas. Therefore, the ions lose a certain amount of energy during each collision and do not scatter isotropically. Now one can distinguish between two cases. The first one is a low drift field where the random velocity of the ions is created by the thermal motion. The second case is a high drift field, which can be ignored in this context as the experiment

does not reach these field strengths. The velocity v of the drifting ions in low electric fields is described by:

$$v = \left(\frac{1}{m} + \frac{1}{M}\right)^{\frac{1}{2}} \left(\frac{1}{3k_B T}\right)^{\frac{1}{2}} \frac{eE}{N\sigma} \tag{2.38}$$

with m the mass of the ions, M the mass of the atoms in the gas and T the temperature.
The Nernst-Townsend formula or Einstein formula describes the connection of the diffusion coefficient with the mobility of the particles in a classical way:

$$D = \frac{k_B T}{e}\mu \tag{2.39}$$

This shows that the ions diffuse less than the electrons because of the low mobility. In gas mixtures the mobility $\overline{u}$ of the ions can be approximated with Blanc's law:

$$\frac{1}{\overline{u}} = \Sigma \frac{N_k}{N} \frac{1}{u_k} \tag{2.40}$$

with u_k the mobility and N_k the density of the gas component k and N the full density. If complex molecules are added to the mixture, all ions can transfer their charge to the molecules by collisions. The molecule's ionization potential must be lower than the ionization potential of the ions. 100 to 1000 collisions of the ions with molecules are needed to transfer the charge [14]. This mainly depends on the difference in the ionization potential. In a standard TPC configuration with a mean free path of the ions of the order 10^{-5} cm and gas fractions of > 1 %, the charge transfer to the lowest ionization potential is fulfilled before 1 cm of drift of the ions. Thus, the mean drift velocity of the ions is mainly determined by the drift velocity of the molecule with the lowest ionization potential. Typically, the molecules possess the highest mass of the components of the gas mixture. Thus, the ions drift velocity is mainly determined by the drift velocity of that molecule.

2.4 Gas Amplification

The few electrons of the ionization cannot be detected as the signal produced is too low in the electronics. Therefore, a structure for electron multiplication is used which is called gas amplification stage. Several different amplification methods exist but gaseous detectors normally use a high electric field. The drifting electrons are accelerated in the presence of the field and are able to reach enough kinetic energy between two collisions to ionize atoms of the surrounding gas. This starts an avalanche of secondary electrons and ions which are responsible for the signal in the readout structure. The multiplication of electrons is described by the first Townsend coefficient α:

$$\frac{\mathrm{d}N}{\mathrm{d}x} = \alpha N_{\mathrm{tot}} = \frac{N_{\mathrm{tot}}}{\lambda_{\mathrm{ion}}} \tag{2.41}$$

with $\mathrm{d}N/\mathrm{d}x$ the number of secondary ionizations per track length, N_{tot} number of atoms and λ_{ion} the mean free path for ionization. The Townsend coefficient depends strongly on the detector configuration. A drawback is that the dependency of the Townsend coefficient on electric field cannot be analytically calculated for high electric fields. For that reason one defines the gas gain G as a measurable value. It characterizes the quotient of number of incoming electrons N_0 and number of outgoing electrons N

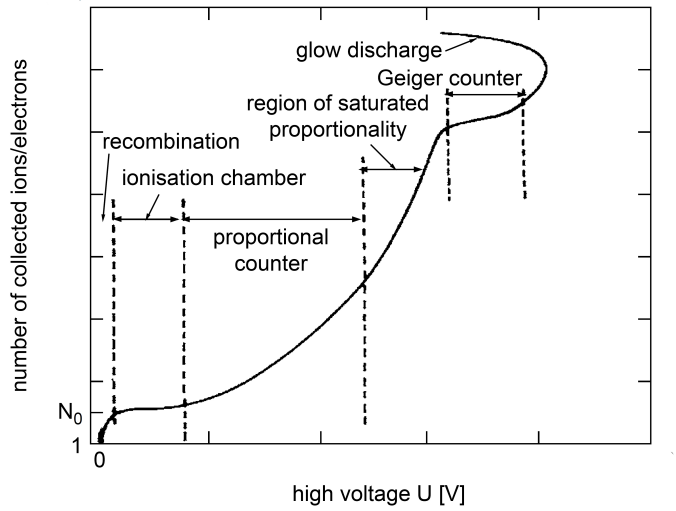

Figure 2.5: Working regions of a cylindrical gaseous detector [15]

between place r_1 and r_2.

$$G = \frac{N}{N_0} = \exp\left(\int_{r_1}^{r_2} \alpha(x)\mathrm{d}x\right) = \exp\left(\int_{E_1}^{E_2} \frac{\alpha(E)}{\mathrm{d}E/\mathrm{d}x}\mathrm{d}E\right) \tag{2.42}$$

The gas gain varies with the electric field and one distinguishes several regions as seen in figure 2.5. For very low electric fields the probability of recombination of ions and electrons is high due to the coulomb attraction. With increasing field strength the recombination is suppressed and one reaches the region of proportionality. In this region the signal is proportional to the number of electrons created by a traversing charged particle. This is an interesting region for gaseous detectors trying to measure the energy deposition of the charged particle. If the electric field becomes higher, the signal loses its proportionality to the number of electrons. Due to the large number of ions in the avalanche the electric field is distorted strongly enough to stop further ionization. This region is called the Geiger mode. It is used in Geiger counters where one only wants to know if a particle went through the detector. The efficiency is at its maximum in the Geiger mode but one cannot perform an energy loss measurement of the traveling particle. If the field is further increased, discharges occur which can lead to the destruction of the detector.
In uniform electric fields E the gas gain rises exponentially in the region of proportionality:

$$\tag{2.43}$$

$$G(E) = a \cdot \exp(bE) \tag{2.44}$$

with the parameters a and b being detector dependent.
The gas gain is only the mean of the gain distribution for a single electron. As the avalanche is a statistical process the gain distribution includes various information on the detector performance. The statistic of the avalanche was studied by several groups and theoretical predictions vary with the model. Two important models are provided by Legler [16] and Alkhazov [17]. In both models the gain distribution cannot be expressed analytically. One can just extract statistical moments of the gain distribution from the models, but the Pólya-distribution $P(G)$ proved to be a good approximation for both models and

experimental data.

$$P(G) = \frac{1}{\overline{G}} \frac{(\Theta+1)^{\Theta+1}}{\Gamma(\Theta+1)} \frac{G^{\Theta}}{\overline{G}} \exp\left(-\frac{(\Theta+1)G}{\overline{G}}\right) \tag{2.45}$$

with $\overline{G}$ the mean gas gain, $\sigma^2 = \overline{G}^2/(\Theta+1)$ the variance and $\Gamma(\Theta+1)$ the Gamma function.
An important factor for the amplification is also the creation of UV-photons. Excited atoms in the avalanche are able to emit photons. These photons can have enough energy to ionize the gas or release electrons from metal inside the gaseous detector through the photo effect. This is an unwanted process as it produces a second avalanche inside the detector at a position where no primary electron was created. A reduction of the spatial and energy resolution of the track is the consequence. It can also cause breakdowns if too many high energy photons are emitted. Avalanches will keep occurring until the detector breaks down. Therefore, one uses quenching gases to reduce this effect. Quenching gases are made of molecules with absorption lines in the UV-range. Vibrational states of the molecules are excited and only the emission of less energetic photons or collisions cause the decay of the state. Standard quenching gases for a gaseous detector are CO_2, CH_4 or iC_4H_{10}.

2.5 Signal Development

Moving charged particles induce a signal in the electrode. The avalanche of the gas amplification has to create enough charged particles so that the signal can be amplified and read out.
As already stated, the signal originates from induction effects. The electric field of a charged particle induces a surface charge on the metal of a grounded electrode. If the electric field $E(x,y,z)$ or the surface charge density $\sigma(x,y,z)$ at the metal surface is known, one can calculate the induced charge Q.

$$Q = \int_A \epsilon_0 E(x,y,z)\mathrm{d}A = \int_A \sigma(x,y,z)\mathrm{d}A \tag{2.46}$$

with A being the surface of the observed electrode. Now one should consider the case of a moving charged particle inside the detector with a velocity v and the trajectory of $z(t) = z_0 - vt$. In standard detectors the induced charge is dependent on the z-position of the charge (exceptions are for example enclosing single electrodes as a hallow sphere). Thus, the moving particle induces a time dependent charge in the electrode, which can be detected as an induced current I_{ind}.

$$I_{ind} = -\frac{\mathrm{d}}{\mathrm{d}t}Q(z(t)) = -\frac{\partial Q}{\partial z}\frac{\mathrm{d}z(t)}{\mathrm{d}t} = -\frac{\partial Q}{\partial z}v \tag{2.47}$$

The minus sign results from the fact that the induced charge Q moves in the opposite direction with respect to the charge q.
The idea of this method is quite simple but can be difficult do calculate for complex detector structures. With the use of Ramo's theorem, one can simplify the calculation of the induced current. One just has to calculate or simulate the potential inside the detector for a special case. One puts the electrode i of interest on $U = 1\,\mathrm{V}$, all other metals on ground potential and removes the drifting charges. One receives the weighting potential ψ. With this, one gets the induced charge with the relation

$$Q_\mathrm{i} = -q\psi_\mathrm{i}(z) \tag{2.48}$$

with q being the charge of the drifting charge. The derivative of the induced charge with respect of the time gives the induced current.

$$I_{\mathrm{i}}^{\mathrm{ind}}(t) = -\frac{\mathrm{d}Q_{\mathrm{i}}}{\mathrm{d}t} = q\nabla\psi_{\mathrm{i}}[z(t)]\frac{\mathrm{d}z(t)}{\mathrm{d}t} = -qE_{\mathrm{i}}[z(t)]v(t) \tag{2.49}$$

with Ramo's theorem as $E_{\mathrm{i}} = -\nabla\psi_{\mathrm{i}}(z(t))$ [18]. An important fact is that the electrons reach the electrode in a timescale of nanoseconds. The induced signal is thereby very short and hard to measure. The ions on the other hand drift slowly in the gaseous detector. They induce a signal whose timescale is in the order of a microsecond. As the ions drift away from the readout electrode, the integrated induced charge must be equal to zero. So the signal is bipolar which must be considered during the choice of the charge sensitive amplifier.

2.6 Time Projection Chamber

The Time Projection Chamber (TPC) is probably the most sophisticated gaseous tracking detector and was invented by D. Nygren in 1974 [19]. TPCs have the benefit of a very low material budget combined with a relatively good spatial resolution and many track points. Figure 2.6 shows a sketch of a TPC as it would be used in a collider experiment. The TPC has a cylindrical shape and is divided in two separated drift volumes by a central cathode. Inside the TPC there is another cylinder which contains the beam pipe. Charged particles from the interaction point of the collider traverse the gaseous volume and ionize the atoms along their tracks. An electric field between the central cathode and the anodes cause a drift of the electrons towards the detection region. The ions drift slowly towards the cathode and are neutralized. The segmentation of the TPC in two parts shortens the maximal drift time of ions and electrons and diffusion is less prominent. In typical TPCs a magnetic field is applied parallel to the electric field. On the one hand this provides the possibility of momentum measurement from the curvature of the traveling particle. The magnetic field, on the other hand, also reduces the electron diffusion. Electrons are forced on a helix-shaped trajectory between two collisions in the presence of the magnetic field. The magnetic field's influence on the transverse electron diffusion D_T is:

$$\frac{D_{T,mag}}{D_T} = \frac{1}{1+\omega^2\tau^2} \tag{2.50}$$

with $\omega = eB/m$ the cyclotron frequency and τ the mean time between collisions of electrons with the gas [5].
At the end caps the drifting electrons reach an amplification structure. The avalanche of the gas amplification induces a signal in the electrodes which is read out by the electronics. In a cylindrical coordinate system with z being in the cylinder direction one has now produced an image of a projection of the track in the $r\phi$-plane. An external trigger system allows a measurement of the drift time t' and thus the z-position of the track with the knowledge of the drift velocity $v(t)$.

$$z = \int_0^{t'} v(t)\mathrm{d}t \tag{2.51}$$

Theory predicts a constant velocity in a homogeneous electric field and the simple relation $z = vt'$ remains. Now one has three dimensional image of the event inside the chamber.
The electric field inside the TPC should be as homogeneous as possible. Otherwise the drift velocity

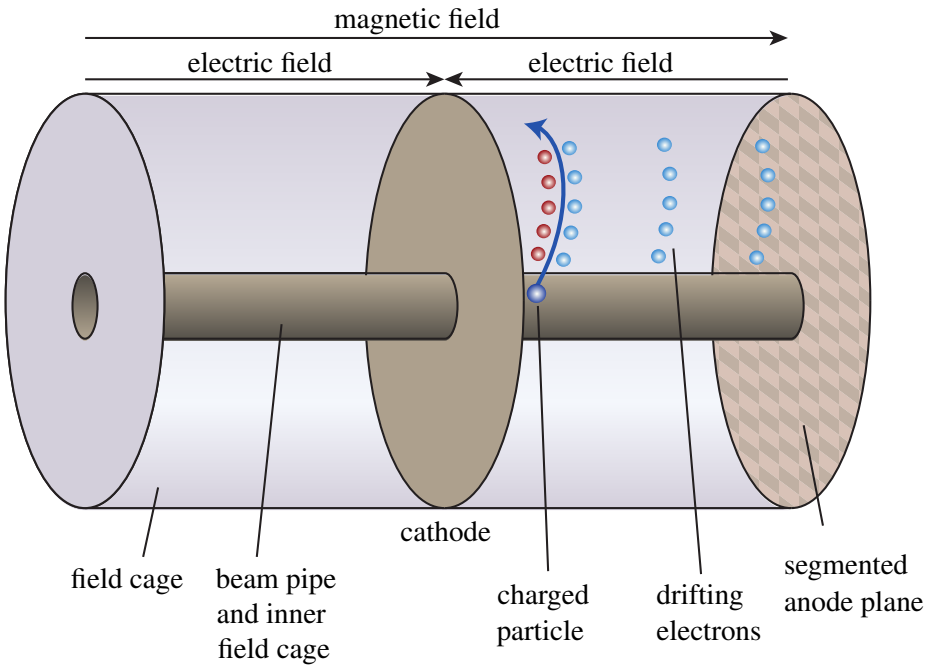

Figure 2.6: Schematic of a Time Projection Chamber as planned for the International Large Detector [20]

of the electrons varies too much, which reduces the resolution of the track. Therefore, one uses a field cage along the drift volume. The field cage consists of metallic rings which are held on the potential corresponding to the field inside the detector. This is done with a resistor chain along the field cage. In the case of the ILD the field cage must be very thin to fulfill the requirements of a material budget of less than 3 % radiation length. Furthermore, the cathode is on a potential as high as 100 kV.
The Time Projection Chambers created by Nygren used wires as the amplification stage. Figure 2.7 shows the setup of the amplification and readout stage of a traditional TPC on the left side and the electric field lines on the right side. The sense wires are on a high electric potential and the electrons create avalanches in the vicinity of the wire. The field lines are placed alternating with the sense wires to generate the correct field configuration. One does not use the wire signals to identify the $r\phi$-position of the electrons but the induced signals in the anode plane. The anode plane is on ground potential and is segmented into pads, which enhances the spatial resolution compared to the wire readout. Due to information from neighboring pads, one can even reach a resolution below the limit of a single pad. The zero grid decouples the drift field from the amplification field. This enables a homogeneous drift field with a high permeability of the electrons. The major drawback of this configuration are ions from the avalanches. If they are not collected by the pads they can travel inside the drift volume and cause field distortions. This effect is called ion backflow. Charged space points destroy the homogeneity of the field with respect to the direction and the strength of the field. The $r\phi$-position is reduced if the direction of the field changes and the trajectory of electrons is bent. The distortion of the field strength alters the electron velocity and worsens the z-resolution of the TPC. To avoid or at least minimize the influence of the ion backflow one implements gating grids above the zero grid. The gating grid receives an alternating potential. If the gate is opened, the potential of the grid has to be aligned with the drift field. After all the electrons are amplified the grid is switched to a negative potential to collect the ions. Figure 2.8 shows the field lines of a gating grid in the opened (left) and closed (right) state. The ions are very slow and need time to reach the grid. Hence, a high frequency of the gating grid cannot be

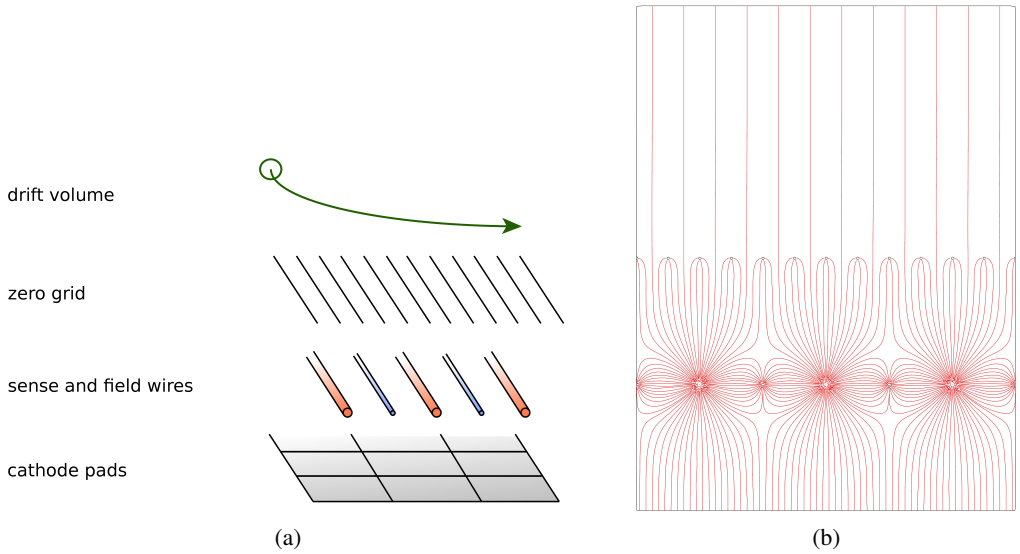

Figure 2.7: a) Schematic of the amplification and readout plane of a standard TPC. b) Field lines of the corresponding setup [20, 21].

achieved. For the ILD a gating grid is also considered, but one would only be able to close the grid between two bunch trains ($t = 200\,\text{ms}$) and not between two bunches ($t = 350\,\text{ns}$) [22].
As the end cap has to provide the complete readout for the TPC the material budget is higher compared to the field cage. Nevertheless, a TPC has the benefit of a low material budget, a nearly 4π coverage of space and many track points ($20 - 200\,\text{cm}^{-1}$ dependent on the gas). An example of a TPC with the depicted setup is the ALICE TPC used in the ALICE experiment at the LHC.
The transverse resolution of a TPC is limited by the structure of the signal wires. That is why new technologies of amplification structures are being researched for the ILD. Micro Pattern Gaseous Detectors (MPGD) will replace the wire structure. Two different MPGDs are presented: GEM amplification and Micromegas.

2.6.1 Gas Electron Multipliers

Gas Electron Multipliers (GEM) were developed by F. Sauli in 1996 [23]. They consist of an insulating Kapton foil with copper layers on both sides. Holes are etched into the foils in a hexagonal structure. Figure 2.9a is an electron microscopic picture of a standard CERN GEM. The sizes of the layers and the holes are also included in the picture.
A voltage is applied between both sides of the GEM and a strong electric field inside the holes causes gas amplification. The voltages of a GEM ranges between $300 - 500\,\text{V}$ and the gain can reach up to 10^3. To reduce the probability of discharges of a GEM, one often uses a stack of two or three GEMs with a distance of $1 - 2\,\text{mm}$ between two GEMs. It is then possible to reduce the voltage of one GEM and use the multiplication of the gas gain to achieve a total gas gain of the order $10^5 - 10^6$.
Figure 2.9b shows the field lines of a single GEM and electrons and ions of the avalanche. The incoming electron is forced inside the hole by the electric field. The electron gets enough kinetic energy to start an avalanche of ionization. The electrons of the avalanche are then extracted to the volume behind the GEM and only $\sim 50\,\%$ electrons are neutralized at the bottom copper layer of the GEM. The ions, on the other hand, are often caught by the top copper layer and only a few reach the drift volume of the TPC.

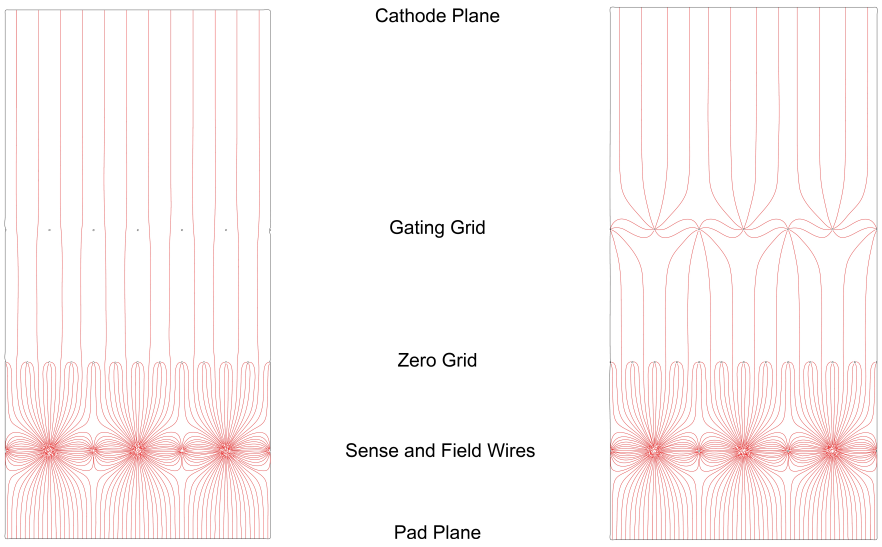

Figure 2.8: Field lines of the two modes of operation of a TPC with gating grid. a) Gating grid opened and c) gating grid closed [21].

Thus, GEMs posses an intrinsic reduction of the ion backflow. For a stack of GEMs one can increase the reduction by tuning the transfer fields between the different GEMs and by reducing the amplification of the first GEM.
GEMs can be teamed up with a pad or a pixel readout. The distance of the GEMs to the readout is also in the order of one millimeter as the GEMs can bend and discharges must be avoided. Therefore, diffusion of electrons is large and the avalanche width reaches easily ~ 1 mm.

2.6.2 Micromegas

A second type of Micro Pattern Gaseous Detectors are Micromegas (Micromesh Gaseous Structures). Micromegas detectors are based on a parallel plate detector. One of the plates serves as the readout electrode and a high voltage between the plates makes gas amplification possible. In a TPC application the drifting electrons have to be inserted in the parallel plate, hence the top plate is replaced by a mesh. Micromegas detectors are consequently a fine mesh above a readout plane with a high electric field between them. Many different production techniques have been developed in the last 15 years, but they all share the same setup. The readout electrode of Micromegas is typically a pad or strip structure with several 100 µm width. Then a pillar or wall structure is placed on top of the readout structure to support the mesh and ensure a homogeneous mesh height. The mesh is then put onto the spacers. Standard meshes are a few micrometers thick and the hole pitch is in the order of 50 µm (see figure 2.10). The production techniques of the Micromegas started with quartz fibers as the gap spacers glued on a PCB and the mesh mounted on top. Lithographic techniques were later used to create pillar structures onto the PCB to lower the gap inhomogeneities. Furthermore, the mesh and the supporting structure can be created in one process by lithographic etching of a Kapton foil with copper layers. This foil can then be glued onto a PCB to form a Micromegas detector. The latest developments of Micromegas are so-called Microbulk Micromegas. They are also produced by lithographic processing of Kapton foils with copper layers [26]. The difference is that the readout structure is also created by etching of the copper and PCBs

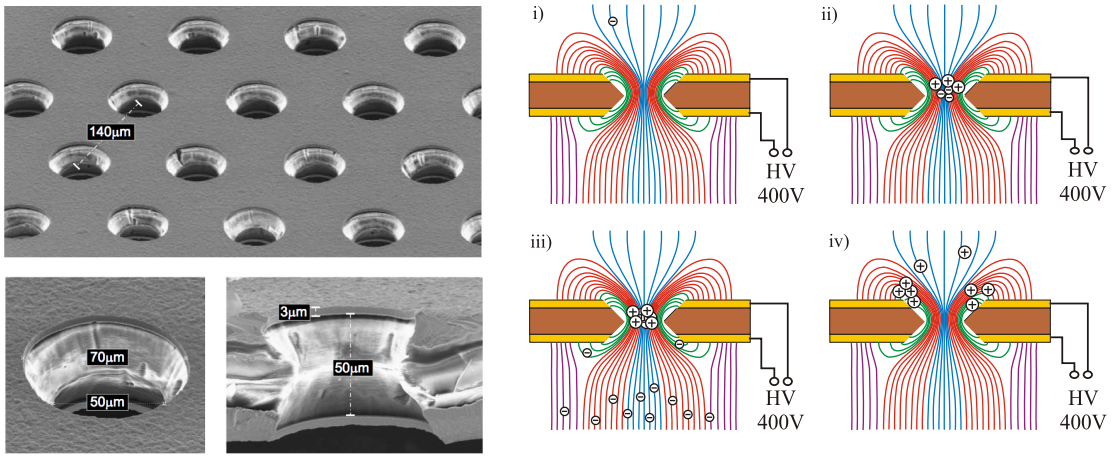

Figure 2.9: a) Electron-microscopic pictures of a GEM [24]. b) Schematic drawing of the field lines and the gas amplification process inside one hole of a GEM [25].

are not needed anymore. The advantage of the new Microbulk Micromegas is the low material budget and radiation purity of the used materials.
The Micromegas were tested in many radiation source and test beam experiments. One important fact is the understanding of the electric field in the detector. The field configuration at the mesh is of the utmost interest. The ratio between the field strength in the drift volume and in the amplification volume influences the field lines at the mesh. In a standard setup the field in the amplification volume is a lot higher. Therefore, most of the field lines from the drift volume are bent into the holes of the mesh. This happens at a short distance above the mesh and does not influence the drift behavior of the electrons. As nearly all the field lines reach the amplification volume, the electron transparency of the mesh is very high [28]. On the other hand, most of the field lines from the amplification volume end at the top of the mesh. This serves as an intrinsic ion backflow reduction. Only with a reduction of the ion backflow, high rate experiments are possible for TPCs. It was shown that Micromegas can be used in high rate experiments and proved to resist discharges between the mesh and the charge collecting electrode [29]. As the standard pad readout structure is larger than the mesh, the spacial resolution of the Micromegas are restricted by the pad size. That is the reason for the development of a pixel chip based Micromegas detector. This structure is called InGrid and is the reason for this work. The InGrids will be presented more precisely in Chapter 3.2.

2.7 Gas Configurations

The choice of the gas is an important step in the design of a gaseous detector. As already stated, one normally uses a combination of a noble gas and an organic gas or CO_2 as a quencher but in special application even pure organic gases have been used. Several properties of the gas mixtures have to be considered to find the best suited for the experiment.
In general one distinguishes between hot and cold gas mixtures. The names refer to the velocities of the electrons in the gas. While electrons have low drift and thermal velocities in cold gases, the opposite is true in hot gases. A low thermal velocity is an advantage as this means a reduced diffusion

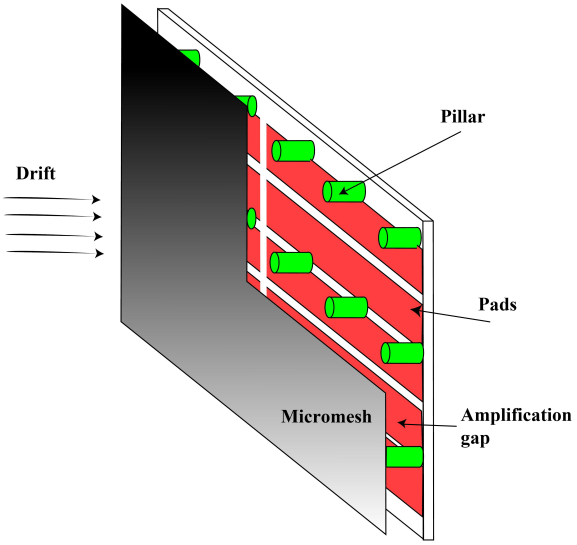

Figure 2.10: Schematic view of a Miromegas detector [27].

coefficient, which enhances the spatial resolution of the TPC. As a strong magnetic field greatly lessens the diffusion coefficient (formula (2.50)), even large TPC do not suffer from running with hot gases. In a high frequency experiment, such as the ILC, one also wants to have a high drift velocity. This reduces the time needed for the readout of one event and thus the dead time of the detector. The drift velocity does not only depend on the gas mixture but also on the electric field strength, gas pressure and temperature. To achieve the highest possible longitudinal resolution it is desirable to run independently of variations of the drift field caused by space charges. All gas mixtures exhibit a maximum in the relation between drift velocity and electric field. This is the most stable working point in the aspect of drift velocity, but in cold gases the maximum is found at very high electric field strengths. Therefore, the cold gases are not operated in this mode as the probability of discharges becomes too high.
One of the big advantages of TPCs compared to silicon detectors is the large number of track points. The mixture of the gas can greatly change the number of ionizations along the tracks. The organic gases have a low ionization potential and thus often enhance the number of electrons in the mixture. In standard TPC configurations the fraction of the organic gas is low. The noble gas is the dominating parameter for the number of electrons. The higher the mass of the noble gas, the more electron-ion pairs are created during the passage of the charged particle. Argon is widely used for large TPC as heavier noble gases are too expensive for large volume TPCs.

2.8 Cosmic Rays

During this work tracks of cosmic rays were observed. Therefore, a short introduction of cosmic rays is presented.
Cosmic rays are charged particles and nuclei created in stellar processes and accelerated at astrophysical sources. Through interactions with interstellar gas other types of charged particles are included in the cosmic rays, but the lifetime of the particles must be in the order of 10^6 to be detected at earth. The largest part of the total flux of the radiation is made of protons. When the radiation reaches the atmosphere of earth, new particles are created in interactions of the cosmic rays with the gas. Of primary importance are short lived mesons such as pions and kaons. While the neutral mesons mainly

decay in electrons, photons and lighter mesons, muons and muon neutrinos are the main decay products of the charged mesons. Due to helicity reasons, the decay of charged pseudoscalar mesons into leptons is suppressed with $\beta\gamma$ and thus with the inverse of the mass of the leptons. The decay channel into muons and muon neutrinos is strongly favored as a result. During the travel of the cosmic rays through the atmosphere, the particles lose their kinetic energy and can be absorbed. The flux of the particles decreases with the penetration depth and at earth level the muons provide around 99 % of the flux of the charged particles of cosmic radiation [7].
The energy and angular distribution at ground level is dependent on the production spectrum, energy loss in the atmosphere and the decay. The energy spectrum of the muons does vary with the incident angle and the mean energy of all muons at ground level is $\overline{E} \approx 4\,\mathrm{GeV}$. The total angular distribution of the muons is $\propto \cos^2(\Theta)$. In particular low energetic muons have a narrower angular distributions as higher angles correspond to a longer way in the atmosphere and a larger probability of decay. The integral intensity of vertical muons for vertical detectors is $I \approx 1\,\mathrm{cm}^{-2}\,\mathrm{min}^{-1}$.

Chapter 3

Experimental Setup

In this chapter the experimental setup is presented. The main parts of the detector, consisting of the prototype Time Projection Chamber, the Timepix chip and the InGrid structure, are explained in detail.

3.1 Timepix Pixel Chip

In an attempt to increase the spatial resolution of a TPC, a highly granular structure is tested. The Timepix [30] is the chosen pixel chip of research for the ILD and is also used during this thesis. The Timepix was developed at CERN and is the successor of the Medipix. Both chips are produced with a 0.25 µm CMOS technology and have an active area of $1.4 \times 1.4\,\mathrm{cm}^2$ consisting of 256×256 pixels. Thus, the pixel pitch is 55 µm in both directions. Figure 3.1a shows the Timepix chip on its carrier PCB. The chip is slightly larger ($1.6 \times 1.4\,\mathrm{cm}^2$) than its active area to provide pads, serving as connections to the PCB via wire bonds.
Each pixel consists of a metal bond pad of octagonal shape with a diameter of around 20 µm. The Medipix was developed for medical imaging purposes. It was intended to work as an electronic readout chip for gamma ray detectors based on a semiconductor. The detector can be placed onto the Medipix via bump bonding to the octagonal pixels. A charge sensitive amplifier in each pixel generates a voltage pulse, which is proportional to the input charge. The equivalent noise charge of the amplifiers is around 90 electrons. After each amplifier a single threshold discriminator is produced. The discriminator emits a digital pulse as long as the input signal is larger than a certain threshold. In normal applications the threshold is around 500 electrons in order to be five times larger than the equivalent noise charge. Figure 3.1b shows the analog circuit of the Timepix.
In the TPC application the metal bump pads are used as the charge collecting anode without the use of further sensor material. An amplification structure above the chip has to create enough electrons to induce a measurable current in the bond pads.
The main task of the Medipix is X-ray imaging. Therefore, the Medipix is able to count the number of input pulses which lie above the threshold of the discriminator. This can only create two dimensional images of an item. In a TPC one also wants to measure the time information to receive the third dimension of the track. Furthermore, a charge measurement is also interesting as $\mathrm{d}E/\mathrm{d}x$ information can be achieved. This was the reason for an upgrade of the Medipix to the Timepix. Each pixel in the Timepix is now able to run in one out of four different measurement modes. The two interesting modes for a TPC are the Time over Threshold and the Timepix mode (or Time of Arrival).
A pixel in the Time of Arrival (ToA) mode measures the time between the first overstepping of the threshold and the end of a shutter signal. For that purpose the number of clock cycles is counted. The clock signal is generated in the readout electronics. A shutter signal can either be injected by an external trigger system or by a software timer. The output is shifted serially into a 14-bit shift register. A pseudo random counter is used instead of the exact measurement of the pixel. This reduces the maximal countable number to 11800.

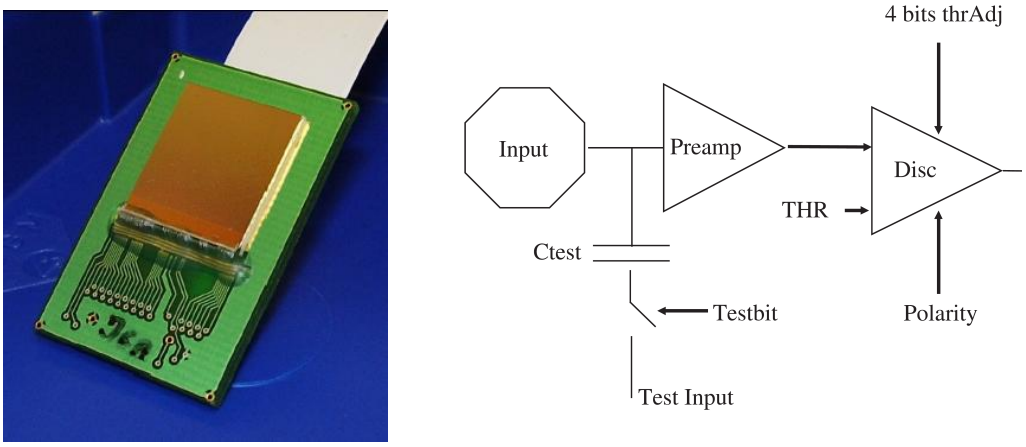

Figure 3.1: a) Picture of the Timepix chip on the carrier PCB. b) Analog part of the circuitry of the Timepix [30].

The Time over Threshold (ToT) mode is used to measure the amount of induced charge in one pixel. The pixel counts the number of clock cycles as long as the input signal stays above the threshold of the discriminator. The charge sensitive amplifier has a linear feedback created by a Krummenacher structure. Hence, the induced charge is nearly linear depending on the time of the signal above the threshold. The output only loses its linear behavior for small signals. The capacitor C_{test} in figure 3.1b allows us to couple a well-defined charge into the amplifier. This is achieved by injecting a pulse into the test input of the Timepix chip. With that one can calibrate the chip to convert the number of clock cycles into the amount of induced charge.
Figure 3.2 shows the timing scheme of the Timepix chip and the behavior in the ToT and ToA mode. One of the main drawbacks of the Timepix is its inability to discriminate between multiple hits. In the Timepix mode, only the first arrival of an electron is measured while in ToT mode the induced charges are added up. This is one of the reasons for the development of the so-called Timepix3. The successor of the Timepix will be commissioned in Spring 2012 and will be further specialized for the requirements of a TPC. The designed structure of the Timepix 3 is completely different compared to its predecessor, but some advantages will be a better time resolution, multiple hit recognition and the possibility to measure ToA and ToT with a single pixel at the same time.

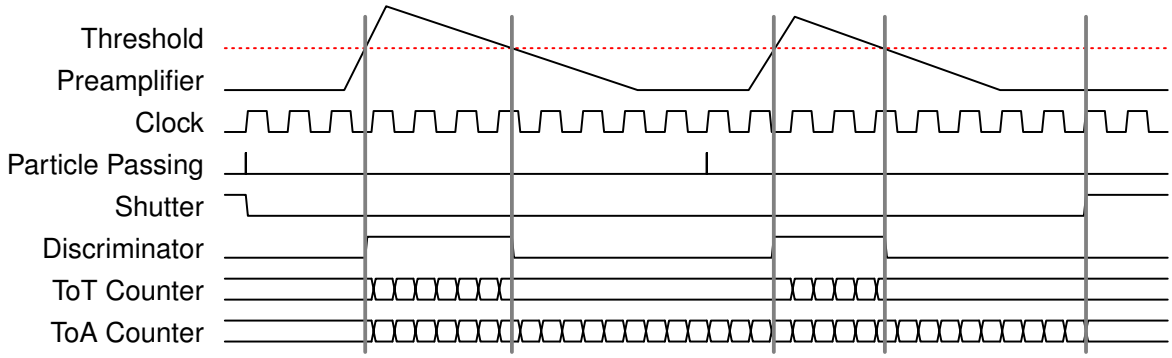

Figure 3.2: Timing scheme of the Timepix chip [31].

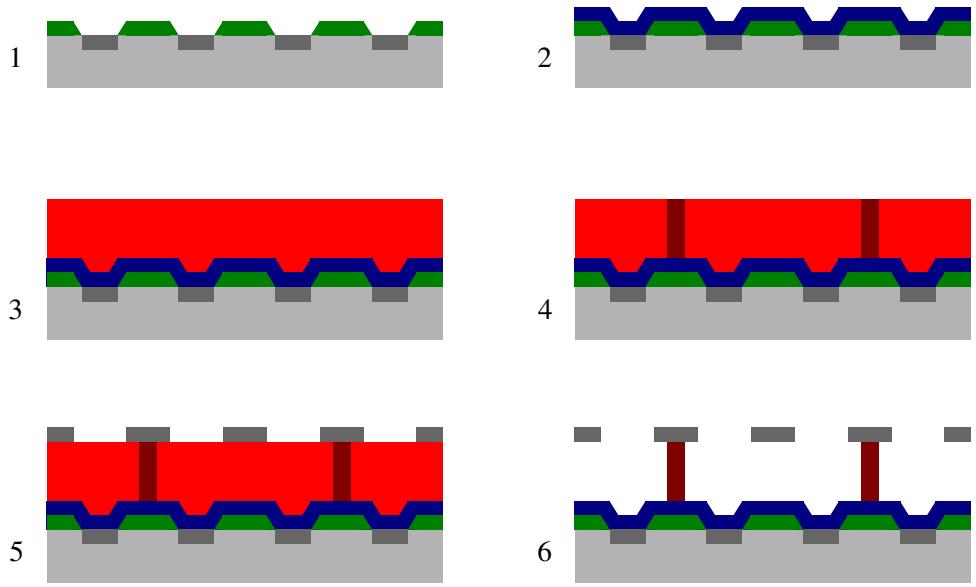

Figure 3.3: Scheme of the production process of InGrids. Light gray: Silicon chip, dark gray: metal bump bond pads and grid, green: passivation layer, blue: SiProt, light red: unexposed SU-8, dark red: exposed SU-8

3.2 InGrid

To use the Timepix in a TPC one must use a gas amplification stage to reach charges higher than the discriminator threshold. The possible technologies are described in section 2.6. The combination of GEM and Timepix was already tested successfully [32]. It was shown that a stack of three GEMs with separation distances of 1 mm creates an avalanche of the size of around 60 pixels. For the ILD this implies a very high occupancy of the chip during bunch crossings. A large dead time of single pixels as well as a redundancy of data is the consequence. To take advantage of the small pixel pitch one tried to create a Micromegas detector with the Timepix. If the Micromegas grid is close enough to the Timepix, one expects that only a single pixel is activated by the electron avalanche.
First attempts with Micromegas on a Timepix suffered from a bad alignment of the grid with respect to the pixel position. This gives rise to the Moiré effect. The Moiré effect is a special case of the Alias effect and describes the appearance of an interference pattern if two meshes are overlaid at an angle or have a different mesh size. This can greatly restrict the performance of the detector and has to be avoided.
As the alignment with simple mechanical structure is too complex a CMOS post- processing technique was chosen. Figure 3.3 shows a simplified sketch of the productions steps for InGrids. One starts with the bare Timepix chip with the passivation layer and the bump bond pads as the top layer. First, a small silicon nitride layer is put onto the Timepix. This layer is called SiProt and has the function of protecting the chip. In first attempts the SiProt was not used and discharges between the grid and the Timepix caused the breakdown of the chip. As the electric field between the Micromegas and the Timepix was very high, the discharges were too frequent to allow a long measurement with the InGrids. The SiProt has a high electrical resistivity. Avalanches charge the SiProt layer which discharges with a slow time constant. Furthermore, the charge on the SiProt is spread over several pixels and the current in one pixel is reduced. Tests showed that a single discharge can destroy the complete chip without the SiProt while a protected chip endures several.
Next, one places a photo resistive material upon the chip. The photo resist will later serve as the pillar

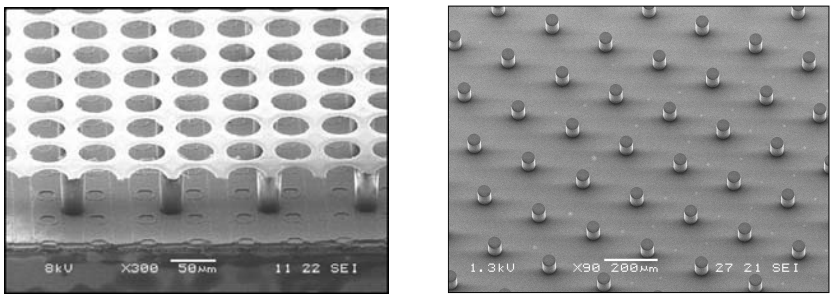

(a) (b)

Figure 3.4: An Electron-microscopic picture of an InGrid structure a) and the pillar structure without grid b) [33].

dimension	value
height of pillars	$(50 \pm 1)\,\mu m$
distance between pillars	$(110 \pm 1)\,\mu m$
thickness of SiProt	$(4 \pm 1)\,\mu m$
hole diameter of grid	$(30 \pm 2)\,\mu m$
hole distance of grid	$(55 \pm 1)\,\mu m$

Table 3.1: Dimension values of the InGrid used in this work. The errors are taken from [33].

structure to hold the grid at a homogeneous height. The pillars have to be insulators and mechanically stable. The chosen photo resist for the InGrids used is SU-8, which is spin coated on the chip. SU-8 is a negative tone photo resist that undergoes a cross-linking reaction after the exposure of light. A lithographic mask is used to develop the pillars in the SU-8 layer. The development of the SU-8 is done later as the unexposed SU-8 serves as a sacrificial layer for the metal grid.
A thin aluminum layer is sputtered onto the wafer to generate a grid. During this process UV- photons are created which then can cause unintentionally cross-linking in the unexposed SU-8. Therefore, a layer of positive photo resist is deposited on the SU-8 with a thickness of around 1 µm. It is exposed to light simultaneously with the SU-8 to create a protective layer. The grid structure is then wet etched into the aluminum. At the end the protective and sacrificial layer made of photo resist are developed and only the pillars remain. The pillars are set after every second bump pad. As the pillars are between two bump pads, they do not cause any dead area on the chip.
To stabilize the InGrids, a frame of $\sim 500\,\mu m$ width is created around the pillar structure. It also consists of the SU-8 and a metal layer but does not show the same structure. Expansion gaps in the frame reduce the stress caused by thermal expansion.
Figure 3.4a shows electron-microscopic pictures of an InGrid as it is used during this thesis while figure 3.4b shows the pillar structure on the chip. The thickness of the layers and the diameter of pillars and holes can be varied during the production process. The distance between two pillars is chosen so that the grid height stays homogeneous but as little material as possible is used. The chip used for the measurements was produced in a single chip process at the university of Twente. For larger scale applications the production of InGrids must be on wafer level. Therefore, first attempts being developed at the IZM which show promising results. Table 3.1 shows the values and errors of the InGrid's dimensions as it was used in this work.

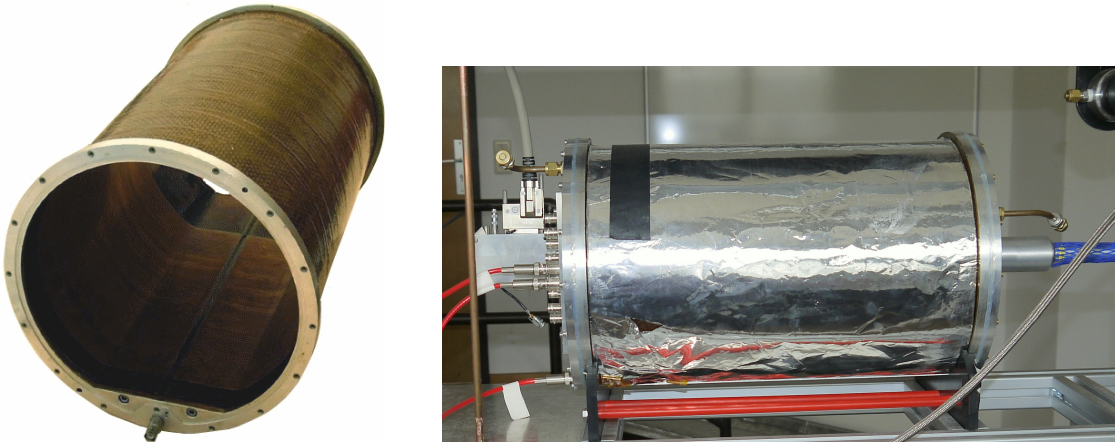

(a) (b)

Figure 3.5: a) Picture of the field cage developed at the RWTH Aachen. b) Picture of the TPC as it is used in this work. In the left end cap the readout structure is implemented.

3.3 Bonner TPC- Prototype

The measurements are performed with a prototype TPC from Bonn. The TPC's field cage was developed and built at the RWTH Aachen [34]. The main aspects of the field cage are a robust, gas tight structure and a homogeneous electric field despite of a low material budget. This was achieved by using a honeycomb structure made of Aramid as the stabilizing component. Several layers of Kapton, a layer of Fiberglass and a total of 187 copper rings aligned in two displaced row complete the mantle of the field cage. The field cage's mantle is around 40 cm long and the outer diameter is 26 cm. The cathode and anode plate reduce the maximal drift distance for electrons to 26.3 cm. A resistor chain connects the copper rings. The first ring is connected to the cathode plate while the ring number 186 can get a variable voltage through a SHV- connector. The voltages define the drift field inside the TPC. A high homogeneous electric field was a major goal of the development for the field cage. The design homogeneity was evaluated with simulations to be in the order of 10^{-4} and the light material reduces the material budget of the field cage to 1 % of radiation length. Until now, the actual homogeneity of the electric field has never been measured, but cross checks with the results of the GEM and Timepix readout has shown no signs of larger inhomogeneities due to the field cage.
The end caps of the TPC consist of 2 cm thick aluminum. Both caps have connectors for the gas supply and the cathode has a voltage connection through the end cap. The anode side end cap has a notch which serves as the inlet for different readout modules. A voltage connector for the InGrid is also implemented in the end cap while the readout of the Chip is done with a ribbon cable through the inlet. Figure 3.5a shows a picture of the field cage of the TPC while figure 3.5 shows the complete TPC as it is used in the experiments.

3.4 Setup

The measurements were done between May 2011 and August 2011 at Bonn. Figure 3.6 shows the complete setup of the experiment. The goal was to observe charged particles with enough kinetic energy to travel through the detector. For that reason and the necessity of an external trigger for time measurements, two scintillation detectors are placed above and below the TPC. The coincidence of both signals

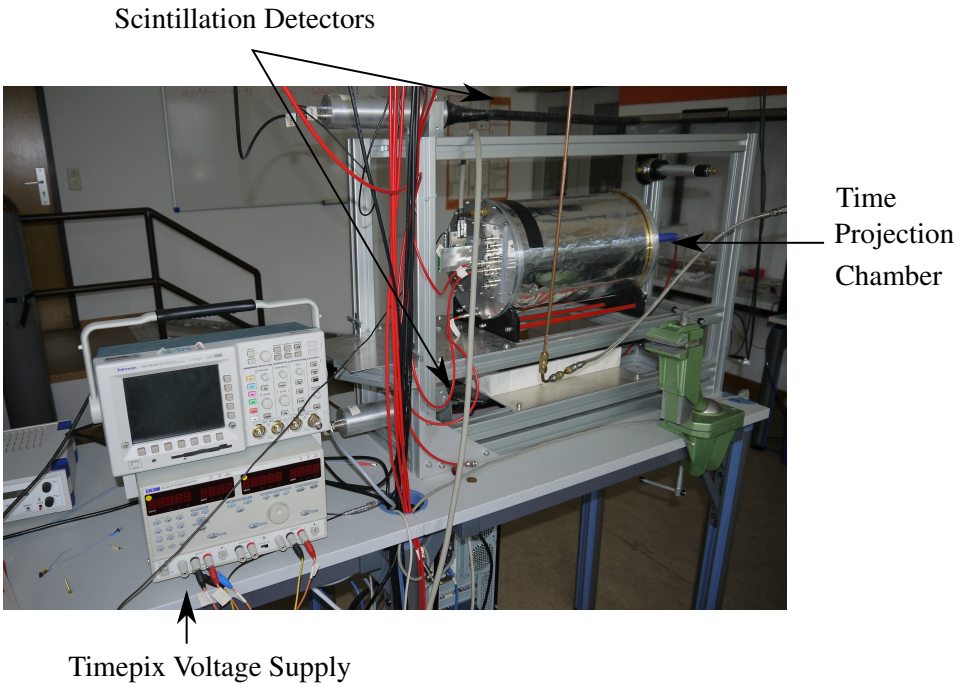

Figure 3.6: Setup of the experiment

serves as the trigger for the readout. A lead block above the second scintillator reduces the background from lower energetic particles.
A single InGrid was implemented into the center of the readout plane while the anode plane was positioned at the same height as the metal grid. Thus, the potential of both must be the equivalent to achieve a homogeneous electric field inside the TPC. The Timepix chip is connected to the MUROS2-readout system (Medipix re- Usable Readout System). The MUROS2 connects the Timepix with a PC and controls the chip functionalities. In addition, the MUROS2 generates the clock which is fed into the Timepix. The supply voltages for the Timepix can also be generated by the MUROS2 but a more stable voltage source was used in the experiment.
Pixelman is the name of the PC software which one controls the MUROS2 with and hence the behavior of the Timepix. The equalization of the pixel thresholds, the charge calibration of the chip and the definition of the operation mode are some of the many important features of Pixelman. The MUROS2 is able to read out eight Timepix chips. As the development of the InGrid was on a single chip level during the thesis and the amount of usable chips was low, a single InGrid was implemented in the TPC as the readout plane. Figure 3.7 shows pictures of the readout plane of the TPC. The metal grid is connected to the high voltage via the orange cable and a 10 MΩ resistor as protection. The gap between the chip and the anode plane generates field distortions and should be as small as possible. The connection of the voltage supply for the InGrid and the bump bonds from the chip to the carrier PCB enlarge the required gap.
During the measurements two gas mixtures and varying grid voltages were used. Table 3.2 shows the different working points of the TPC during the experiments. A drift field of 500 V cm^{-1} was desired due to a simplified comparison with previous GEM and Timepix measurement. The small voltage of the metal grid and the anode do not allow such a field in the field cage. The drift field was held at the highest possible value for each run.

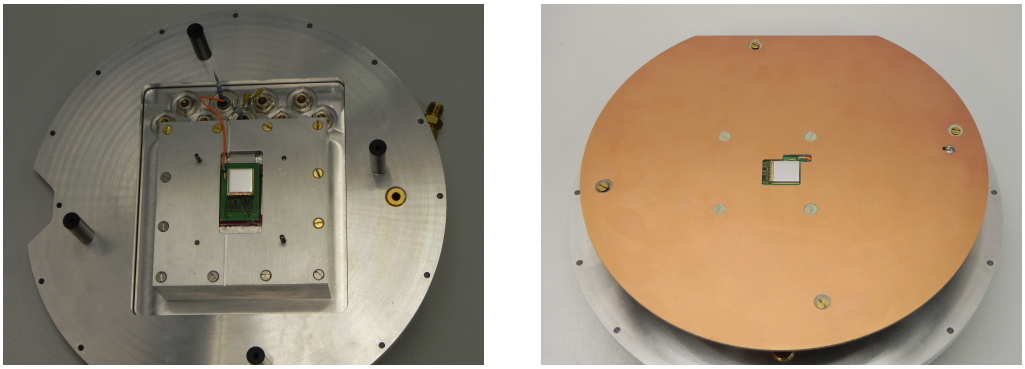

(a) (b)

Figure 3.7: Interior view of the readout end cap a) without and b) with anode plate.

gas mixture	grid voltage	drift field
He/CO_2	490 V	423 V cm^{-1}
Ar/CO_2	370 V	313 V cm^{-1}
Ar/CO_2	380 V	324 V cm^{-1}
Ar/CO_2	390 V	335 V cm^{-1}
Ar/CO_2	400 V	346 V cm^{-1}

Table 3.2: Working parameters of the TPC during the measurements.

Chapter 4

Analysis Framework

In modern detector research the performance of a future detector is studied by building small scale prototypes and through simulations. To compare results of different working groups or simulation and measurement a common software package is beneficial. For the ILC project a software package is under development, which shall be used in simulation, reconstruction and analysis.

4.1 Linear Collider Input Output (LCIO)

Linear Collider Input Output (LCIO) is a framework used in the ILC collaboration for detector development. It defines data classes, a file format and a user interface. In addition, an implementation exist in C++ and Java to facilitate usage for developers.
LCIO defines several data classes and so-called container classes. The data classes are used to save the measured and reconstructed data. Objects of the data classes are placed inside collections, which are the container classes of LCIO. For the measurements of the Timepix chip inside a TPC, four different data collections are needed. The output of the Timepix chip is read into LCIO and is converted to TrackerRawData. This data class saves the information of the identification number of the chip and the pixel and the measured digital value. TrackerData provides more space for information about the pixels. The digital value of TrackerRawData now is changed into a time or charge information depending on the mode of the pixel. As one wants to create tracks, a class for possible track points exist and is called TrackerHit. It contains the access to all TrackerData objects, which are combined in a single hit as a large charge deposition causes the activation of more than one pixel. It also contains the position of the charge's center of gravity, the time and total charge of the hit.
The Track data class is the final one of the track reconstruction. The objects save all information about the parameterization of a reconstructed track and also provide access to the assigned hits. LCIO also defines the parameterization of the tracks which can be seen in figure 4.1.

4.2 Marlin and MarlinTPC

Modular Analysis and Reconstruction for the Linear Collider (Marlin) is a LCIO based software framework for simulation, reconstruction and analysis. It serves as the standardized C++ framework for the detector development of the ILC.
As the name implicates, Marlin is built up modularly. The modules are called Processors in Marlin and each Processor serves as one element in a chain to achieve a computational task. Therefore, the Processors can read in LCIO files, process the data and write out LCIO files. An XML steering file defines at runtime which Processors are used and the order of them. Settings of the processors and the names of the input and output collections are also set in the steering file. The data is processed in an event by event basis.

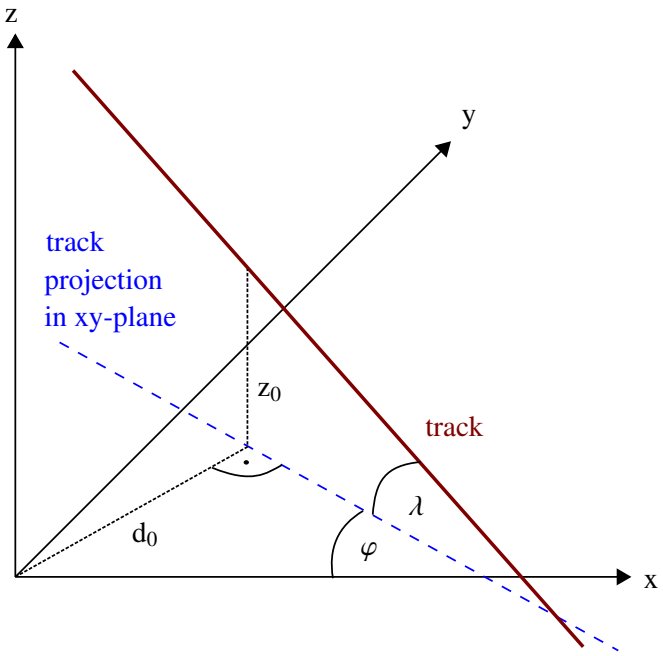

Figure 4.1: Sketch of the track parametrization in LCIO [35].

The modular structure of Marlin has the benefit of simplify testing, exchanging or the implementation of Processors. The steering files are altered easily and the rest of the chain remains.
MarlinTPC is a collection of Processors for the development of a TPC for the ILC. As many different readout technologies are studied, a common framework is advantageous to compare the results of the different working groups. A part of this work was the further development of existing and new Processors of MarlinTPC for the analysis of data obtained with an InGrid detector.

Chapter 5

Data Analysis and Results

This chapter is about the complete reconstruction of the track parameterization of cosmic muons and the analysis of the detector performance. First of all, a cluster analysis is done to define an appropriate track reconstruction chain. The charge calibration of the chip and the gas amplification measurements are shown. Then the reconstruction of the tracks is performed and the cuts applied on the data are presented, which are essential to suppress background events, noise and deficits in the track reconstruction. At the end, the analysis of the transverse and longitudinal spatial resolution of the TPC with InGrids is discussed. The proof of field inhomogeneities due to the gap between the grid and the anode plate will be shown and the influence on the measured date is demonstrated.

5.1 First Measurements

As the TPC had already been used with a GEM and Timepix readout, most of the parts were reused in the setup with the InGrid and only a few parts had to be modified. A new inset for the chip carrier had to be milled to create space for the high voltage connection of the grid. Also, the anode plane was newly constructed to fit next to the Grid. After the modifications, the first measurements were already performed. Figure 5.1 shows four typical events observed with the setup. The x-coordinate reflects the route between the two trigger scintillators. The lines are the reconstructed tracks taken from the reconstruction analysis described in chapter 5.4.
The InGrid used initially was destroyed by the first observed discharge. Its SiProt layer was only 2 µm thick. The InGrid, which the presented data was measured with, has a SiProt layer of 4 µm and proved to resist a few discharges. It was used constantly for around three months and is still working today. This shows that for future experiments, the SiProt layer of InGrids should have at least this thickness. A thicker layer has an even higher resistance towards discharges but has also some disadvantages. The charge of the avalanche accumulates on the surface and needs time to pass the layer. If the layer is too thick, the charge cannot be completely depleted between two events and the amplification field decreases. Thus, the gas gain is reduced. In a high frequency experiment as the ILC, the varying gas gain reduces the resolution of an energy loss measurement and even the efficiency.

5.2 Charge Spread of an Avalanche

The advantage of the Micromegas compared to GEMs is the short distance between the grid and the charge collecting anode. The electron diffusion in the Micromegas structure is suppressed and the amplification avalanche is rather thin. Therefore, the cluster size, created by a drifting electron on the chip, is of great interest. The measurements in Ar:CO_2 with the highest grid voltage show that most of the primary electron cause the activation of only a single pixel. In 10 % of the clusters, two neighboring pixels detect an induced current which reaches the threshold of the discriminator and activates the pixel.

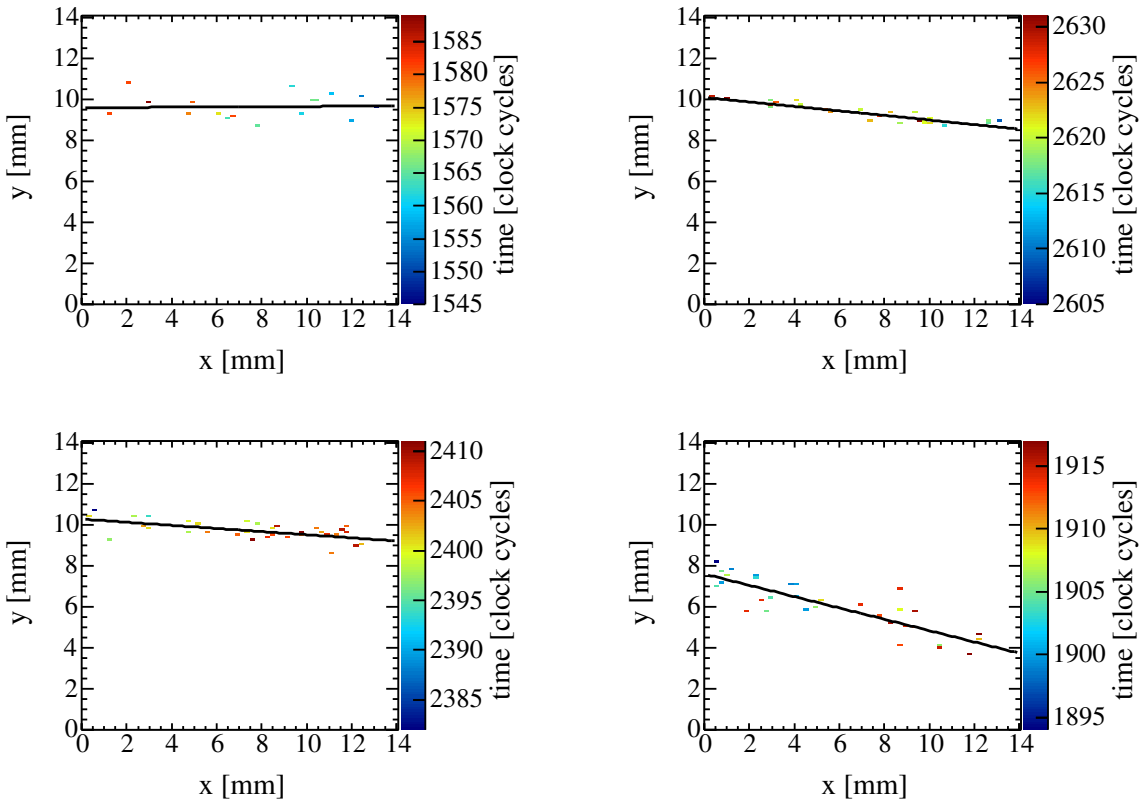

Figure 5.1: Four typical examples for tracks inside the experimental setup. The chip plane is represented by the *xy*-plane in the reconstruction while the abscissa reflects the way between the scintillators. The binning is reduced by a factor of four in both dimensions to enhance the visibility of the detected hits.

Now the question arises, whether pixels with neighbors do see a single thick or two thin electron avalanches. In the case where one drifting electron is responsible for the signal, two effects can cause the second pixel to measure charge. The first is a charge sharing effects as it is observed with GEMs. The avalanche of electrons becomes too wide and is observed by two pixels. The second possibility is crosstalk between the electronics of both pixel, which is enhanced if the gas amplification and the signal is large. One is currently unable to distinguish between the two effects. One has to inject a defined charge either in the bump pads or in the test input of the pixel and read out the surrounding ones. The bump pads cannot be easily connected through the holes of the grid and the software does not allow us to inject a test pulse in one pixel and read out others. A new readout is currently under development which will offer the possibility to measure the crosstalk. As the effects are not distinguishable at the moment, both will be addressed as charge sharing in the rest of the thesis. Fortunately, both effects result in a large charge deposition in one pixel and only a small charge measurement in the neighboring pixel. As the hole of the grid is centered above one pixel, a neighboring pixel would only measure a small induced current compared to the one centered. Two analyses are possible to explore the effect in detail. The first one is a measurement of the arrival times for both pixels. The difference of both arrival times should be zero if a single avalanche causes the activation of both pixel. Due to the timewalk effect, the expectation changes. The timewalk is an effect of a simple discriminator. Smaller signals reach the discriminator threshold later although the rise time of a larger signal is the same. Figure 5.27b shows a

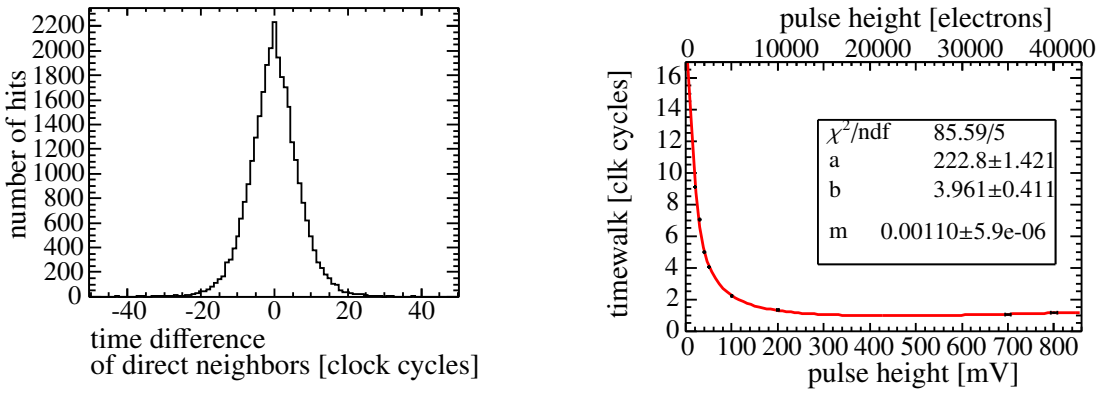

(a) (b)

Figure 5.2: a) Histogram of the time difference of two neighboring pixel. b) Calibration of the timewalk effect.

sketch of the timewalk. As one signal is considerably larger than the other, one expects a maximum in the difference spectrum inconsistent with zero but in the order of the timewalk effect.

The figure 5.2a shows the time difference of neighboring pixel. The difference is caused by two phenomena. On the one hand, two ionization electrons diffuse in the drift region and on the other hand, the timewalk of the discriminator. During the calibration of the chip the timewalk is also measured. One injects voltage pulses into the Timepix to put a well-defined amount of charge in each pixel. The time between the shutter start and the pulse injection is well-defined. One gains a Gaussian distribution of the ToA values of all pixels. The mean is than plotted against the voltage. To reduce statistical fluctuations an average of five measurements is calculated for each pulse height. Figure 5.2b shows the timewalk calibration. The fitted function is empirically determined and is described by:

$$f(x) = \frac{a}{Q+b} + mQ \tag{5.1}$$

with a, b and m fit parameters and Q the injected charge. The figure 5.2b shows this calibration and the curve converges to a fixed value. The distribution rises again for even larger voltage pulses. The working point of the preamplifier gets out of the linear behavior but the gas gain with InGrids will not reach these high values.

The gas gain during the measurements was between 1000 – 2000 (see chapter 5.6) which is at the beginning of the calibration curve. If a large electron avalanche causes the activation of both pixels, one would observe the timewalk effect due to the difference in the induced currents. According to the calibration one expects a time difference of around 6-10 clock cycles. As seen in figure 5.2a, the time difference of neighboring pixels has only a distinct maximum at zero and a Gaussian distribution. The diffusion alone explains this behavior and the timewalk effect does not dominate as one would expect for charge sharing.

The second option is the usage of the charge measurement of the pixels. The first observable is the difference of both charge values. As already mentioned, one expects one large and a second small signal if a single avalanche activated both pixels. Figure 5.3b shows the distribution of the measured charge difference for neighboring pixels. The distribution has its maximum at zero and a Gaussian shape. One cannot see an indication for a large amount of high charge differences. The second analysis of the measured charge is the investigation of the charge spectra of pixels with and without an activated neighbor. One expects to see an increase of low charge measurements in the charge spectrum of the

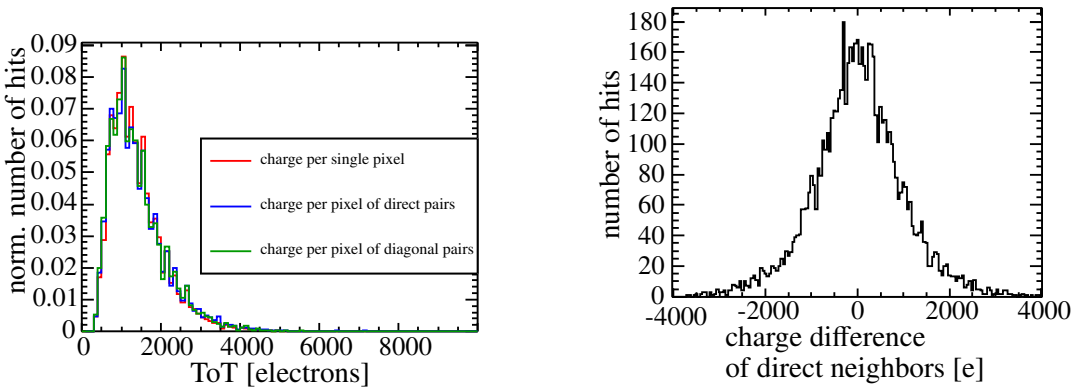

(a) (b)

Figure 5.3: a) Charge spectrum of single pixel (red), pixel with an activated neighbor at a side (blue) and at an edge (green). b) Difference of the charge measured of neighboring pixels.

pixel with activated neighboring pixels. In figure 5.3a one sees the charge spectra of pixel which have no activated neighbor (red), which have a neighbor at one of the four sides (blue) and which have a diagonal neighbor (green). One can clearly see that the spectra overlap nearly perfectly. The three spectra can be described by a Pólya-distribution and no shoulder is visible for low charge values. This is another indication of the fact that each activated pixel has detected a primary electron.
Both measurements and the tree analyses indicate that the effect of charge sharing is negligible with the gas gains used. This has two impacts on the measurements and reconstruction. In GEM setups, it is possible to run the chip in a checkerboard pattern of ToT and ToA mode pixels. As the cluster size is large enough one always gets time and charge information of one cluster. This can not be done with the InGrid. Therefore, the whole chip must be set in a single measurement mode. For the TPC it is necessary to have time information to reconstruct the third dimension of the track. The ToA mode is used in all measurements campaigns which were done in the context of track reconstruction and spatial resolution measurements. The ToT mode is only used in special cases in which one wants to study the gas gain. This deficit compared to a GEM setup cannot be compensated with the current setup. As already stated, the use of the future Timepix3 chip will solve the problem as each pixel is able to measure ToT and ToA at the same time.
On the other hand, the activation of single pixels gives a great benefit in the reconstruction of hits on the chip. One does not need a to use a complex cluster algorithm to identify clusters or separate overlapping clusters. One can use the simple fact that every activated pixel marks an incoming electron from the drift region.

5.3 Drift Velocity

A track reconstruction in a TPC needs the value of the drift velocity of the electrons. One can simulate the drift velocity with the program Magboltz [36]. Running parameters of the TPC, e.g. the gas temperature and the gas pressure have a strong influence on the drift velocity. During the experiments, one tried to stabilize the parameters as well as possible. The temperature was controlled with an air conditioner, which has a temperature stability of around 1K. The prototype TPC has no temperature detector inside the drift region and one can only measure the temperature of the room. The gas pressure is controlled by the gas system whose stability is of around 10 Pa. To reduce the decontamination of the

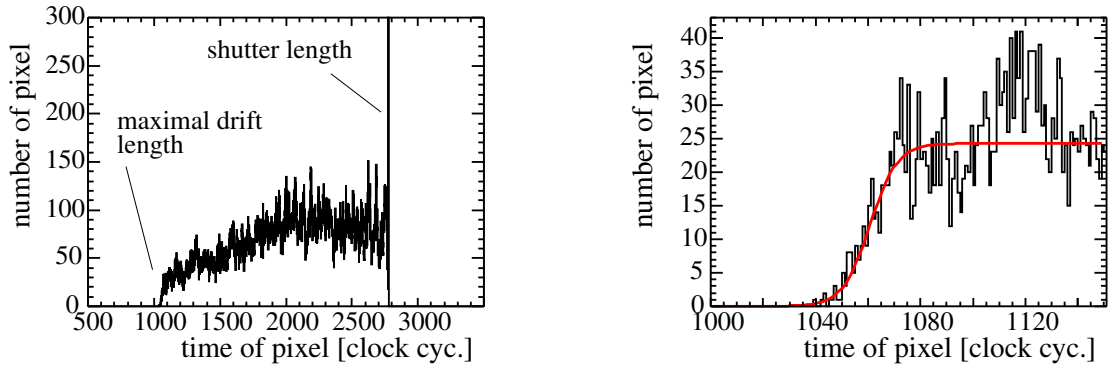

(a) (b)

Figure 5.4: a) Histogram of all ADC values from activated pixels. b) Zoom into the rise of the distribution and sigmoid function fit to get the drift velocity of electrons

gas with oxygen, one uses a low overpressure. The prototype TPC is not stable enough to withstand an overpressure of more than around 40 hPa. Thus the pressure was set to 20 hPa over standard states. Unfortunately, large external pressure variation caused the gas system to react to maintain an overpressure. That makes the simulation rather difficult as not all parameters are perfectly known or vary with time. It is better to measure the drift velocity of the electrons for each run than to use the simulated results. This is done by studying the spectrum of the measured time values of all pixels. Figure 5.4a shows this spectrum for one run in Ar:CO_2. One can see two distinct points of interest. The first is the cut off at the end of the histogram. This represents the anode plane of the TPC. If an electron hits the pixel right after the start of the trigger, the pixel in ToA mode counts as long as possible (the complete shutter length). The rise of the distribution at the anode plane is due to electrons which measured an induced current just before the shutter signal. The signal is still above the threshold when the trigger finally arrives. So one folds pixel with a slightly larger time measurement into the bin of the anode plane. The other effect in the distribution is the rise at the beginning. This comes from other side of the chamber, the cathode plate. The cut off is smeared out by the longitudinal diffusion of the drifting electrons and the timewalk. To define a reproducible starting point of the distribution, a sigmoid function is fitted to the rising edge. The used function is the logistic function as it fits the data well. The logistic function is defined as

$$f(x) = \frac{a}{1 - \exp\left(-b(t - \mu)\right)} \tag{5.2}$$

with a being the height, b the width and μ the turning point. The parameter μ is used to identify the cathode plane in the distribution. Figure 5.4b shows the determination for one run. With the information of the clock frequency ν, the maximal length of the drift region l and the difference between start and end point of the clock spectrum n one can calculate the drift velocity of the electrons v.

$$v = \frac{l}{n \cdot \nu} \tag{5.3}$$

The table 5.1 shows the measured and simulated results for the drift velocities. One can see that they deviate on a 4 % level. The differences can be explained with gas impurities, gas pressure and temperature. The temperature is the most probable reason as the resistor chain of the field cage can heat up the

gas mixture and grid voltage	mean of the measured drift velocities	simulated drift velocity
He/CO_2 490 V	$(0,832 \pm 0,0029)$ mm µs^{-1}	$0,808$ mm µs^{-1} $\pm$ 0.17 %
Ar/CO_2 370 V	$(0,7321 \pm 0,0019)$ mm µs^{-1}	$0,719$ mm µs^{-1} $\pm$ 0.15 %
Ar/CO_2 380 V	$(0,7576 \pm 0,0019)$ mm µs^{-1}	$0,744$ mm µs^{-1} $\pm$ 0.07 %
Ar/CO_2 390 V	$(0,7874 \pm 0,0047)$ mm µs^{-1}	$0,773$ mm µs^{-1} $\pm$ 0.07 %
Ar/CO_2 400 V	$(0,8303 \pm 0,0062)$ mm µs^{-1}	$0,8201$ mm µs^{-1} $\pm$ 0.08 %

Table 5.1: Measured and simulated drift velocities for all five measurement campaigns.

drift gas and one only measures the temperature of the room.

5.4 Reconstruction Chain

With the information gained in the previous chapters, one can define the complete reconstruction chain for an InGrid detector. This includes the read in of the data, the reconstruction of the track parameters and the analysis of the tracks.

Read in of Data and Zero Suppression

The first step is to read in the data from the Pixelman software of the Timepix chip. Pixelman is able to write in different formats from which an ASCII matrix of $256 \times 256 = 65536$ numbers was chosen. Each event is stored as a file by Pixelman. Then the ASCII files are read in and are converted to the LCIO data format. For each file an event is created in LCIO. The occupancy of the chip is very low in the InGrid setup. Thus, a zero suppression of the data is performed to reduce the data size on the disk. The identification number of the pixel is stored to maintain the information of the hit's position.

Position Reconstruction of the Hits

Until now the information about each hit is the pixel identification number and the counter value. So, one must calculate the true electron position. As the pixel pitch is well-known, the conversion of the pixel ID to the xy-position inside the TPC is rather simple. LCIO uses the software package GEAR (Geometry API for Reconstruction) for the definition of the detector geometry. The geometry is specified in a XML-configuration file which is inserted into the reconstruction software. The position and size of each detector in a TPC is described in the configuration file. For the setup of a single Timepix chip one typically puts the origin of the coordinate system at the center of the bottom left pixel and the detector plane lies in the xy-plane.
One also has to provide the software with a mode map which defines the measurement mode of each pixel. The mode map is read in during the initialization of the processors and is then accessible for each processor thereafter. The software is than able to convert the detected ADC values to charge or time information dependent on the pixel mode.
To reconstruct the z-position of the hit, one has to know the shutter length t_{shutter}, the drift velocity v, the readout frequency ν and the shutter delay t_{delay}. Of course, the pixel has to run in ToA mode and measures the counter N. The shutter delay describes the time between the pulse generation in the trigger scintillators and the arrival of the shutter signal in the chip. Both signals can be inserted into an oscilloscope and one can read off the time difference. Due to the slow trigger generator, the shutter signal is delayed by $t_{\text{delay}} = 0.7\,\mu\text{s}$. Thus, the detector can not observe electrons right above the InGrid as they arrive before the trigger signal. The region depends on the drift velocity and has a height of

around 5 mm.
The equation to calculate the z-position is as follows

$$z = \left(t_{\text{shutter}} - \frac{N}{\nu}\right) \cdot v + t_{\text{delay}} v = \left(\left(t_{\text{shutter}} + t_{\text{delay}}\right) - \frac{N}{\nu}\right) \cdot v \tag{5.4}$$

Track Identification

After the reconstruction of the electron positions, the tracks in the events must be identified. There are several possible algorithms, but the Hough-transformation is the only implemented algorithm in MarlinTPC so far. With a Hough-transformation one is able to assign all points on a straight line to the corresponding line. If the electrons are aligned along a track with the positions (x_i,y_i) one writes the linear equation as

$$y_i = a x_i + b \tag{5.5}$$

$$b = -a x_i + y_i \tag{5.6}$$

with a the slope of the track and b the intercept. Formula (5.6) shows that each point (x_i,y_i) in the image space can be transformed to a straight line in the so-called parameter space (a,b) with the slope x_i and the intercept y_i.
All points, belonging to a single track, create a line in parameter space, which intercept each other at a single point. The interception point represents the parameters of the track in the image space. As the electrons do not lie right on the track but are Gaussian distributed due to diffusion, the lines in the parameter space to not intercept at a single point. Nevertheless, the lines meet each other close enough to use a binned histogram. The binning of the histogram can be adapted to the diffusion of the electrons. One now has gained a first approximation of the track parameters. The binning reduces the resolution of the parameter and a linear regression will be later used to find the precise parameter values.
To assign the detected hits to the corresponding track found by the Hough-transformation, a tube with variable radius was used. The radius was adapted to the diffusion expected for the electrons. Thus the radius is dependent on the running parameters of the TPC and the z-position of the hit. All electrons, lying in the tube around a track, are allocated to the track.
A threshold for the number of electrons per track can also be applied in the processor. In the measurements the threshold was set to six. Lower thresholds cause the adjacent linear regression to suffer from a low number of degrees of freedom.

Linear Regression

The track parameters of the Hough-transformations have a large error because of binning effects of the histogram. The tracks of the muons are straight lines because no magnetic field was applied during the measurements. Hence, a linear regression is the natural choice for calculating the parameters of the track.
All tracks are aligned along the x-axis of the chip because of the trigger geometry. Therefore, the track is parametrized in the following form:

$$y = a \cdot x + b \tag{5.7}$$

$$z = c \cdot x + d \tag{5.8}$$

The equation of the linear regression for the slope a and interception b are

$$a = \frac{n\Sigma_i x_i y_i - \Sigma_i x_i \Sigma_i y_i}{n\Sigma_i x_i^2 - (\Sigma_i x_i)^2} \tag{5.9}$$

$$b = \frac{\Sigma_i x_i^2 \Sigma_i yi - \Sigma_i x_i \Sigma_i x_i y_i}{n\Sigma_i x_i^2 - (\Sigma_i x_i)^2} \tag{5.10}$$

and the parameters c and d equivalent.
LCIO does not use the slopes and intercepts to define the tracks but the parameters as already shown in figure 4.1. So, one has to transform the calculated values to the parameters of LCIO. The inverse of the transformation will be presented. The transformation was already implemented in LCIO, but the inverse transformation had to be calculated to be able to draw tracks in event displays.
The parameterization of the xy-plane can be achieved with geometrical considerations.

$$y = \tan(\varphi)x + \cos(\varphi)d_0 \tag{5.11}$$

For the zx-plane one must calculate the line integral l_{xy} with the origin at the point of closest approach $\vec{d_0}$.

$$l_{\mathrm{xy}} = \int_C y(x)\mathrm{d}s = \int_a^b \sqrt{1 + (y'(x))^2}\mathrm{d}x \tag{5.12}$$

$$= \int_{-d_0 \sin\varphi}^{x} \sqrt{1 + \tan^2(\varphi)}\mathrm{d}x = \sqrt{1 + \tan^2(\varphi)}(x + d_0 \sin\varphi) \tag{5.13}$$

As λ is defined to the projection of the track on the xy-plane, one can write the parametrization in the z-direction as

$$z = z_0 + l_{\mathrm{xy}} \tan\lambda = z_0 + \tan\lambda \sqrt{1 + \tan^2(\varphi)} \cdot (d_0 \sin\varphi) + \tan\lambda \sqrt{1 + \tan^2}(\varphi)x \tag{5.14}$$

$$\Rightarrow x = -\frac{z_0}{\tan\lambda \sqrt{1 + \tan^2(\varphi)}} - d_0 \sin\varphi + \frac{1}{t \tan\lambda \sqrt{1 + \tan^2(\varphi)}}z \tag{5.15}$$

We can see that the parameterization of MarlinTPC fully describes the tracks inside the TPC. If the tracks are curved by a magnetic field, a helix fit is also implemented in LCIO. For the paramerization of a helix, one additionally needs the curvature Ω. As the helix fit is only used in a single diagnostic analysis, it is not further explained.

Analysis Processors

After the track parameters are successfully reconstructed, one can use several different analysis processors in Marlin. Besides defining cuts on the data, one can create many different statistical distributions of the track and hit parameters.

5.5 Charge Calibration of the Timepix

To determine the gas gain of the InGrid, one first has to calibrate the chip. As for the calibration of the timewalk, voltage pulses are injected into the test input of the Timepix but the pixels are now in ToT mode. The test capacitance is a high precision capacitor with a capacitance of $C = 8\,\mathrm{fF}$. One can

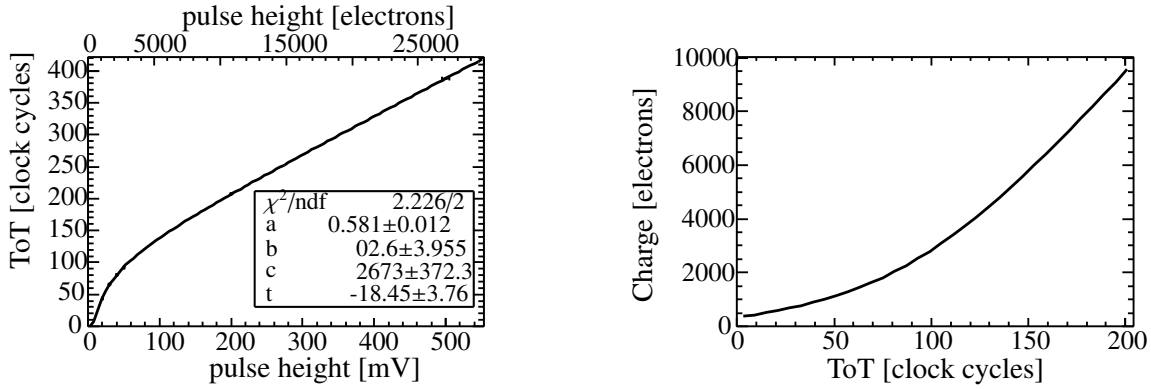

Figure 5.5: Charge calibration curves for the Timepix chip determined by injecting test pulses into each pixel. a) Calibration curve with the pulse height as the abscissa. The fit function is described in the equation 5.17. b) Relation between measured ToT values and induced electrons.

calculate the induced charge from the pulse high U.

$$Q[electrons] = \frac{CU}{e} \approx 50 \cdot \frac{U}{\mathrm{mV}} \tag{5.16}$$

For each voltage pulse the distribution of the ToT values of the chip are created. The mean is then plotted against the pulse height. So, by injecting pulses with different sizes, the calibration curve can be plotted. To lower the influence of statistical fluctuation, the procedure is performed five times for each pulse height and the average is taken. Figure 5.5 shows the charge calibration curves for the Timepix. The left plot is the charge calibration, which is the result of the calibration measurements. The fit function is empirically determined and has the following form:

$$ToT = a \cdot U + b - \frac{c}{U - t} \tag{5.17}$$

The right plot emphasizes the relation between the measured ToT values and the induced electrons. In addition, one can see the threshold of the detector. The intercept point of the curve and the ordinate is the threshold. The threshold used in the measurements is determined as 330 electrons.
The linear behavior in the dependance of ToT values to electrons is reached for ToT> 110 but one will see in chapter 5.6, that the gas gain of the InGrid is in the range of low charge.

5.6 Gas Amplification

With the charge calibration performed, one can determine the gas amplification of the InGrid. Therefore, single measurement campaigns are performed with the Timepix in ToT mode. As each activated pixel is regarded as a primary electron inside the TPC, one can just use the charge spectra of all pixels after a zero suppression.
This was performed for all five parameter configuration. Figures 5.6a and 5.7 show the different charge spectra. The spectra are Pólya-shaped distributions. Due to the non-linearity of charge calibration curve, the Pólya-distribution is modified and is not fitted to the data. The mean of the distribution is defined as the gas gain. In addition, it is shown in figure 5.6a that the higher the grid voltage, the more the

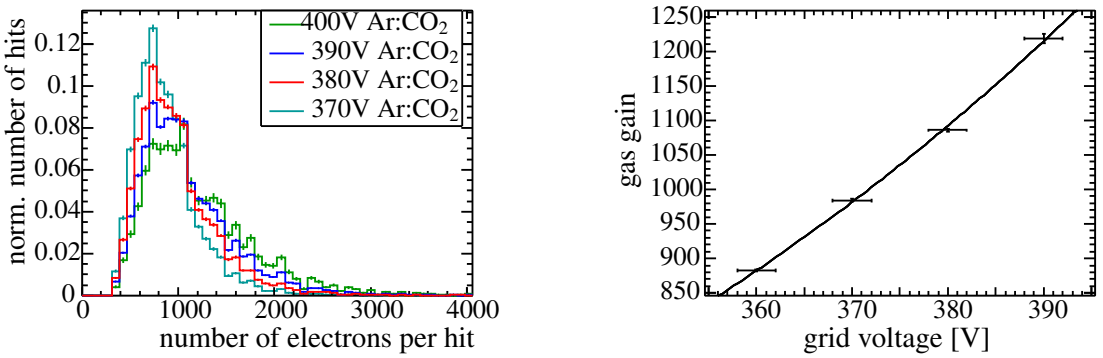

(a) (b)

Figure 5.6: a) Charge spectra of the argon campaigns for all hits on the chip. b) Gas gain of the InGrid for the four different grid voltages in Ar:CO_2. For a gaseous detector in the proportionality range, one would expect an exponential rise which can be seen in the data (exponential fit function).

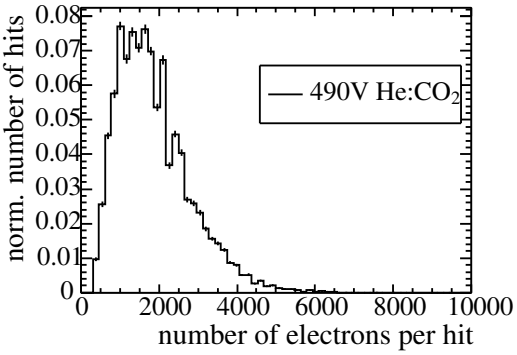

Figure 5.7: Charge spectrum of the helium campaign for all hits on the chip.

distribution is shifted to higher values. Of course this is expected behavior because a higher grid voltage leads to a higher electric field in the amplification region. This leads to a higher gas gain. The gas gain for the four campaigns with Ar:CO_2 as the gas mixture is presented in figure 5.6b. An exponential progress is expected for a gas detector performing in the proportionality region. The exponential fit function describes the data well and the highest gas gain achieved in Ar:CO_2 was 1218.4 ± 6.1 which is low. This shows that it is possible to run the detector well with low gas gains, but on the other hand the single electron efficiency might be relatively low. The electron efficiency should be as high as possible to reach the energy loss resolution desired for the ILC. The track resolution also suffers as it is strongly dependent on the number of reconstructed track points. The first employed InGrid was destroyed from the first discharge at a grid voltage of 510 V in He:CO_2 and some discharges were already observed with the second InGrid at 400 V in Ar:CO_2. Although the second InGrid has a thicker SiProt layer of 4 µm, the grid voltage was not increased to protect the chip from a possibly destructive discharge. Thus, the additional measurement campaign with He:CO_2 was executed instead. He:CO_2 has the advantage that higher electric fields are possible before discharges occur, but the number of electrons along the trajectory of the charged particle is much lower. Figure 5.6 shows that a higher gas gain was achieved compared to the argon measurements. The gas gain in helium was 1874.1 ± 4.5.

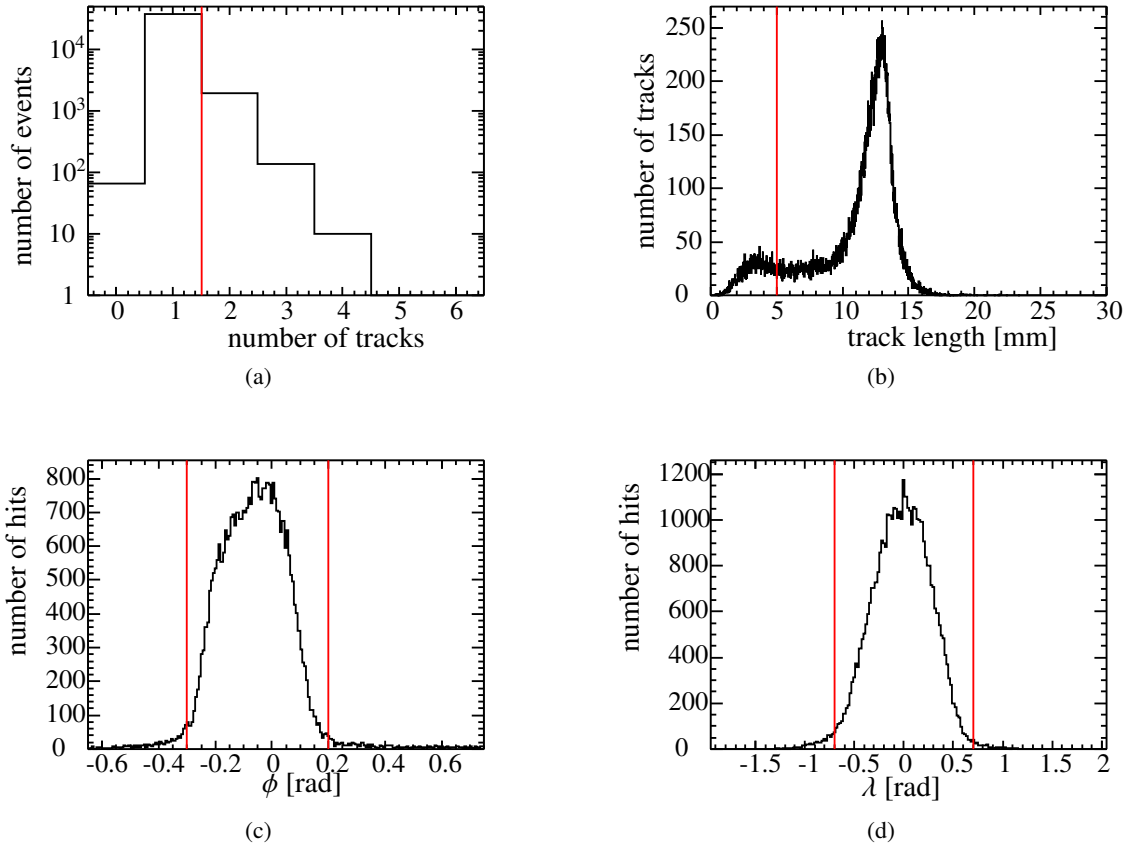

Figure 5.8: Histograms of several parameters of the reconstructed tracks without applied cuts on the data. The red lines symbolize the cut values which are used for further studies. a) Histogram of the number of tracks per event. b) Histogram of the measured track length. c) φ-distribution of the tracks. d) λ-distribution of the measured tracks (for the definition of φ and λ see figure 4.1).

5.7 Track Parameters and Cuts Applied

The purpose of this work was to measure the spatial resolution of an InGrid detector inside a TPC. Therefore, a number of cuts on the data had to be applied to reduce the influence of background events, delta electrons and noise. Many background events can be suppressed by considering the geometry of the trigger. One only wants to detect the cosmic rays which passed through both trigger scintillators of the detector. This diminishes the possible solid angle for the detected tracks. In the MarlinTPC framework this results in a limitation of the φ and λ angles (for the definition of the angles see figure 4.1). In addition, the active area of the InGrid is very small. If a track has a certain angle and only grazes the detector, the track reconstruction cannot be performed correctly as too few track points are visible. So, a track length of at least 5 mm is required. The track length is defined as the largest length between the projections of the measured hits on the reconstructed track. This is an underestimation of the track length as both endpoints are primary electrons. By using a statistical factor of $n/(n-1)$, with n being the number of detected electrons, a corrected track length can be calculated. Figure 5.8 shows the different distribution of the track parameters with the data cuts displayed as red lines.
In figure 5.8a one can see that multiple track events are excluded. Due to the reconstruction al-

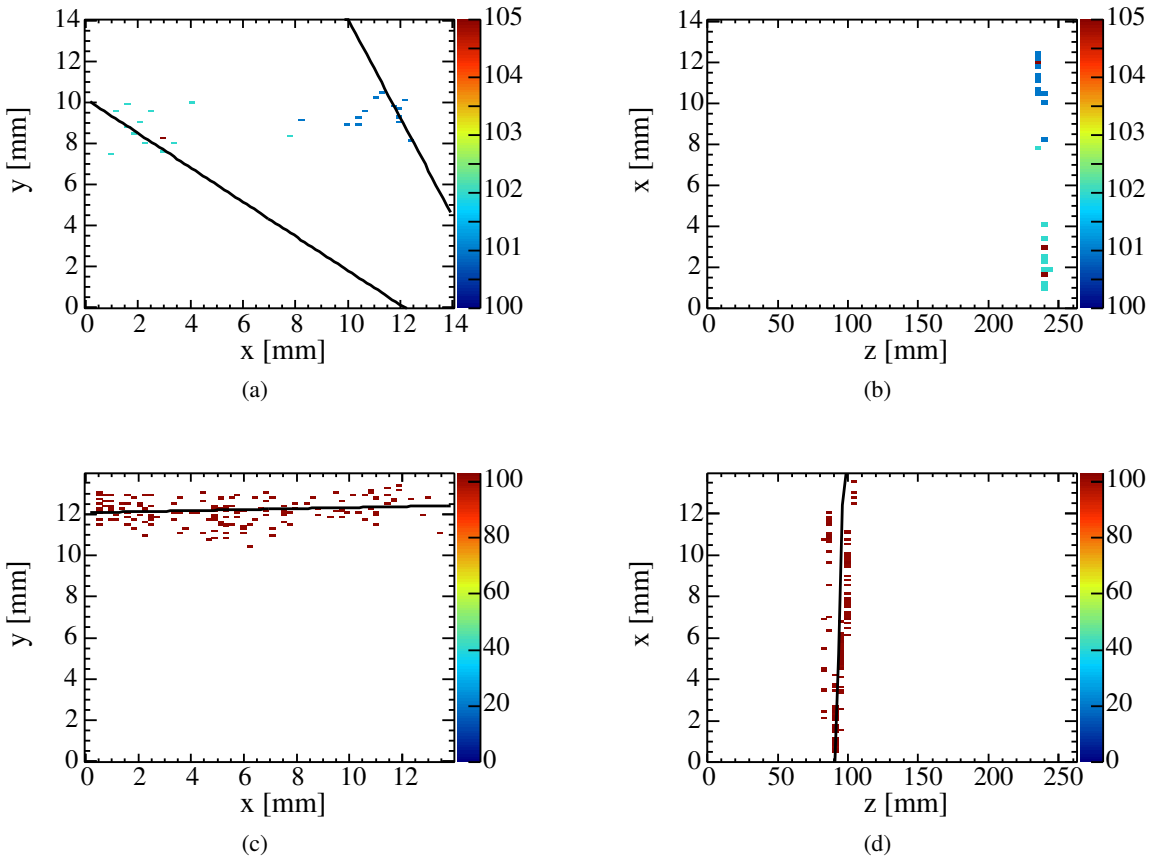

Figure 5.9: Two projections of two incorrectly reconstructed tracks. A single track reconstructed as two independent tracks in *xy*-plane a) and *zx*-plane b). Two tracks lying above each other in the *xy*-plane c) and *zx*-plane d). The color coding is used to identify the electrons corresponding to a single track.

gorithm, the cut is important to correct the data. As explained in chapter 5.4 the algorithm is a Hough-transformation in the detector plane. The transformation has two deficits. Fist, the third dimension of the tracks is not considered in the algorithm. Thus, two tracks lying upon each other in the *xy*-plane are reconstructed as one. Figures 5.9c and 5.9d demonstrate such an event in two projections of the TPC. The lines in the figures are the reconstructed tracks. One can clearly see two distinguishable tracks in the *zx*-plane but the reconstruction in the *xy*-plane can only identify a single track. To remove these events, a cut is implemented which is explained in chapter 5.8.
The second problem occurs if a single track consists of two distant electron groups. As the energy transfer is a statistical process with large fluctuations, this happens in few cases. The Hough-transformation searches for the interception points of the lines in the Hough space. In the current form the maximum is found with a binned histogram. In the case of the two distinct electron cluster, the binning seems to cause the identification of two tracks. In the future, a different algorithm for track finding has to be implemented to avoid such false reconstructions. Figures 5.9a and 5.9b show one of these events. The cut on the number of tracks removes these events.
All electrons lying in a tube around the track are allocated to the track. If two tracks are lying relatively close to each other, an electron of one track can be allocated to the wrong track. This greatly influences the linear regression. This is another reason for reducing the analysis to single track events.

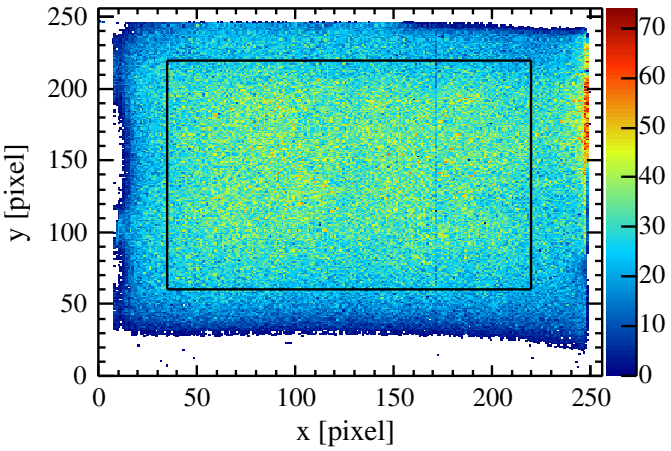

Figure 5.10: Occupancy plot of a measurement campaign without using cuts on the data. The lines demonstrate the area with the highest electron efficiency on the chip.

To remove delta electrons from the data, the number of electrons for a single track is restricted. Due to the low mass and energy of the delta electrons compared to muons, they lose all their kinetic energy on a short distance inside the TPC. So the total energy is transferred into the ionization of a large number of gas molecules. The cut was chosen by observing the tracks with a higher number of electrons until standard muon tracks are generated. The number for this setup was 200.
The final cut is necessary because of the small active area of the chip. If a track lies at the border of the chip, the electrons next to the chip are of course not detected. So the track reconstruction calculates a wrong track position and a narrower width of the hit distribution. This biases the spatial resolution towards lower values. Previously, one tried to avoid this by defining a new and smaller area within the active area of the chip. Then only tracks were used which do not have a single electron outside this new border. On the one hand, the cut removes too many tracks from the data sample and on the other hand, a biasing of the spatial resolution does still occur. The diffusion is a statistical process and tracks with a statistical low diffusion are preferred because of the cut. Thus, a new type of cut was implemented into MarlinTPC. The trigger geometry causes the tracks to have a preferred orientation along the x-axis of the chip. One now defines a vertical line on the left and on the right side of the chip. The restriction implemented is that the reconstructed track has to pass both lines. If one defines a large enough distance from the line's endpoint to the borders of the chip, one does not bias the results of spatial resolution. Figure 5.10 shows the occupancy of the chip for all runs of argon with a grid voltage of 400 V. The lines, which are drawn in the figure on the left and on the right side, show the cut as it is used in the thesis. The lines on the top and on the bottom will be discussed in chapter 5.9.

5.8 Noise Reduction

Noise is an important effect for an InGrid readout. If noise activates a pixel, one reconstruct an additional drifting electron. A more advanced track reconstruction algorithm should be able to identify these electrons as the z-position should be off track. If the noise hit is also on track, one cannot distinguish it from the correct primary electrons. Thus, the threshold of the discriminator is set to a high signal to noise ratio to reduce the number of noise hits considerably. Single noise hits change the solution of the linear regression, which results in outlier events in the resolution measurements. Hence, an

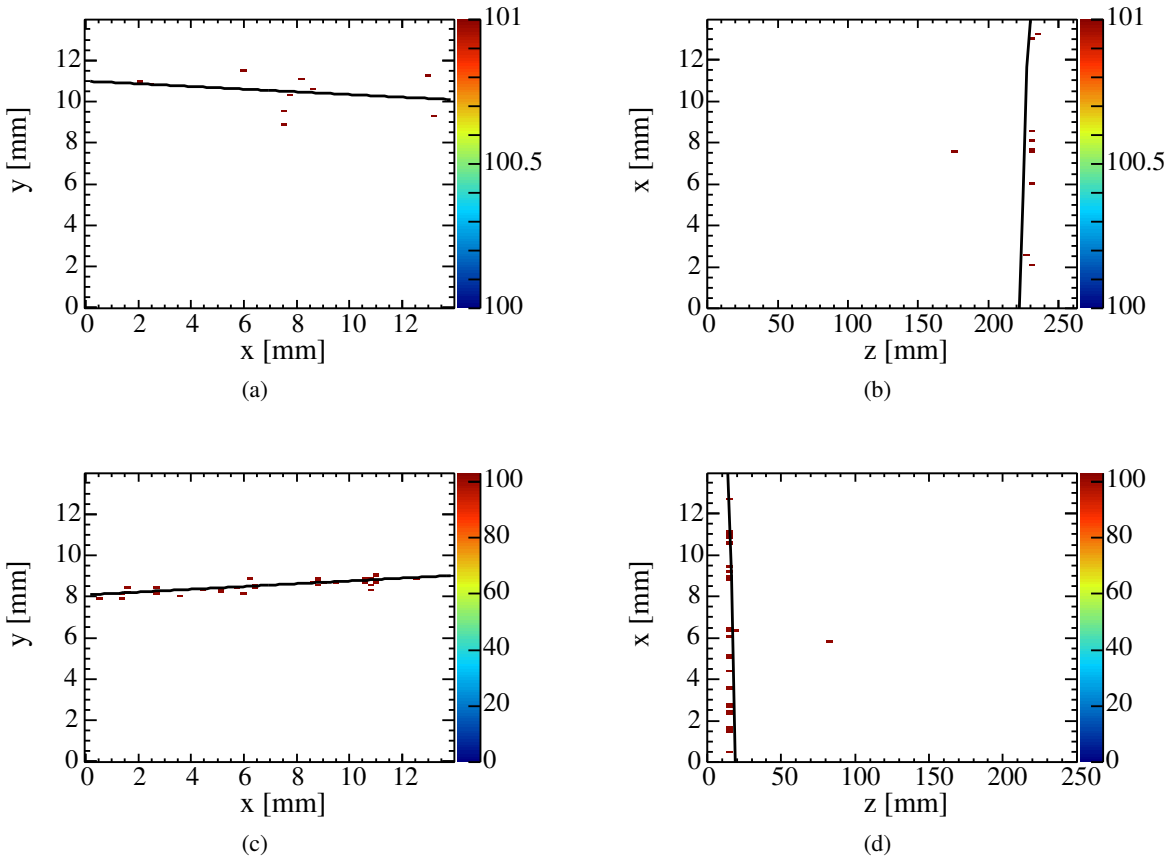

Figure 5.11: Example events of noise hits with reconstructed tracks. The noise hits greatly influence the track reconstruction and worsen spatial resolution. The color coding is used to identify the electrons corresponding to a single track.

identification and exclusion of the noise hits must be implemented. Figure 5.11 shows two identified noise hits in two projections of the chamber. Figures 5.11b and 5.11d clarifies the influence of noise hits on the reconstructed tracks in the z-dimension. As the noise hits are far away from the track, they greatly influence the reconstructed track.

The trigger geometry does not allow tracks with large φ or λ angles. This leads to tracks, which are nearly parallel to the x-axis. The mean and the median of the z- and y-positions of the hits are now good approximations of the position of the track. So one can easily use the root mean square (RMS) of the hit's z-position to identify the noise hits. If the RMS of the z-positions of hits passes a certain threshold, the event is taken out of the data sample. Figure 5.12b shows the RMS distribution of the z-position of track hits. The red line is again the cut which was applied in the final configuration of data analysis. The cut seems to be chosen arbitrary, but it was set such that large outliers in the spatial resolution distributions are eliminated. Figure A.3 in the appendix shows a scatter plot of the longitudinal spatial resolution of each track without the cut applied. One can identify a large number of outliers which can greatly influence the mean calculation of the spatial resolution. The cut removes most of the outlier events.

The cut on the RMS deletes a complete event from the analysis as one does not identify the actual noise hit, but only the existence of one. Another approach to find the noise hits is the usage of the

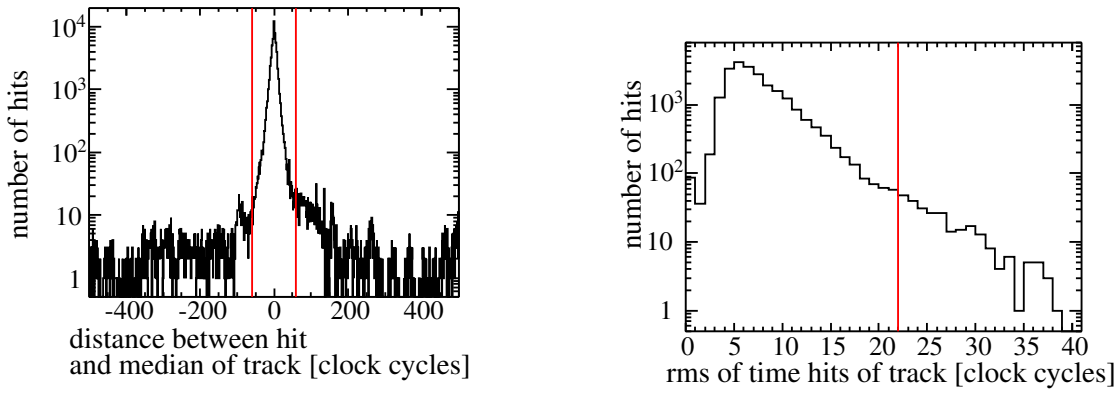

(a) (b)

Figure 5.12: a) The distribution of the difference between the median of the z-positions of the track hits and each hit's z-position. b) The distribution of the RMS of the track hit's z-positions. The red lines illustrate the chosen cuts to clean the data from noise hits.

median. The median of the z-position of the hits is more robust regarding single outliers compared to the mean. So one is able to calculate the distance between the median and the z-position of the hits. One gets a distribution as in figure 5.12a. The peak at the center of the distribution contains the hits which are correctly allocated to a track. The cuts were set at the position where the peak loses its original form. In addition, one can see that one has more hits with a positive value than a negative one. This fact means that more hits are delayed. The reason is attachment of electrons to components of the gas mixture. Naturally the reverse reaction is also possible where the electron is released from the oxygen. The released electrons arrives later and are reconstructed wrongly. As the reverse reaction is also statistically distributed in time and the electrons are indistinguishable from noise hits, one cannot calculate the original position and released electrons are counted as noise hits.

5.9 Field Distortions

One could already see in figure 5.10 that the chip is not occupied homogeneously over the whole area. At the sides of the chip one does not have any detected hits at all. On the one hand, this comes from the stabilization frame of the InGrid with a width of 500 µm. The frame covers around ten rows of pixel at the edge of the chip. At the top and the right side of the chip one can see the intersection of active pixel and the frame. But at the left and bottom side, the active area is further away from the chip borders. The occupancy also starts to get lower outside of the black frame in the figure. This originates from field distortions above the grid. Due to the gap between the amplification grid and the anode plane, one creates a distortion of the drift field. The field distortions at the left and bottom side are larger because of a larger gap. The wire for the voltage connection of the grid is positioned at the left side and requires a larger distance to the anode plate. Two different problems occur at the bottom of the chip. On the one hand, one has the gap towards the anode plane and on the other hand the wire bonds of the Timepix to the carrier PCB. They are on about ground potential and have nearly the same height as the grid. So, the bond wires on ground potential next to the high voltage of the grid enlarge the field distortions created by the gap in the anode plane. An ANSYS simulation is shown in the appendix in figure A.4. The simulation shows the electric field in the direction of the chip plane. Due to the gap, distortions of the design value of zero reach above $10\,\mathrm{V\,cm^{-1}}$ above the chip.

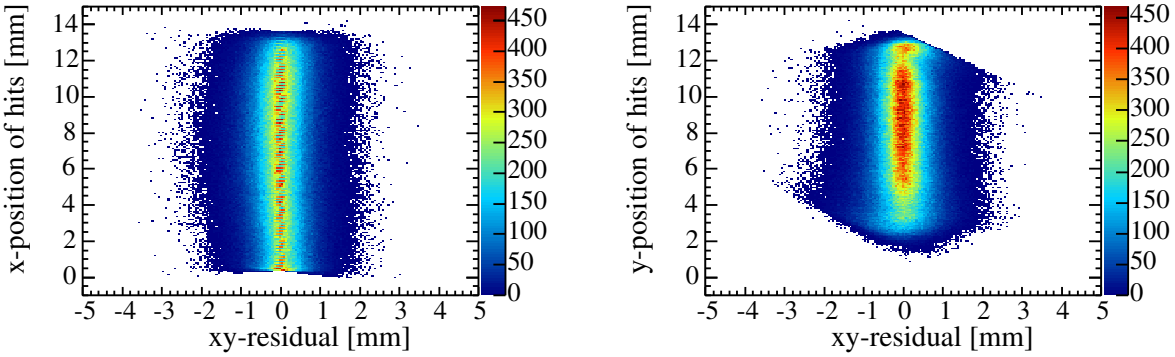

(a) (b)

Figure 5.13: The plots show histograms of the *xy*-residual of hits with respect to the hit's *x*-position a) and *y*-position b).

Several ideas are under development which will reduce the field distortions. The first improvement will be the usage of a Frisch grid. The zero grid of the original wire readout of the TPC is a Frisch grid. It decouples the drift field from the electric field between the Frisch grid and the InGrid. This will limit the range of the field distortion to the Frisch grid. If the distance between both grids is kept small, the influence of the distortion should be lowered. A larger influence would be achieved if the anode plate would be closer to the grid. Therefore, a new carrier PCB for the Timepix is already constructed, but could not be implemented yet. One of the advantages of the new carrier is that the connection of grid voltage lies at the rear side of the carrier and the large cable is not needed. A wire bond is enough to connect the grid with the PCB and consequently the voltage supply. In addition, the geometry was changed a little and one should be able to reduce the curvature of the wire bonds. This results in a reduction in the height and hence, field distortions. The last important change of the PCB is the connecter to the readout. In the present setup a ribbon cable is used, which also defines the chip's position in the detector. As the cable is flexible, the position of the chip can vary a bit. So, the cut-out in the anode plane had to be larger than the chip size to avoid the destruction of the grid during the installation of chip and anode plate. The new connecter is a plug connector which reduces the variations of the position. This allows us to create a new anode plate with smaller gap sizes.
In the future the Timepix3 will be used in the experiment. It has a large advantage as it can be used with so-called Through Silicon Via. This relatively new technology allows the user to connect the chip with the carrier PCB from the rear side of the chip. Wire bonds are therefore unnecessary in the setup.
As the field distortions are clearly visible in the measurements, one must study the influence on the data. In a first attempt, the residuals of the hits with respect to the reconstructed track were analyzed. The residuals of hits with respect to the *x*-and *y*-position of the hit are plotted in figure 5.13. One expects that the highest values are at zero and the plots show this behavior. The barbs in figure 5.13b come from the geometry of the trigger scintillators and the preferred direction of the tracks.
A closer look of the distribution can be achieved by separating the distribution in figure 5.13a into bins of the *x*-position. Then one calculates the mean and RMS of the *xy*-residuals in each bin. This was done in figure 5.14 for tracks with a short drift distance. A long drift distance disguises the behavior in the figure due to the large diffusion. The distribution of the means exhibits a curvature. This is not the expected behavior but it can also be explained by the field distortions. If the track is at the bottom of the chip, the field causes electrons to move downwards. This effect is stronger in the middle of chip

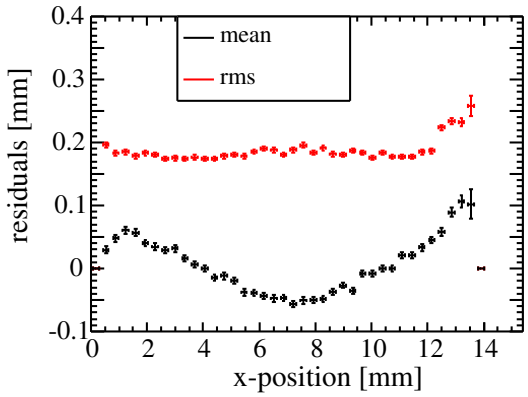

Figure 5.14: Mean and RMS for the *xy*-residuals of hits for different *x*-positions on the chip.

because the field distortions bend sideways at the sides of the chip. A curvature of the track is the result. The linear regression of the track suffers from the curvature and the RMS of the hit's residuals becomes larger.
The plot is useful when verifying if the tracks have a curvature, but one also wants to find the corrupted area on the chip. The tracks follow the x -dimension and the field distortion in this direction cannot cause a curvature. So, one just has to find the region in the *y*-dimension which causes the corruption of the data. Therefore, a diagnostic analysis is performed. Instead of using a linear regression of the track, one now takes a helix fit as if a magnetic field is applied. Of course, the distortions do not create a helix shaped trajectory of the track but a rather complicated behavior, but the chip size and the curvature are small enough that a helix is a good approximation for the curvature of the tracks. A helix fit is implemented in MarlinTPC, which simplifies the process. With the curvature of the track now acquired, one can now look at the dependency of the curvature of the track on the *y*-position of each hit. This was performed in figure 5.15a. The curvature is around zero for larger values of the *y*-position. For lower values the mean of the curvature moves to negative values. So, one found the area on the chip which is the least affected by the field distortions. This is displayed in figure 5.15b as a black frame in the occupancy histogram of the measurements with of Ar:CO_2 and a grid voltage of 400 V.
Now one verifies the result. Therefore, the same procedure is done as in figure 5.14 but this time one just uses tracks which lie inside the area of most homogenous drift field. The result is shown in figure 5.16. The expected mean of zero is fulfilled for all *x*-position of the chip. Also the RMS of the residuals is lower compared to the data of the larger area.

5.10 Number of Electrons per Track Length and Efficiency

To reach the desired resolution of the particle momentum in the ILD, one has to detect as many track points as possible in the TPC. The large number of track points in a TPC is the reason that one can reach a similar resolution as in the case with silicon based tracking detectors.
For all five measurements campaigns the number of electrons per track length was determined dependent on the *z*-position of the primary electron. The four different grid voltages in Ar:CO_2 are displayed in figure 5.17a and the helium run in figure 5.17b. All the distributions have the same characteristic behavior. At small drift distances the highest number of electrons are detected. With larger drift distances one starts to lose electrons along their path towards the detector. The reason is electron attachment to a

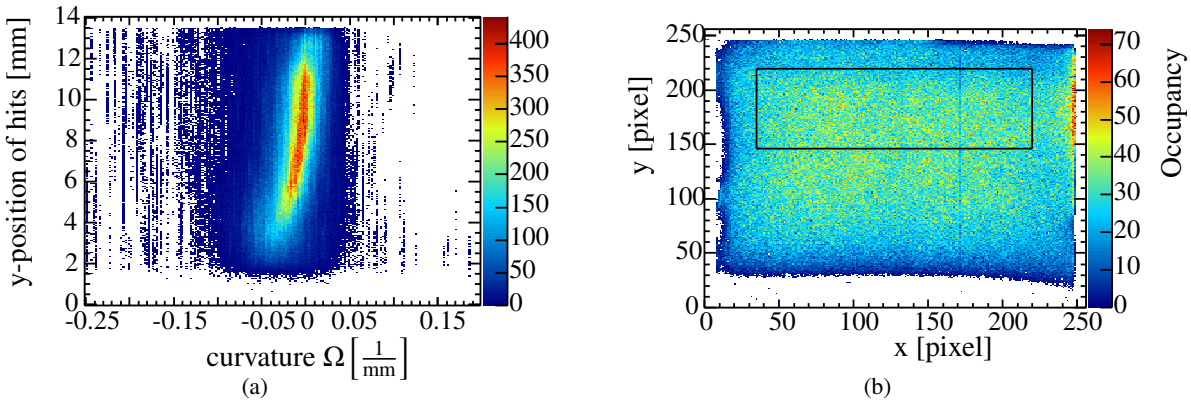

Figure 5.15: a) The histogram of the curvature of the track plotted against the each hit's y-position. b) The figure shows the occupancy of the chip and a black frame that marks the area which is influenced the least by the field distortions.

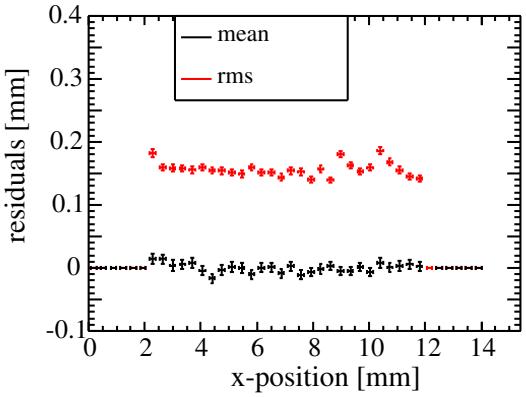

Figure 5.16: Mean and RMS for the xy-residuals of hits for different x-positions on the chip. The data consists of tracks inside the chip area which is influenced the least by the field distortions.

component of the gas mixture. Argon and helium does not form a stable anion in the TPC and the electron energy for a dissociative attachment to CO_2 is too large for the used drift field ($\sim 4\,\text{eV}$ and $\sim 8\,\text{eV}$ [37]). This was also verified with a simulation of the electron drift with the program Garfield++ [38]. The drift was simulated for ten thousand electrons and none of the electrons became attached to Ar:CO_2 or He:CO_2. So, the remaining possible gases are impurities due to leakages of the TPC and the gas system and impurities in the gas bottles from the supply company. Oxygen is the only gas component, that has a negative electron affinity and is in large amounts in the air, which is able to cause the electron attachment. The attachment with respect to the drift distance is an exponential function. The slope of the exponential function depends on the amount of oxygen inside the TPC. During the argon campaigns, the gas supply was changed. The campaign with the largest grid voltage was done with a premix bottle of the gas mixture. During the other three campaigns the gas system, built by a working group member, was used. One can see that the campaigns with the gas system have a smaller slope. The premix bottle was connected with a plastic pipe to the TPC, while the gas system uses gas tight copper pipes. As the slopes seemed rather large, the setup was changed in the helium campaign. The connection of a premix bottle and the TPC was held at minimum distance with a flexible metal tube and an oxygen absorber was

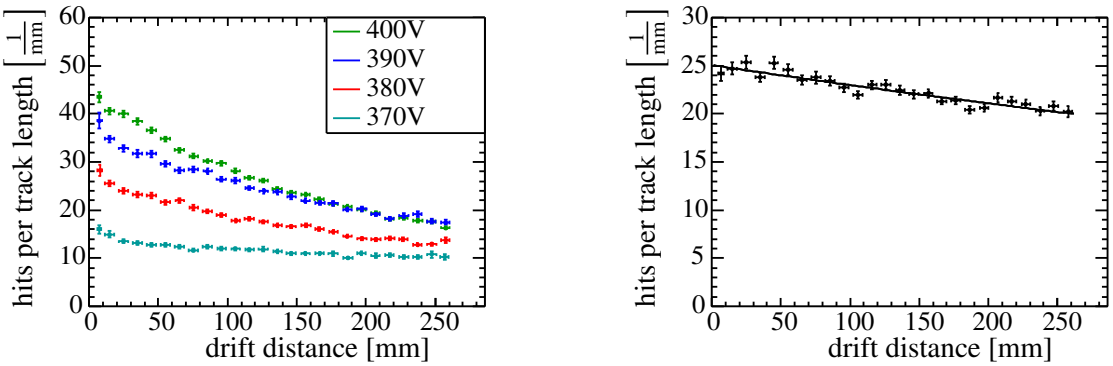

Figure 5.17: The number of track points per unit length for different drift lengths. The argon campaigns are displayed in a) and the helium campaign in b). The declination is explained by electron capture of oxygen impurities inside the drift volume.

implemented at the entrance of the TPC. With this setup, the lowest amount of oxygen was measured. The oxygen amount was determined by comparing the measured slope of the exponential function and simulations of the drifting electrons for different impurities of oxygen in Garfield++. The result is an oxygen level of $\approx 10\,\text{ppm}$. The result is biased by the fact that tracks with less than six electrons are not taken into account. This is visible in the four argon campaigns. One observes in figure 5.17a that the slopes are different for the measurements although the setup was not changed for three of the campaigns. The oxygen level in He:CO_2 is the only one presented as the simulations for the determination has only been done for this gas mixture. Also the electron efficiency is higher and the biasing of the results is diminished. The evidence of a higher electron efficiency follows in the next paragraph.
The number of electrons along the track corresponds to the energy loss of the charged particle inside the chamber. The value depends on the gas mixture and on the energy of the charged particles. Therefore, a simulation of the energy transfer of the charged particle was simulated with the program HEED [39]. HEED is able to simulate the distributions of the number of electrons per track length for many gas mixtures and particle energies. A 4 GeV muon was simulated to travel through the TPC. The distribution of the electron number has the typical Landau shape. To calculate the single electron efficiency, one must compare the mean of the simulation with the detected one. The Landau distribution has a very long tail that enlarges the mean. Figure 5.18 shows the simulation result for the gas mixture of He:CO_2. The cut on the number of electrons per track in the measurements reduces the Landau tail. One has a mean number of electrons per track length of $\sim 80\,\text{cm}^{-1}$ for Ar:CO_2 and $\sim 27\,\text{cm}^{-1}$ for He:CO_2. As the implemented cut on the data does not take into account the track length, the cut off value of the simulation is not exactly the same as in the measurement. The mean varies strongly with the cut off value and only the approximation of the number of electrons is presented.

For very short drift lengths of the electrons, the electron capture can be neglected. So one can compare the simulated results with the measured ones. In the argon campaigns one observes a rise in the maximum number of electrons with the grid voltage. This is an indication that the maximal electron efficiency is still not reached. Furthermore, the maximum number of $\sim 42\,\text{cm}^{-1}$ is only half of the expected $\sim 80\,\text{cm}^{-1}$ from the simulation. A larger grid voltage was not applied due to the fear of destroying the Timepix chip. On the other hand, the maximal number of electrons per track length of the helium campaign nearly reaches the value of the simulation. The gas gain of 1874.1 ± 4.5 in helium seems to

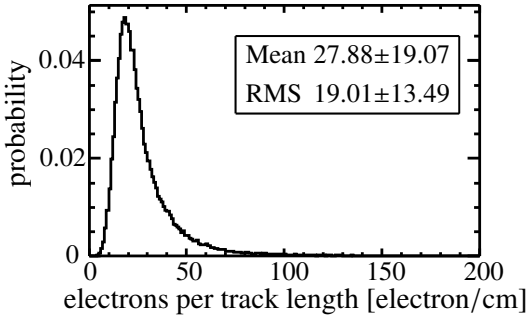

Figure 5.18: Simulated number of electrons per track length for a gas mixture of He:CO_2 and 4 GeV muons.

suffice for a very high single electron efficiency. This is an advantage compared to a pad readout where one can only detect several electrons at once and thus fewer track points as with an InGrid and Timepix readout. The high single electron efficiency results in a high track resolution as many track points can be detected.

5.11 Spatial Resolution

One of the main tasks of the thesis was the measurement of the spatial resolution of track points with an InGrid based readout of a TPC. It is important to distinguish between transverse and longitudinal spatial resolution. This is due to three reasons in the current setup. The diffusion coefficients of the electrons differs for both orientations as explained in chapter 2.3. Hence, the physical limitation of the detector is different, which has to be considered. The second reason is the detection mechanism of the Timepix. The transverse position of hits is detected by the position of the corresponding pixel. The resolution is limited by the size of the pixels or by the size of the amplification structure. On the other hand, the longitudinal dimension is reconstructed with the time measurement of the pixel. As the clock is counted, the frequency of the clock restricts the resolution in longitudinal direction. The last reason to distinguish between the orientations is a possible magnetic field inside the chamber. Typically the magnetic field is applied parallel to the electric field. The magnetic field forces the charged particles onto a helix shaped trajectory. This reduces the diffusion of the drifting electrons and allows a momentum measurement of the traversing charged particles. The curvature is only in the transverse orientation and one can only detect the transverse momentum of the particle. Thus, it is of great importance to have a high transverse resolution as more information lies in this orientation.
To determine the resolution of the detector, one calculates the distribution of the residuals of the hits. The distribution has a Gaussian shape as one expects as a result of the diffusion. Figure 5.27 shows such a distribution. The deviance from a Gaussian function is explained in the chapter 5.11.3. Due to the diffusion of the electrons, the resolution is dependent on the drift length. Therefore, one subdivides the drift region into smaller parts and creates the residual distribution for each part. The width σ_{N} of the distribution does not display the resolution of the detector. As the residual of a hit was calculated with track fits, that included the hit itself, σ_{N} is an underestimation of the spatial resolution.
Hence, one now determines a new track that does not contain the hit in the fit. The distance of the hit from the new track is then stored in a new distribution. This is done for every hit on a track. The width $\sigma_{\mathrm{N-1}}$ of this distribution is an overestimation of the resolution. The best approximation of the detector

resolution is the geometrical mean of both values. So the spatial resolution σ_{geo} is defined as:

$$\sigma_{\text{geo}} = \sqrt{\sigma_{\text{N}}\sigma_{\text{N-1}}} \tag{5.18}$$

The diffusion limits the possible resolution of a TPC. In chapter 2.3 the relation of the resolution and the diffusion coefficient D is defined as:

$$\sigma = D\sqrt{z} \tag{5.19}$$

with z the drift length.
Every setup and detector has an intrinsic resolution σ_0. The intrinsic resolution of the detector modifies the resolution equation of the detector to

$$\sigma = \sqrt{\sigma_0^2 + D^2 z}. \tag{5.20}$$

5.11.1 Transverse Spatial Resolution

The intrinsic spatial resolution of an InGrid and Timepix readout is affected by the pixel size and the hole pitch of the grid. As both have the same size, one can just take the pixel size of $d = 55\,\mu\text{m}$. With the assumption that the detection efficiency is constant over the whole pixel, one can calculate the intrinsic spatial resolution of the detector to:

$$\sigma_0 = \frac{d}{\sqrt{12}} \approx 15.9\ \sqrt{\mu m} \tag{5.21}$$

The transverse spatial resolution was determined for all five measurement campaigns. The figures 5.19 and 5.20a show the spatial resolution dependent on the drift length of the tracks. The used data sample is the large sub-area of the Timepix which still suffers from field distortions. The blue lines in the figures are the theoretical limits, which are just determined by the diffusion constant (see equation (5.19)). The diffusion constant were simulated with Magboltz for each set of running parameters of the measurement campaigns.
The spatial resolution of the detector is relatively close to the theoretical limit for all five parameter configurations. Unfortunately, the difference is larger than simply the intrinsic detector resolution due to the finite size of the pixels. The distortions in the drift field influence the detector performance and enlarge the intrinsic resolution of the detector. A fit of the detector resolution equation (5.20) can be done, but has only a low significance. On the one hand, the fitting parameters σ_0 and D are correlated. On the other hand, small changes in the measured values strongly influence the fitting results and the result does not perfectly fit the measured curvature. The fitting results are presented in table 5.2. Another possibility to gain the intrinsic resolution is the interception point of the measured values and the y-axis. In the limit of a zero drift distance the spatial resolution is only determined by the intrinsic detector resolution. Unfortunately, the trigger delay is too large to approximate the interception point. One will have to use a faster trigger to use this method in the current experimental setup.
Now one can look at the data of the chip that is influenced the least by the field inhomogeneities above the grid. The transverse spatial resolution of the small area is displayed in figures 5.21 and 5.20b. The resolution is very close to the theoretical limit of a TPC. Again the results of the fits is presented in table 5.3. The large deviations of the measurement values in the figure 5.21d are a result of a poor statistic due to the low efficiency and cuts applied. If the intrinsic resolution of the InGrids is close to the fit results, the InGrids reach the required spatial resolution of the ILD project. Nevertheless, the active area

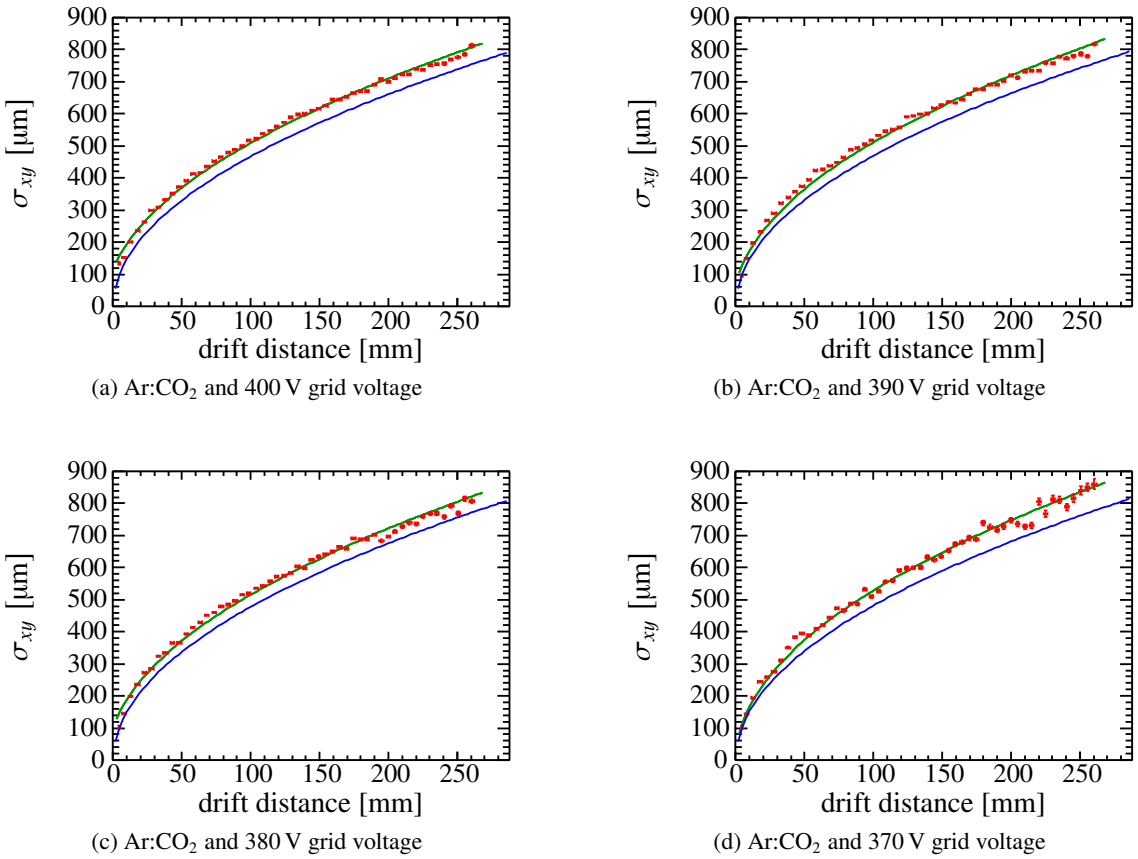

(a) Ar:CO_2 and 400 V grid voltage

(b) Ar:CO_2 and 390 V grid voltage

(c) Ar:CO_2 and 380 V grid voltage

(d) Ar:CO_2 and 370 V grid voltage

Figure 5.19: Transverse spatial resolution of the InGrid detector for the four argon campaigns. The grid voltage is written beneath the figures. The blue lines are the theoretical limits through diffusion and the green lines are the fitted functions.

with low field distortions is too small.

5.11.2 Correction of Field Inhomogeneities

One can try to correct the field distortions in the reconstruction chain to enlarge the chip area with the highest spatial resolution. The idea is that the field distortions just causes all the electrons to be shifted a certain amount in the direction of the electric field lines. If one then calibrates the electrons to their original position, one can reconstruct the correct track parameters of the muons. The chip was divided in 40×40 segments to measure the average shift of the electrons for each segment. The residuals of the hits should contain an information of the shifting direction of the electron. Therefore, the mean and the RMS of the xy-residuals of hits inside each segment was calculated. The mean correlates with the average shift of the hits with respect to the track position. Figure 5.22 shows the results of the mean and RMS of the xy-residuals of each segment. One can see the area on the chip that is not affected by the field distortion in the mean as well as the RMS distribution. But at the bottom side of the chip the curvature of the tracks and the high RMS of the xy-residuals are visible. As the tracks are nearly parallel to the x-axis, the field distortions in the y-direction are the only ones that reduce the resolution of the hits. The electrons of each segment are now shifted in the y-direction as far as the deviation of the mean

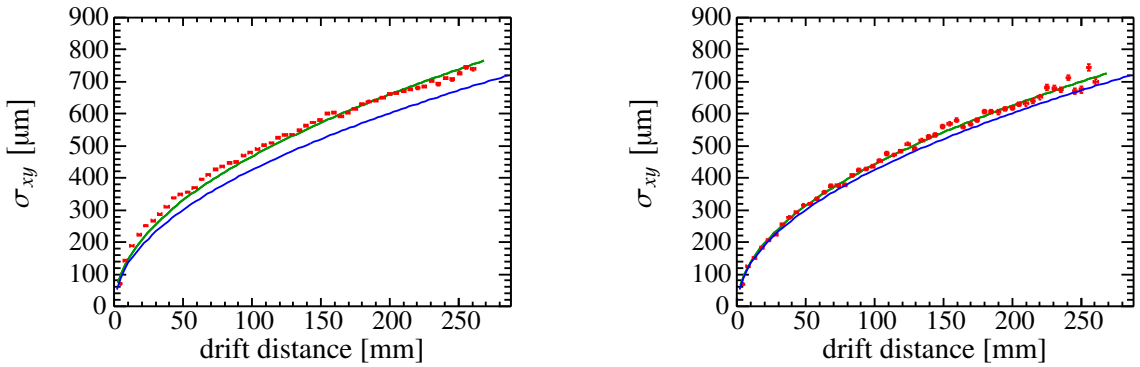

Figure 5.20: Transverse spatial resolution of the InGrid detector for the helium campaign. The blue lines are the theoretical limits through diffusion and the green lines are the fitted functions. a) The complete chip area is used. b) The chip area with the highest resolution is used.

gas and grid voltage	fitted σ_0 $\left[\sqrt{\mu m}\right]$	fitted D_{xy} $\left[\mu m/\sqrt{mm}\right]$	simulated D_{xy} $\left[\mu m/\sqrt{mm}\right]$
He/CO_2 490 V	$3.7 \cdot 10^{-08} \pm 2.6$	147.71 ± 0.15	$134.5 \pm 2.89\,\%$
Ar/CO_2 370 V	13.2 ± 29.5	167.1 ± 0.35	$152.3 \pm 1.68\,\%$
Ar/CO_2 380 V	102.5 ± 5.0	159.80 ± 0.30	$151.1 \pm 1.26\,\%$
Ar/CO_2 390 V	67.8 ± 5.9	160.14 ± 0.24	$148.4 \pm 1.59\,\%$
Ar/CO_2 400 V	118.1 ± 3.6	156.51 ± 0.24	$147.7 \pm 1.41\,\%$

Table 5.2: Fit result of the spatial resolution (equation (5.20)) for the large chip area.

of the *xy*-residuals from zero. Then one must again use the linear regression to calculate the change in the track parameters. After that, one creates the maps of the *xy*-residuals again and receives the results in figure 5.23.
The figures show that the mean of the *xy*-residuals is reduced by a factor of ~ 2. Nevertheless, the RMS of the distribution does not change that much. This results in only a small change in the transverse resolution of the complete chip area. In figure 5.24 the transverse spatial resolution with and without the correction of the hit position is displayed. The deviation is very small, but all points are shifted to lower values.
The correction of the field distortions does not work yet. The assumptions for the field correction seem

gas and grid voltage	fitted σ_0 $\left[\sqrt{\mu m}\right]$	fitted D_{xy} $\left[\mu m/\sqrt{mm}\right]$	simulated D_{xy} $\left[\mu m/\sqrt{mm}\right]$
He/CO_2 490 V	$3.1 \cdot 10^{-08} \pm 57.1$	139.96 ± 0.25	$134.5 \pm 2.89\,\%$
Ar/CO_2 370 V	$1.2 \cdot 10^{-07} \pm 101.1$	153.53 ± 0.54	$152.3 \pm 1.68\,\%$
Ar/CO_2 380 V	$2.2 \cdot 10^{-07} \pm 315.1$	151.49 ± 0.31	$151.1 \pm 1.26\,\%$
Ar/CO_2 390 V	$3.4 \cdot 10^{-07} \pm 552.4$	151.38 ± 0.26	$148.4 \pm 1.59\,\%$
Ar/CO_2 400 V	$5.5 \cdot 10^{-06} \pm 49.8$	150.80 ± 0.30	$147.7 \pm 1.41\,\%$

Table 5.3: Fit result of the spatial resolution (equation (5.20)) for the small chip area.

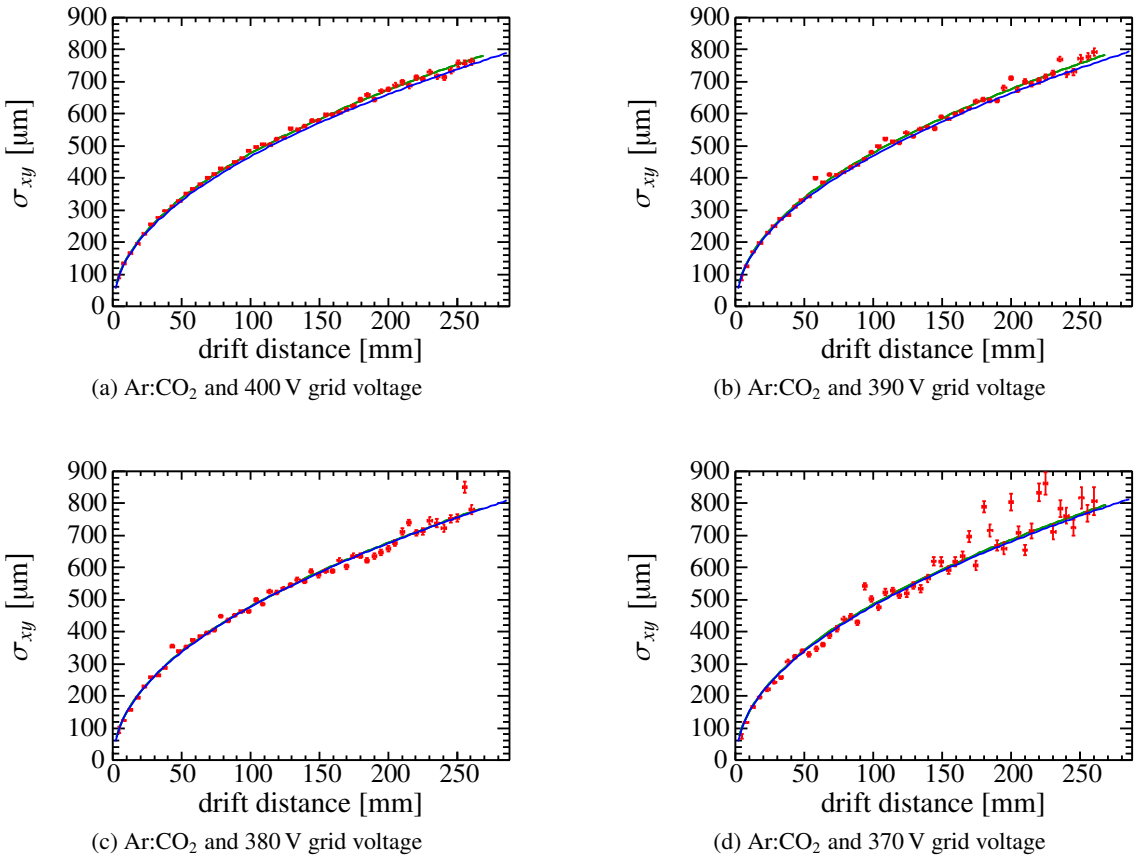

(a) Ar:CO_2 and 400 V grid voltage

(b) Ar:CO_2 and 390 V grid voltage

(c) Ar:CO_2 and 380 V grid voltage

(d) Ar:CO_2 and 370 V grid voltage

Figure 5.21: Transverse spatial resolution in the area of least field distortions for the four argon campaigns. The grid voltage is written beneath the figures. The blue lines are the theoretical limits through diffusion and the green lines are the fitted functions.

to be too simplified and also the binning of the map might be too large.

5.11.3 Longitudinal Spatial Resolution

The intrinsic resolution of the Timepix chip in longitudinal direction is influenced by the clock frequency. If the time of the electron would be reconstructed perfectly, the intrinsic detector resolution of the Timepix in longitudinal direction is given by:

$$\sigma_0 = \frac{v}{\nu\sqrt{12}} \approx 50\,\mu\text{m} \tag{5.22}$$

with v the drift velocity of the electrons and the clock frequency ν. The figures 5.25 and 5.26 show the measured longitudinal spatial resolution dependent on the drift length. In contrast to the transverse resolution, the longitudinal resolution deviates highly from the theoretical limit. Even in the area, which is the least influenced by the field distortions, the longitudinal resolution looks the same (see appendix A figures A.1 and A.2).
The reason of the deviation from the theoretical detector resolution is the timewalk effect of the discriminators. One can see the influence of the timewalk in figure 5.27a. The figure sows the distribution

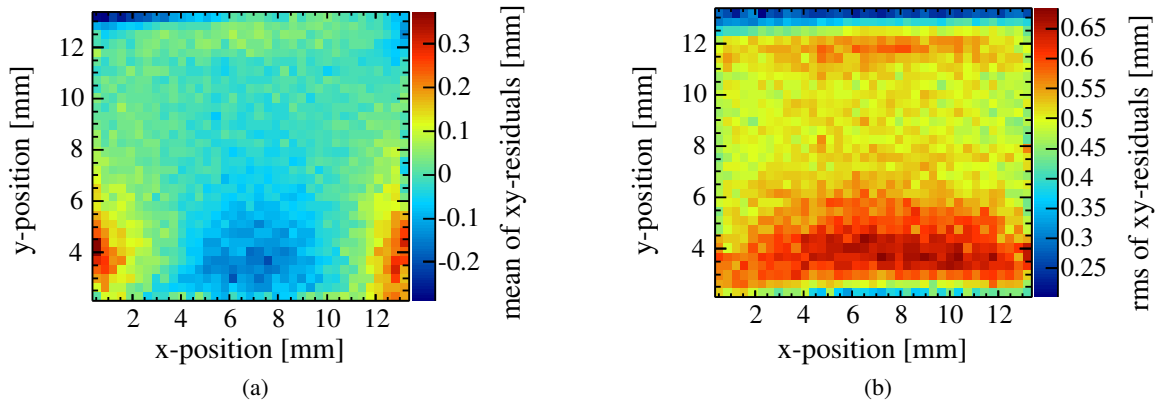

(a) (b)

Figure 5.22: a) The map shows the mean of the *xy*-residuals of the corresponding segment of the chip. b) Equivalent to a) with the RMS of the *xy*-residuals.

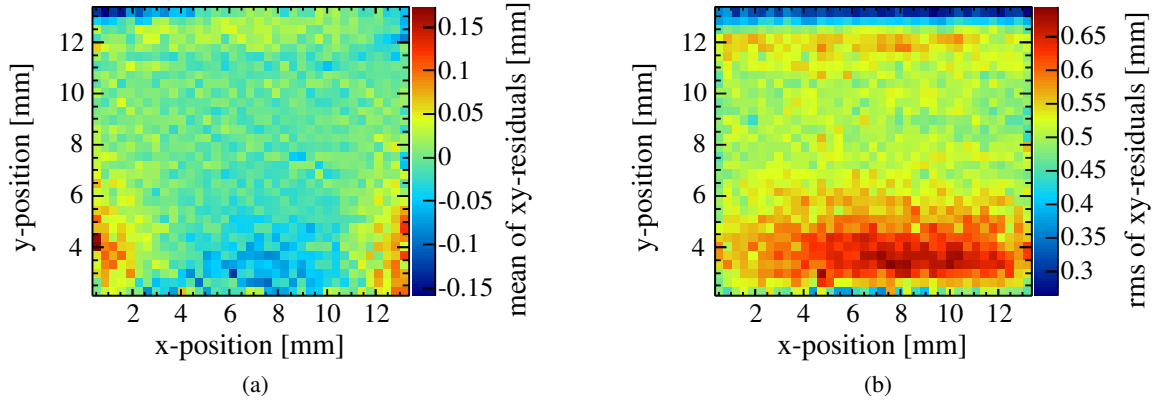

(a) (b)

Figure 5.23: a) The map shows the mean of the *xy*-residuals of the corresponding segment of the chip after the attempt to correct the field distortions. b) Equivalent to a) with the RMS of the *xy*-residuals.

of the z-residuals for all drift lengths. On the one hand, one measures a maximum of the distribution inconsistent with zero. On the other hand, the distribution has a larger tail for higher z-residuals. If we observe timewalk effects in the electronics, the drifting electrons are reconstructed with a larger drift distance in the chamber as they should. This leads to a wrong reconstruction of the tracks. Especially, the hits with a very low charge are shifted towards larger z-positions. These large shifts of electrons are the reason for both observations in the distribution of the z-residuals. One would be able to calibrate the timewalk effect (see figure 5.2b) if one could also measure the charge of the induced signal. Due to the activation of a single hit by one electron avalanche, this is not possible with the Timepix chip.
To estimate the effect of the timewalk on the longitudinal spatial resolution, a Gaussian function was fitted to the left side of the distribution of the z-residuals. The left side of the distribution should be less effected by the timewalk as the timewalk is responsible for large z-residuals. An example of this fit is shown for a small part of the drift length in the figure 5.28.
If one now uses the standard deviation of the Gaussian function instead of the RMS of the z-residuals, one reaches a longitudinal spatial resolution as seen in figure 5.29b. The resolution gets closer to the

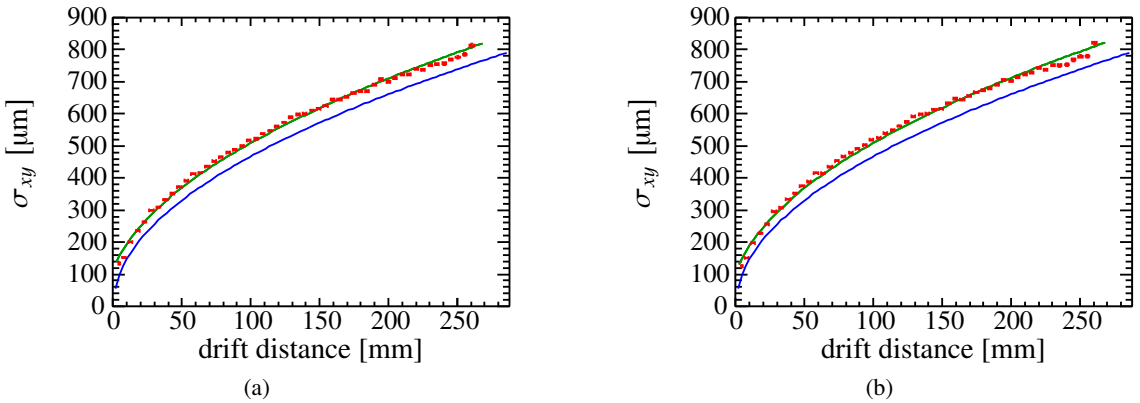

Figure 5.24: Comparison between the measured data with b) and without a) the correction of the field distortions.

theoretical limit but it still deviates more than one would expect without the timewalk effect. The successor chip of the Timepix should be able to reach a higher longitudinal resolution as it can measure charge and time information at the same time. So, one can calibrate the timewalk and the longitudinal resolution should only depend on the readout frequency and the drift velocity of the electrons.

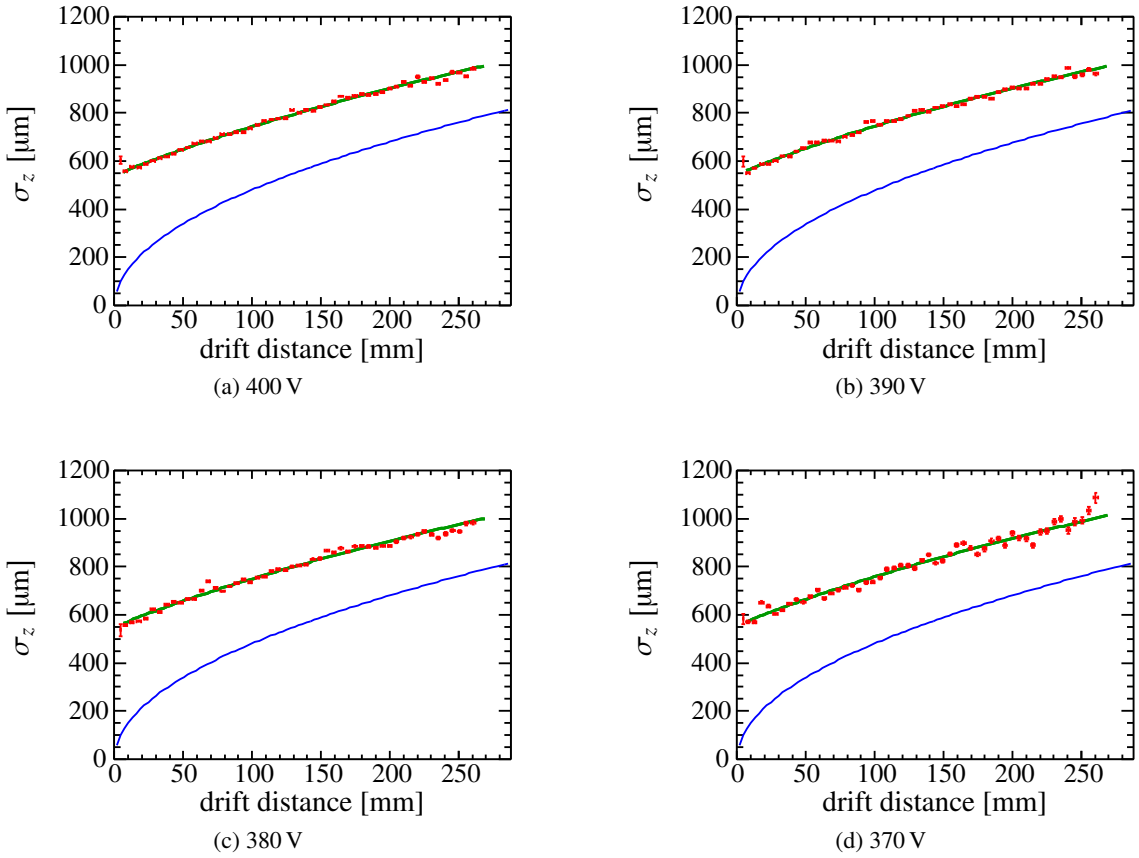

(a) 400 V (b) 390 V

(c) 380 V (d) 370 V

Figure 5.25: Longitudinal spatial resolution of the InGrid detector for the four argon campaigns. The grid voltage is written beneath the figures. The blue lines are the theoretical limits through diffusion and the green lines are the fitted functions.

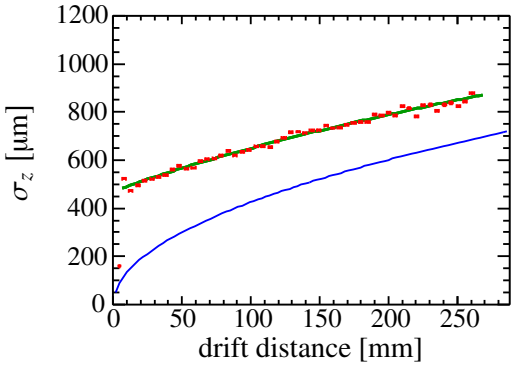

Figure 5.26: Longitudinal spatial resolution of the InGrid detector for the helium campaign. The blue line is the theoretical limit because of diffusion and the green line is the fitted function.

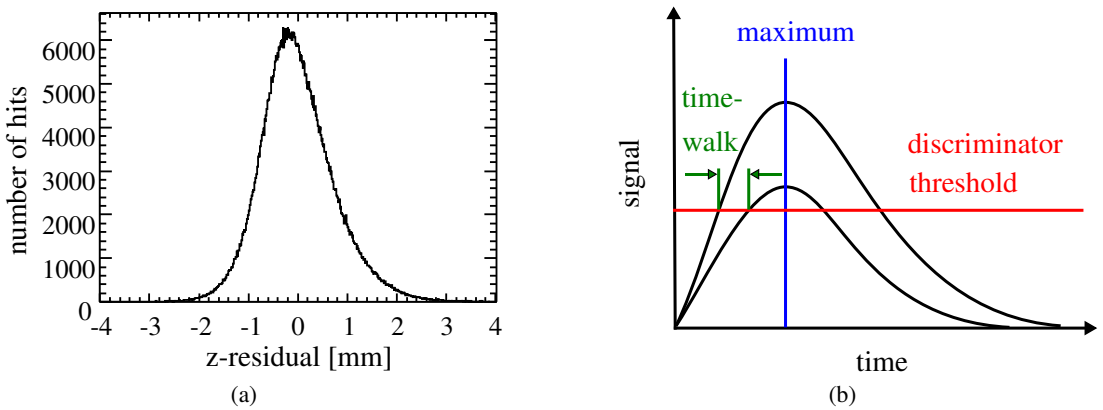

(a) (b)

Figure 5.27: a) Distribution of the z-residuals of each hit. b) A sketch of the timewalk effect of a discriminator.

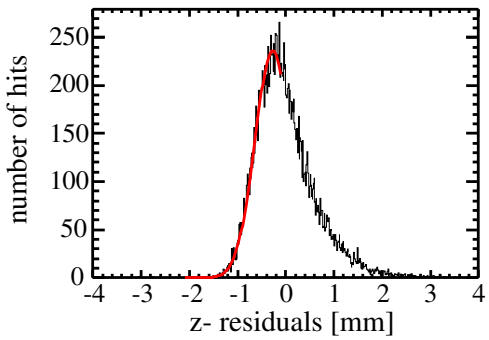

Figure 5.28: z-residuals for a small part of the drift length and a Gaussian function fitted to the left side of the distribution.

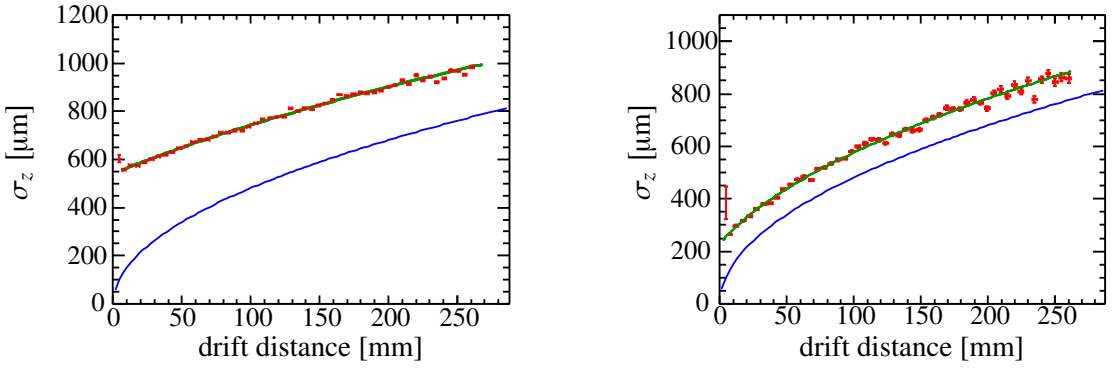

(a) (b)

Figure 5.29: Comparison between the approximated longitudinal spatial resolution from the RMS of the z-residuals a) and the standard deviation of the fitted Gaussian function b). The blue line is again the theoretical limit and the green line a fit of equation (5.20).

Chapter 6

Conclusion

The Timepix chip with an InGrid structure was successfully mounted in the Bonner time projection chamber. The tracks from cosmic rays were detected for two different gas mixtures and varying grid voltages. A thorough analysis of the gas amplification has been done to study the signal of primary electrons after the gas amplification. It was found that for the gas gains used the induced signal of one electron avalanche can only activate a single pixel of the chip. In a gas mixture of He:CO_2 (70:30) and a grid voltage of 490 V a very high single electron efficiency was achieved with a gas gain of around 1800. The efficiency in the Ar:CO_2 (70:30) was lower than 60 % due to the low gas gain.
The transverse spatial resolution of a limited area proved to be very close to the theoretical diffusion. The intrinsic detector resolution is limited by the finite pixel size. In the vicinity of the chip border and, in particular, close to the wire bonds, the measurement of the transverse spatial resolution showed the influence of field distortions. These are caused by the gap between the grid and anode plate. An area on the chip was identified that was the least influenced by the field inhomogeneities.
The spatial resolution in the longitudinal direction was also analyzed. The timewalk effect of the discriminators causes the hits to be reconstructed with larger drift lengths. As each drifting electron causes the activation of a single pixel, the complete chip has to run in a single measurement mode. Therefore, the timewalk effect cannot be corrected and the longitudinal spatial resolution deviates considerably from the diffusion limit.
The measurements of an InGrid structure on top of a Timepix chip show promising results for the ILD. Nevertheless, the drawbacks of the current setup, namely the timewalk and the field distortion, have to be reduced or corrected to achieve the desired spatial resolution. Therefore, a new carrier PCB was developed but could not be implemented until the end of the thesis. Furthermore, the successor of the Timepix, called Timepix3, will be produced in 2012 and will solve the problems created by the timwalk. The new chip will be able to measure the charge and the time information in each pixel at the same time. Hence, one can just correct the timewalk with a calibration of the chip. The Timepix3 will also allow the user to reduce the gap size between the anode plate and the grid structure. Further measurements still have to be performed. A readout with multiple InGrids and a magnetic field is desired to determine the momentum resolution and the energy loss resolution of a TPC with an InGrid based readout. In addition, measurements of the track resolution must be performed at a test beam.

Appendix A

Backup Figures

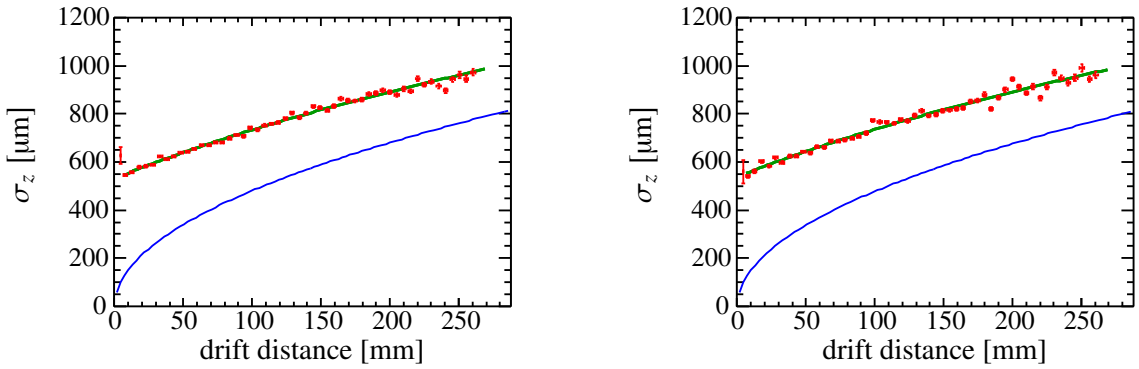

(a) 400 V

(b) 390 V

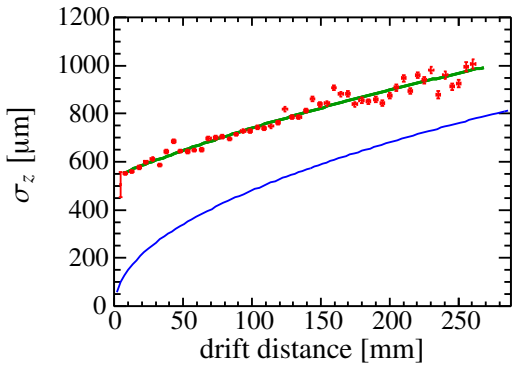

(c) 380 V

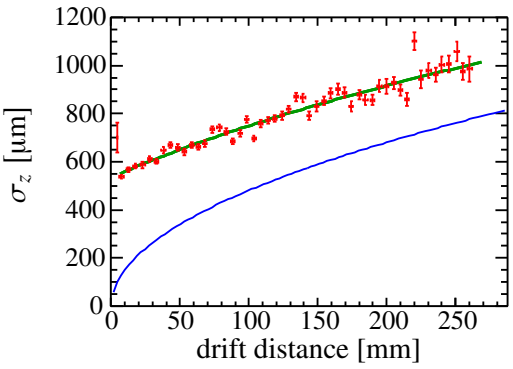

(d) 370 V

Figure A.1: Longitudinal spatial resolution in the area of least field distortions for the four Argon campaigns. The grid voltage is written beneath the figures. The blue lines are the theoretical limits through diffusion and the green lines are the fitted functions.

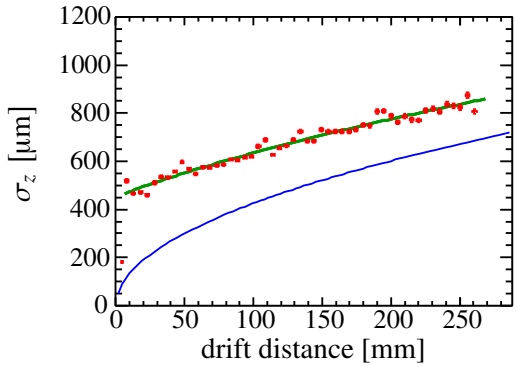

Figure A.2: Longitudinal spatial resolution in the area of least field distortions for the helium measurement. The blue line is the theoretical limits through diffusion and the green line is the fitted function.

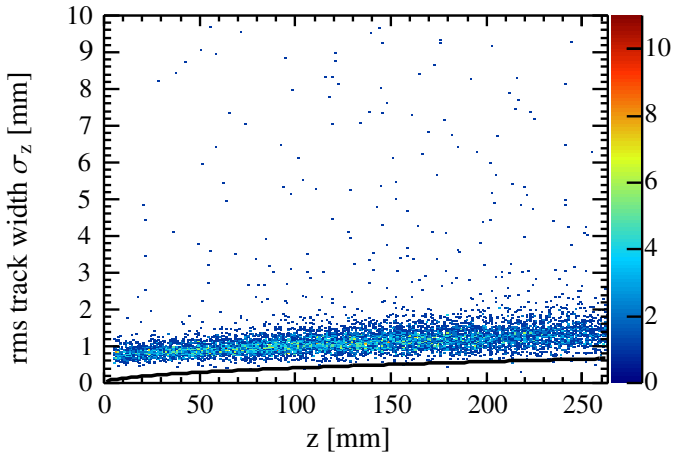

Figure A.3: Longitudinal spatial resolution of each track dependent on the drift length. The outliers are caused by noise events and wrong track reconstructions.

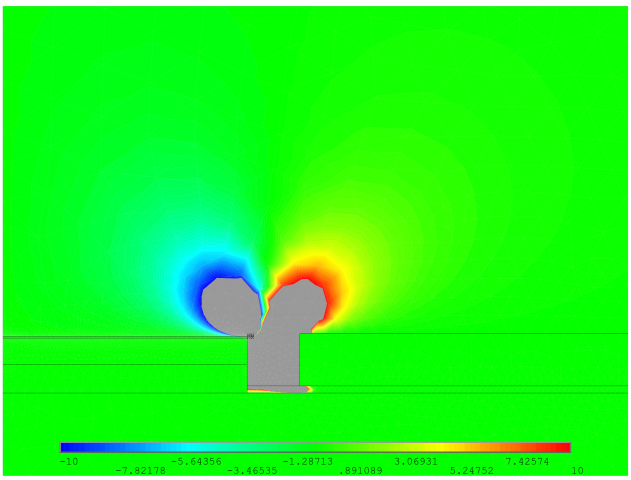

Figure A.4: Simulation of the electric field at the gap of anode plate and grid created with ANSYS. The electric field parallel to the chip plane is displayed. The design value in green is $0\,\mathrm{V\,cm^{-1}}$ and the color range is $\pm 10\,\mathrm{V\,cm^{-1}}$. The chip is in the left part of the picture and the gap size is 1 mm [40].

Bibliography

[1] Gerald Aarons et al. 'International Linear Collider Reference Design Report Volume 2: Physics at the ILC'. In: (2007). eprint: 0709.1893.

[2] (Ed.) Behnke Ties et al. 'ILC Reference Design Report Volume 4 - Detectors'. In: (2007). eprint: 0712.2356.

[3] The ILD Concept Group. 'The International Large Detector: Letter of Intent'. In: (2010). eprint: 1006.3396.

[4] 2011th Sept. 09. URL: http://www.ilcild.org/.

[5] R. Blum and L. Rolandi. *Particle Detection with Drift Chambers*. second. Springer, 2008.

[6] C. Grupen. *Particle detectors*. first. Cambridge University Press, 1996.

[7] W.-M. Yao et al. 'Review of Particle Physics'. In: *J. Phys. G* 33 (2006). URL: http://pdg.lbl.gov.

[8] J.E. Moyal. 'Theory of Ionization Fluctuations'. In: *Phil. Mag.* 46 (1970).

[9] K. Affholderbach et al. 'Performance of the new Small Angle Monitor for BAckground (SAMBA) in the ALEPH experiment at CERN'. In: *Nucl.Instrum.Meth.* A410 (1998), pp. 166–175.

[10] M. Huk, P. Igo-Kemenes and A. Wagner. 'Electron attachment to oxygen, water and methanol, in various drift chamber gas mixtures'. In: *Nucl.Instrum.Meth.* A267 (1988), pp. 107–119.

[11] Felix Bloch and Norris Bradbury. 'On the Mechanism of Unimolecular Electron Capture'. In: *Phys.Rev.* 48 (1935), pp. 689–695.

[12] S.C. Brown. *Basic data of plasma physics*. Technology Press books in science and engineering. Technology Press of the Massachusetts Institute of Technology, 1959.

[13] John J. Lowke and James H. Parker. 'Theory of Electron Diffusion Parallel to Electric Fields. 2. Application to Real Gases'. In: *Phys.Rev.* 181 (1969), pp. 302–311.

[14] F. Sauli. 'Principles of Operation of Multiwire Proportional and Drift Chambers'. In: (). CERN-77-09.

[15] W.J. Price. *Nuclear radiation detection*. McGraw-Hill series in nuclear engineering. McGraw-Hill, 1964.

[16] Werner Legler. 'Zur Statistik der Elektronenlawinen'. In: *Z. Phys.* 140 (1955), pp. 221–240.

[17] G.D. Alkhazov. 'Statistics of electron avalanches and ultimate resolution of proportional counters'. In: *Nucl.Instrum.Meth.* 89 (1955), pp. 155–165.

[18] Simon Ramo. 'Currents induced by electron motion'. In: *Proc.Ire.* 27 (1939), pp. 584–585.

[19] D.R. Nygren. 'The Time Projection Chamber: A New 4 pi Detector for Charged Particles'. In: (1974), p. 58.

[20] M. Schultens. ‘Teststrahlmessungen mit hochgranularer Auslese einer Zeitprojektionskammer bei verschiedenen Pixelgrößen’. PhD thesis. University of Bonn, 2010.

[21] M. Killenberg. ‘Resolution Studies of a GEM- Based TPC’. PhD thesis. RWTH Aachen, 2006.

[22] Nan Phinney, Nobukasu Toge and Nicholas Walker. ‘LC Reference Design Report Volume 3 - Accelerator’. In: (2007). eprint: 0712.2361.

[23] F. Sauli. ‘GEM: A new concept for electron amplification in gas detectors’. In: *Nucl.Instrum.Meth.* A386 (1997), pp. 531–534.

[24] S. Kappler. ‘Higgs Search Studies in the Channel ttH with the CMS Detector at the LHC and Development of a GEM-based Readout for Future Collider Experiments’. PhD thesis. University of Karlsruhe, 2004.

[25] J. Kaminski. ‘Developing studies for a time projection chamber at the International Linear Collider (ILC)’. PhD thesis. University of Karlsruhe, 2005.

[26] S. Andriamonje et al. ‘Development and performance of Microbulk Micromegas detectors’. In: *JINST* 5 (2010), P02001.

[27] (ed.) Behnke T. et al. ‘TESLA: The superconducting electron positron linearcollider with an integrated X-ray laser laboratory. Technical design report. Pt. 4: A detector for TESLA’. In: (2001).

[28] Y. Giomataris et al. ‘MICROMEGAS: A High granularity position sensitive gaseous detector for high particle flux environments’. In: *Nucl.Instrum.Meth.* A376 (1996), pp. 29–35.

[29] Y. Giomataris. ‘Development and prospects of the new gaseous detector ’Micromegas’’. In: *Nucl.Instrum.Meth.* A419 (1998), pp. 239–250.

[30] X. Llopart et al. ‘Timepix, a 65k programmable pixel readout chip for arrival time, energy and/or photon counting measurements’. In: *Nucl. Instr. and Meth. A* 581.1-2 (2007), pp. 485 –494.

[31] C. Brezina, K. Desch and J. Kaminski. ‘Operation of a GEM TPC with Pixel Readout’. In: *proceedings of IEEE NSS 2011 in Valencia* (2011).

[32] J. Kaminski et al. ‘A Time Projection Chamber with triple GEM and pixel readout’. In: *Journal of Instrumentation* 4.11 (2009), P11015.

[33] Maximilien Alexandre Chefdeville. ‘Development of micromegas-like gaseous detectors using a pixel readout chip as collecting anode’. PhD thesis. University of Amsterdam, 2009.

[34] S. Blatt. ‘Konstruktion und Inbetriebnahme eines Feldkäfigs für eine TPC’. PhD thesis. RWTH Aachen, 2004.

[35] Thomas Krämer. ‘Track parameters in LCIO’. In: (2006).

[36] S. Biagi. *Magboltz*. URL: http://consult.cern.ch/writeup/magboltz/.

[37] D. Rapp and P. Englander-Golden. ‘Total Cross Sections for Ionization and Attachment in Gases by Electron Impact. I. Positive Ionization’. In: *jcp* 43 (Sept. 1965), pp. 1464–1479.

[38] H. Schindler and R. Veenhof. *Garfield++*. URL: http://garfieldpp.web.cern.ch/garfieldpp/.

[39] I.B. Smirnov. ‘Modeling of ionization produced by fast charged particles in gases’. In: *Nucl.Instrum.Meth.* A554 (2005), pp. 474–493.

[40] C. Krieger. ‘Construction and First Measurements of a GridPix based X-ray Detector’. PhD thesis. University of Bonn, 2011.

List of Figures

1.1 Left: Illustration of the whole ILD. Right: Zoom inside the TPC of the ILD [4] 2

2.1 Illustration of the energy deposition of a muon. The Bethe-Bloch equation is only valid in the Bethe range and becomes invalid under very high energies due to radiative losses and under very low energies due to the internal structure of atoms [7]. 6
2.2 Energy deposition per unit length for single events in the PEP-4-Experiment. The data is well described by the Bethe-Bloch function for several particle types [7]. 7
2.3 Energy loss of 3 GeV electrons in a small drift chamber of the SAMBA experiment [9]. A Landau-distribution characterizes the measured data. 8
2.4 Cross sections of electron-Argon scattering with respect to the electron energy. The minimum relates from quantum mechanical description and was first discovered by Ramsauer [12]. 11
2.5 Working regions of a cylindrical gaseous detector [15] 14
2.6 Schematic of a Time Projection Chamber as planned for the International Large Detector [20] 17
2.7 a) Schematic of the amplification and readout plane of a standard TPC. b) Field lines of the corresponding setup [20, 21]. 18
2.8 Field lines of the two modes of operation of a TPC with gating grid. a) Gating grid opened and c) gating grid closed [21]. 19
2.9 a) Electron-microscopic pictures of a GEM [24]. b) Schematic drawing of the field lines and the gas amplification process inside one hole of a GEM [25]. 20
2.10 Schematic view of a Miromegas detector [27]. 21

3.1 a) Picture of the Timepix chip on the carrier PCB. b) Analog part of the circuitry of the Timepix [30]. 24
3.2 Timing scheme of the Timepix chip [31]. 24
3.3 Scheme of the production process of InGrids. Light gray: Silicon chip, dark gray: metal bump bond pads and grid, green: passivation layer, blue: SiProt, light red: unexposed SU-8, dark red: exposed SU-8 25
3.4 An Electron-microscopic picture of an InGrid structure a) and the pillar structure without grid b) [33]. 26
3.5 a) Picture of the field cage developed at the RWTH Aachen. b) Picture of the TPC as it is used in this work. In the left end cap the readout structure is implemented. 27
3.6 Setup of the experiment 28
3.7 Interior view of the readout end cap a) without and b) with anode plate. 29

4.1 Sketch of the track parametrization in LCIO [35]. 32

5.1 Four typical examples for tracks inside the experimental setup. The chip plane is represented by the *xy*-plane in the reconstruction while the abscissa reflects the way between the scintillators. The binning is reduced by a factor of four in both dimensions to enhance the visibility of the detected hits. 34
5.2 a) Histogram of the time difference of two neighboring pixel. b) Calibration of the timewalk effect. 35
5.3 a) Charge spectrum of single pixel (red), pixel with an activated neighbor at a side (blue) and at an edge (green). b) Difference of the charge measured of neighboring pixels. . . 36
5.4 a) Histogram of all ADC values from activated pixels. b) Zoom into the rise of the distribution and sigmoid function fit to get the drift velocity of electrons 37
5.5 Charge calibration curves for the Timepix chip determined by injecting test pulses into each pixel. a) Calibration curve with the pulse height as the abscissa. The fit function is described in the equation 5.17. b) Relation between measured ToT values and induced electrons. 41
5.6 a) Charge spectra of the argon campaigns for all hits on the chip. b) Gas gain of the InGrid for the four different grid voltages in Ar:CO_2. For a gaseous detector in the proportionality range, one would expect an exponential rise which can be seen in the data (exponential fit function). 42
5.7 Charge spectrum of the helium campaign for all hits on the chip. 42
5.8 Histograms of several parameters of the reconstructed tracks without applied cuts on the data. The red lines symbolize the cut values which are used for further studies. a) Histogram of the number of tracks per event. b) Histogram of the measured track length. c) φ-distribution of the tracks. d) λ-distribution of the measured tracks (for the definition of φ and λ see figure 4.1). 43
5.9 Two projections of two incorrectly reconstructed tracks. A single track reconstructed as two independent tracks in *xy*-plane a) and *zx*-plane b). Two tracks lying above each other in the *xy*-plane c) and *zx*-plane d). The color coding is used to identify the electrons corresponding to a single track. 44
5.10 Occupancy plot of a measurement campaign without using cuts on the data. The lines demonstrate the area with the highest electron efficiency on the chip. 45
5.11 Example events of noise hits with reconstructed tracks. The noise hits greatly influence the track reconstruction and worsen spatial resolution. The color coding is used to identify the electrons corresponding to a single track. 46
5.12 a) The distribution of the difference between the median of the *z*-positions of the track hits and each hit's *z*-position. b) The distribution of the RMS of the track hit's *z*-positions. The red lines illustrate the chosen cuts to clean the data from noise hits. . . . 47
5.13 The plots show histograms of the *xy*-residual of hits with respect to the hit's *x*-position a) and *y*-position b). 48
5.14 Mean and RMS for the *xy*-residuals of hits for different *x*-positions on the chip. 49
5.15 a) The histogram of the curvature of the track plotted against the each hit's *y*-position. b) The figure shows the occupancy of the chip and a black frame that marks the area which is influenced the least by the field distortions. 50
5.16 Mean and RMS for the *xy*-residuals of hits for different *x*-positions on the chip. The data consists of tracks inside the chip area which is influenced the least by the field distortions. 50
5.17 The number of track points per unit length for different drift lengths. The argon campaigns are displayed in a) and the helium campaign in b). The declination is explained by electron capture of oxygen impurities inside the drift volume. 51

5.18 Simulated number of electrons per track length for a gas mixture of He:CO_2 and 4 GeV muons. . . . 52
5.19 Transverse spatial resolution of the InGrid detector for the four argon campaigns. The grid voltage is written beneath the figures. The blue lines are the theoretical limits through diffusion and the green lines are the fitted functions. . . . 54
5.20 Transverse spatial resolution of the InGrid detector for the helium campaign. The blue lines are the theoretical limits through diffusion and the green lines are the fitted functions. a) The complete chip area is used. b) The chip area with the highest resolution is used. . . . 55
5.21 Transverse spatial resolution in the area of least field distortions for the four argon campaigns. The grid voltage is written beneath the figures. The blue lines are the theoretical limits through diffusion and the green lines are the fitted functions. . . . 56
5.22 a) The map shows the mean of the *xy*-residuals of the corresponding segment of the chip. b) Equivalent to a) with the RMS of the *xy*-residuals. . . . 57
5.23 a) The map shows the mean of the *xy*-residuals of the corresponding segment of the chip after the attempt to correct the field distortions. b) Equivalent to a) with the RMS of the *xy*-residuals. . . . 57
5.24 Comparison between the measured data with b) and without a) the correction of the field distortions. . . . 58
5.25 Longitudinal spatial resolution of the InGrid detector for the four argon campaigns. The grid voltage is written beneath the figures. The blue lines are the theoretical limits through diffusion and the green lines are the fitted functions. . . . 59
5.26 Longitudinal spatial resolution of the InGrid detector for the helium campaign. The blue line is the theoretical limit because of diffusion and the green line is the fitted function. 59
5.27 a) Distribution of the *z*-residuals of each hit. b) A sketch of the timewalk effect of a discriminator. . . . 60
5.28 *z*-residuals for a small part of the drift length and a Gaussian function fitted to the left side of the distribution. . . . 60
5.29 Comparison between the approximated longitudinal spatial resolution from the RMS of the *z*-residuals a) and the standard deviation of the fitted Gaussian function b). The blue line is again the theoretical limit and the green line a fit of equation (5.20). . . . 60

A.1 Longitudinal spatial resolution in the area of least field distortions for the four Argon campaigns. The grid voltage is written beneath the figures. The blue lines are the theoretical limits through diffusion and the green lines are the fitted functions. . . . 63
A.2 Longitudinal spatial resolution in the area of least field distortions for the helium measurement. The blue line is the theoretical limits through diffusion and the green line is the fitted function. . . . 64
A.3 Longitudinal spatial resolution of each track dependent on the drift length. The outliers are caused by noise events and wrong track reconstructions. . . . 64
A.4 Simulation of the electric field at the gap of anode plate and grid created with ANSYS. The electric field parallel to the chip plane is displayed. The design value in green is $0\,\mathrm{V\,cm^{-1}}$ and the color range is $\pm 10\,\mathrm{V\,cm^{-1}}$. The chip is in the left part of the picture and the gap size is 1 mm [40]. . . . 65

List of Tables

3.1 Dimension values of the InGrid used in this work. The errors are taken from [33]. . . . 26
3.2 Working parameters of the TPC during the measurements. 29

5.1 Measured and simulated drift velocities for all five measurement campaigns. 38
5.2 Fit result of the spatial resolution (equation (5.20)) for the large chip area. 55
5.3 Fit result of the spatial resolution (equation (5.20)) for the small chip area. 55

I hereby certify that the work presented here was accomplished by myself and without the use of illegitimate means or support, and that no sources and tools were used other than those cited.

Bonn, _____ _____

Date Felix Müller